SCALING VIOLATIONS IN QUASIELASTIC ELECTRON SCATTERING

Thesis by

Malcolm Nicholas Butler

In Partial Fulfillment of the Requirements

for the Degree of

Doctor of Philosophy

California Institute of Technology

Pasadena, California

1988

(Submitted June 17, 1987)

Acknowledgements

First I would like to thank Steve Koonin for teaching me how to be a physicist. He let me have enough free rope so that I learned how to do research, but was always there to answer questions when I got really stuck or just paranoid. Also, I'd like to thank him for being patient with me in all the mistakes and screw-ups along the way.

I wouldn't have made it through this place without good friends. I'd like to thank (in no particular order) Wade Regehr, Karl Friehs, Herma Riegler, Matt Johnson, Duncan Morris, Greg Smedley, Michelle Vine, Robert Malaney, Martin Savage and Liz Wood for being there when I wanted to have fun, and when I needed to talk. Also thanks to my friends and office mates Ming Chu, Anne Allder, Dawn Meredith and Dave Wasson (also Volker Pönisch) for making life at the desk bearable, and often fun.

On the more mundane side, thanks to all the Kellogg members of the NE3 collaboration for useful (and frank) discussions on the topic of y-scaling. Also thanks to NSERC Canada for a 1967 Science and Engineering Research Fellowship that covered my four years here.

That I even got here at all is largely due to my parents, Cyril and Elizabeth Butler. They always encouraged me but never pushed, and the best I could do was always enough. This thesis is dedicated to them.

Abstract

We study the phenomenon of y-scaling in inclusive quasielastic electron scattering. Emphasis is placed on the approach to scaling at finite four-momentum transfers, and the effects of final state interactions. Brueckner-Goldstone perturbation theory for nuclear matter is used to perform a detailed, microscopic calculation of the dynamic structure function of nuclear matter. This is compared to the naive prediction of the Impulse approximation, and we find that the approach to scaling is quite different. The Brueckner-Goldstone approach reproduces the trends seen experimentally (Impulse approximation does not); however, there is still not good quantitative agreement with the data. We take this to be a possible sign of problems in the conventional nucleon-nucleon interactions studied.

Contents

List of Figures

List of Tables

Chapter 1

Introduction

In trying to understand the internucleon force, physicists still remain unsure of one critical point, the short-range behavior. Without this information, we cannot determine the relationship between the conventional nuclear physics picture of point nucleons interacting via meson exchange, and the QCD picture of nucleons as "bags" of quarks that exchange quark pairs and gluons at short range. What we know from N-N scattering is that the interaction becomes repulsive at short range. This is taken from the fact that the phase shifts change sign at high energy [1] (high energy is only about 300 MeV; at higher energies inelastic processes become dominant). However, we don't know exactly what the source of this repulsion is. Using the conventional picture, we have vector-meson exchange, which is repulsive at short distances[2], but the range ($\approx$0.25 fm) is significantly smaller than the size of the nucleons themselves ($\approx$0.8 fm). In fact, most meson exchange modes (except for one-pion-exchange) are all of shorter range than the nucleon size (Fig. 1.1). This makes one feel somewhat uncomfortable about using meson exchange at these scales, and in fact, obliged to start considering the interactions of the quarks inside the nucleons. This approach has led to speculation that we might see the formation of hybrid states such as six-quark bags. N-N scattering will almost certainly *not* be able to tell us this– inelastic effects such as pion production dominate at the higher energies required to study the core in detail. Instead, we look to the bound systems of

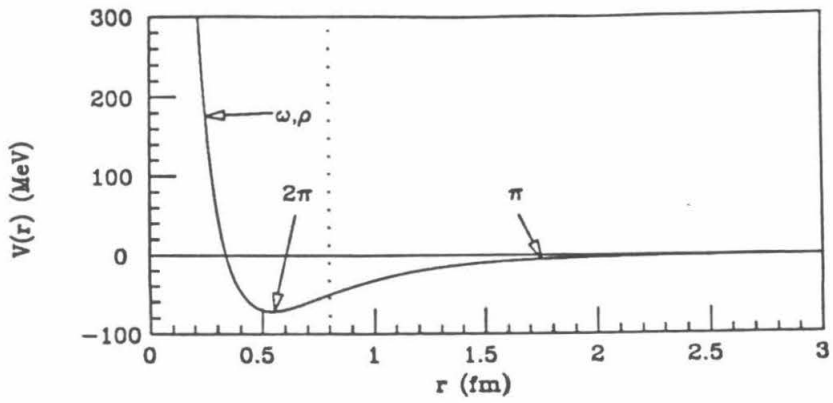

Figure 1.1 $N - N$ potential based on a meson exchange picture. Scales and ranges are based on parameters given by deTourreil *et al.* [3]. Dotted line represents the estimated size of a nucleon.

nucleons, the simplest being the deuteron. If we can study the wavefunctions of such systems in detail, we can see what influences their short distance (or equivalently high-momentum) behavior. It is possible, though, that many different models can produce the same effects in the wavefunction. What we also need is information on the short-range correlations present in larger systems ($A \geq 3$). With this we might start to discern exactly what is happening to the nucleons when they come very close to one another in the nuclear medium.

There are two properties of a nucleus which (in theory) are measurable and can tell us about the wavefunction at short distance scales (or equivalently at high momenta). The spatial distribution $\rho(r)$ (usually measured for practical purposes via the charge density) can be extracted from elastic scattering by taking the Fourier transform of the charge form factor $F(q)$, defined as

$$\begin{aligned} F(q) &= \int d\boldsymbol{r}\; e^{-i\boldsymbol{q}\cdot\boldsymbol{r}}\rho(r) \\ &= \int d\boldsymbol{r}\; e^{-i\boldsymbol{q}\cdot\boldsymbol{r}} \int d\boldsymbol{r}_2 d\boldsymbol{r}_3 ... d\boldsymbol{r}_A |\Psi(\boldsymbol{r}, \boldsymbol{r}_2, \boldsymbol{r}_3, ..., \boldsymbol{r}_A)|^2 \end{aligned} \tag{1.1}$$

(there are also center-off-mass and finite-size effects which must be taken into account in this equation). We can see from the argument of the exponential that large q is going to give us information about *fluctuations* at small r, but there is

nothing in the form factor that will tell us much about correlations. The ideal measurement would be of the off-diagonal part of the one-body density matrix $\rho(\boldsymbol{r}, \boldsymbol{r}')$, defined as

$$\rho(\boldsymbol{r}, \boldsymbol{r}') = \int d\boldsymbol{r}_2 d\boldsymbol{r}_3 ... d\boldsymbol{r}_A \; \Psi^*(\boldsymbol{r}, \boldsymbol{r}_2, \boldsymbol{r}_3, ..., \boldsymbol{r}_A) \Psi(\boldsymbol{r}', \boldsymbol{r}_2, \boldsymbol{r}_3, ..., \boldsymbol{r}_A) \quad . \tag{1.2}$$

How might it be measured? Let us consider for the moment the single particle momentum distribution $n(k)$ of nucleons inside a nucleus. $n(k)$ is given by

$$n(k) = \int d\boldsymbol{k}_2 d\boldsymbol{k}_3 ... d\boldsymbol{k}_A |\Phi(\boldsymbol{k}, \boldsymbol{k}_2, \boldsymbol{k}_3, ..., \boldsymbol{k}_a)|^2 \quad , \tag{1.3}$$

where

$$\Phi(\boldsymbol{k}_1, \boldsymbol{k}_2, ..., \boldsymbol{k}_A) = \int d\boldsymbol{r}_1 d\boldsymbol{r}_2 ... d\boldsymbol{r}_A \; e^{-i(\boldsymbol{k}_1 \cdot \boldsymbol{r}_1 + \boldsymbol{k}_2 \cdot \boldsymbol{r}_2 + ... + \boldsymbol{k}_A \cdot \boldsymbol{r}_A)} \; \Psi(\boldsymbol{r}_1, \boldsymbol{r}_2, ..., \boldsymbol{r}_A) \quad . \tag{1.4}$$

If we combine Equations 1.3 and 1.4, then we can see that

$$\begin{aligned} n(k) &= \int d\boldsymbol{r} d\boldsymbol{r}' d\boldsymbol{r}_2 d\boldsymbol{r}_3 ... d\boldsymbol{r}_A \; e^{i\boldsymbol{k} \cdot (\boldsymbol{r} - \boldsymbol{r}')} \; \Psi^*(\boldsymbol{r}, \boldsymbol{r}_2, ..., \boldsymbol{r}_A) \Psi(\boldsymbol{r}', \boldsymbol{r}_2, ..., \boldsymbol{r}_A) \\ &= \int d\boldsymbol{r} d\boldsymbol{r}' \; e^{i\boldsymbol{k} \cdot (\boldsymbol{r} - \boldsymbol{r}')} \rho(\boldsymbol{r}, \boldsymbol{r}') \quad . \end{aligned} \tag{1.5}$$

Here, measuring at large k corresponds to small $|\boldsymbol{r} - \boldsymbol{r}'|$. Through this we might learn about correlations between nucleons if, for some range of momenta, the effects dominate any mean-field structure in the momentum distribution. Calculations tell us that at small momenta ($k < k_F$), the momentum distribution is dominated by single particle effects, so we can learn little about two-body correlations (see Section 4.1). However, at high momenta ($k > k_F$), single particle effects are vanishingly small and all we see are the effects of N-N correlations. Thus, we can indeed study the short-range correlations between nucleons. But how to measure $n(k)$? There are two obvious methods. One is a single nucleon knockout experiment where the knocked-out nucleon is detected in coincidence with the scattered probe. The momentum distribution enters directly into the theoretical derivation of the cross section and thus can be easily extracted. Such experiments with electrons as probes

have been performed and yielded information on the low-momentum component of the distribution (see, for example, Refs. [4,5]). However, given current accelerators, it is not feasible to measure at higher momenta because of very low count rates. This might change with the new generation of acclerators, such as CEBAF which will be continuous beam machines, and thus low count rates will be offset by 100% duty factors (achieving high duty factors is much more important than achieving higher beam intensity, which can actually be detrimental in terms of signal to noise). An alternative is proposed using inclusive, quasielastic electron scattering. These are more practical experiments and, in fact, have already been performed. Here we hope to measure the momentum distribution via a scaling function.

Scaling phenomena have already played an important role in nuclear physics. Quite often when scaling behavior is found, the scaling function bears some relation to a fundamental property of the system under study. If this property is one that can be studied more easily by other techniques, then effort is likely wasted. *But*, if the property cannot be easily studied any other way, then we have a very powerful tool. An example of this is the experimental confirmation of Bjorken scaling in nucleons[6,7]. It provided the proof that hadrons were indeed made up of more fundamental constituents. Also, it showed that these constituents interacted only very weakly with one another at short range, a signal for asymptotic freedom. Both these facts played a very strong role in the development in the currently accepted theory of the strong interactions (QCD). How though can scaling help us measure the single particle momentum distribution of nucleons? West [8] and Kawazoe *et al.* [9] independently analyzed the part of the inelastic electron-nucleus scattering cross section called the quasielastic peak (see Chapter 2) to show that under a weak interaction hypothesis (similar to Bjorken's), that a scaling function can be extracted which bears a simple relation to the momentum distribution. In fact, the existence of sum rules for structure functions in electron scattering is a strong hint

that scaling can be found (see Sec 2.4). However, they are by no means absolute proof of a scaling phenomenon, and even if such does indeed exist, sum rules can tell us nothing about what the scaling variable is, or what the scaling will tell us.

Another question arises when the scaling is not perfect (this is, in fact, the case for existing experimental data). Experiments are done at finite momentum transfers, while the simplest theoretical predictions work best at infinite momentum transfer. Under experimental conditions, how good is the weak interaction hypothesis? For Bjorken scaling, there are violations of scaling, but these are well modeled by first-order perturbation theory in QCD[10]. In the nucleus, there could still be strong final-state interactions that muddle the analysis. It is not clear that these can be resolved (although we try to do so). Also, nucleons are structured objects of finite size. Are they different in the nuclear medium than in free space? Do their form factors change? None, one, or all of these effects could be significant. This might make it impossible to extract a unique scaling function. Sick [11] and McKeown [12] have already considered the form-factor question, and found that there are strong constraints on nucleon modification in the medium if scaling is to be maintained. In this thesis we consider the other question, whether final-state interactions contribute strongly to the cross section (and thus the scaling function) in the comparison to experimental results. We use nuclear matter as a test medium, because of the ease with which the effects of microscopic interactions can be studied.

This thesis consists of four main sections. In Chapter 2, the formalism for quasielastic electron scattering is reviewed, and the general principles of y-scaling are discussed. The status of theory and experiment (to date) will also be presented. In Chapter 3, we review many-body theory as it applies to nuclear matter, with emphasis on the techniques and assumptions that we will need later on. In Chapter 4, we discuss the structure function of nuclear matter, from the simple approximation relating it to the momentum distribution to the effects of final-state interactions in

a microscopic many-body theory. Comparisons are made to new measurements of the scaling function for various heavy nuclei. In Chapter 5, conclusions are drawn and the possible future directions of theory and experiment will be discussed. Two appendices will discuss algebraic details needed for the calculation.

Chapter 2

Quasielastic Electron Scattering

What does the term "quasielastic" mean? If we study the inclusive inelastic cross section for electron scattering on a nucleus at rest, we can see something quite interesting (Fig. 2.1). Aside from the resonances and deep-inelastic structures, there is a very strong peak centered at $\omega_{el} + \epsilon$, where ω_{el} is the energy transfer for elastic scattering from a free nucleon (this assumes we have picked a kinematic region where the peak is not swamped by overlapping structures). This would seem to indicate that we are scattering from nucleons inside the nucleus, which have separation energy $\mathcal{O}(\epsilon)$. In fact, this is the best evidence we have that nuclei are made up of nucleons! This elasticlike scattering from single nucleons in the nucleus is called quasielastic scattering. More generally it applies to processes where the scattering seems elastic on the constituents of a system, but inelastic on the system. The breadth of the peak is due to the fact that the bound constituents have a continuous distribution of momenta. Thus, one can never transform into a frame where all the constituents are at rest, as in the free elastic scattering case.

Quasielastic scattering (QES) has long been used to determine the momentum distributions of Bose and Fermi systems for low momenta. Moniz *et al.* [14] used the results from quasielastic electron scattering to determine the Fermi momenta for finite nuclear systems, and various groups are now starting to use QES with neutrons to determine the low-momentum properties of liquid ^{3}He [15] and liquid

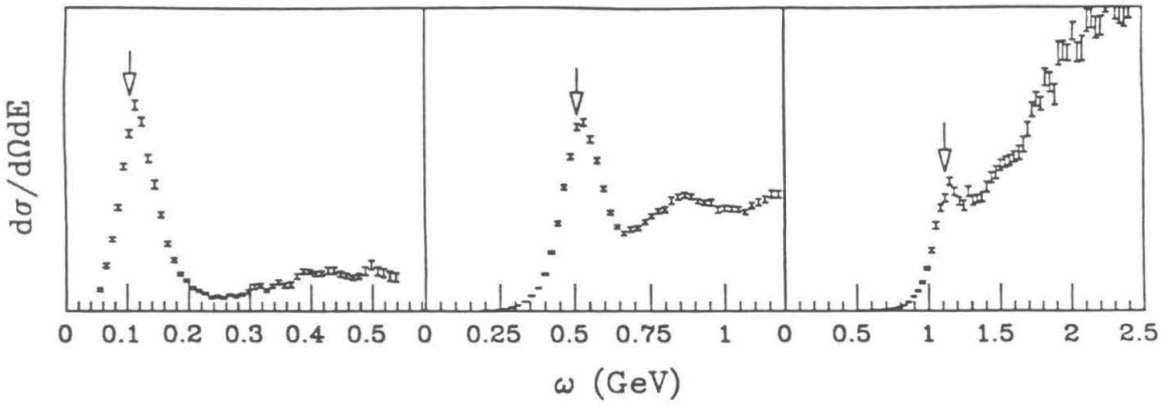

Figure 2.1 Quasielastic scattering cross sections for ^{3}He at 8° for incident electron energies of 3.26, 7.26 and 10.95 GeV. Arrows mark the location for the elastic peak for a free nucleon at the same kinematics. The energy shift in this case is about 8 MeV. It is larger for heavier nuclei (From Ref. [13]).

^{4}He [16]. Recently, people have looked at QES as a tool for determining very high momentum components of the nuclear wavefunction, in turn looking at the short-range correlations of the nucleon-nucleon interaction[8,17,18].

The analysis by West in 1975[8] spawned much of the current experimental and theoretical work in QES from nuclei. He demonstrated in a simple model that the relationship between the measured cross section and the nuclear momentum distribution could be given by a single variable. The idea was analogous to Bjorken x-scaling in the nucleon structure function[6] (but different in spirit) and was labeled y-scaling. The first measurements of QES cross sections sensitive to high momentum components of the nuclear wavefunction were done by Schütz *et al.* on ^{2}H[19], and Day *et al.* on ^{3}He[13]. Both sets of data were analyzed for scaling behavior as predicted by West, and indeed there were only minor deviations from complete scaling[17,18]. Agreement with theoretical calculations was not good at this stage (this will be discussed in Sec. 2.5). A proposal was made to the then newly formed

NPAS (Nuclear Physics At SLAC) program for an experiment that would look for y-scaling in heavy nuclear systems, using targets of ^{4}He, ^{12}C, ^{27}Al, ^{56}Fe, and ^{197}Au.

2.1 Elementary Electron Scattering Theory

We need to develop the formalism for the scattering of electrons from a nucleus. We consider only the Born (or one-photon exchange) approximation with plane waves for the incident and final-state electron. Also, the electron mass is negligible compared to the kinetic energies being considered (0.5 MeV versus approximately 3 GeV), so it is neglected.

We start with the Feynman diagram for the one-photon exchange process for electron scattering from a nucleus (Fig. 2.2) (the conventions used will be those of Bjorken and Drell[20]).

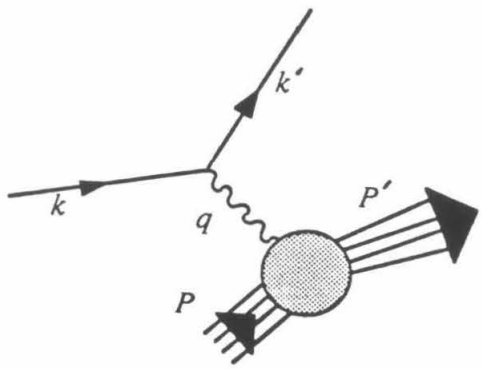

Figure 2.2 Feynman diagram for electron scattering from a nucleus at the one-photon exchange level.

Energy and momentum are conserved at each vertex. k (k') labels the four momentum of the initial (final) state electron, and $P(P')$ labels the four momentum of the initial (final) target state. q is the four-momentum transfer of the scattering reaction. The exact definitions of these (to be used throughout this thesis) are

$$\boldsymbol{q} = \boldsymbol{k} - \boldsymbol{k}', \quad \omega = E_i - E_f, \quad q = (\omega, \boldsymbol{q}), \quad Q^2 \equiv -q^2 = \boldsymbol{q}^2 - \omega^2 \quad . \tag{2.1}$$

Another useful relation gives the momentum transfer in relation to the electron energies and scattering angle as

$$Q^2 = 4EE' sin^2 \frac{\theta}{2} \, . \tag{2.2}$$

We consider the target to be a nucleus of mass M_A at rest. We assume we know its spin state, and also that we know its final-state after scattering. In this case, we write the differential cross section as

$$d\sigma = \frac{2\alpha^2}{q^4}\frac{d\boldsymbol{k}'}{EE'}\eta_{\mu\nu}W^{\mu\nu} \quad , \tag{2.3}$$

where $\eta_{\mu\nu}$ is the leptonic tensor, written as

$$\begin{aligned}\eta_{\mu\nu} &= 2EE'\frac{1}{2}\sum_{s_i}\sum_{s_f}\bar{u}(k)\gamma_\mu u(k')\bar{u}(k')\gamma_\nu u(k) \\ &= k_\mu k'_\nu + k'_\mu k_\nu - k\cdot k' g_{\mu\nu} \quad ,\end{aligned} \tag{2.4}$$

where $u(k)$ is a Dirac spinor, and the sum over spins is performed using trace techniques. $W^{\mu\nu}$ is the hadronic tensor, written in terms of the nuclear currents as

$$W^{\mu\nu} = \langle 0|J^\mu(0)|f\rangle\langle f|J^\nu(0)|0\rangle\,(2\pi)^3\delta^4(P' - P + q) \quad . \tag{2.5}$$

The initial and final electron energies and momenta are (relatively) easily measured, and the initial state of the target is assumed to be known. The only problems arise in the final-state of the target. If we wish to know about the exact final-state, it must be measured in the experiment. The experimentalist then has the problem of detecting all particles over a solid angle of 4π. What is sometimes done is to detect one or two particles of the final-state in coincidence with the final-state electron; but this still has problems with very low count rates. $(e, e'p)$ experiments have been performed at Saclay and NIKHEF (Refs. [4,5]) for relatively low energies, and Donnelly[21] has calculated the characteristics of the cross section for detection of n-particles in coincidence with the final-state electron.

West's derivation of y-scaling involved what is known as the inclusive cross section, meaning that the final-state of the target is undetermined. Practically, this means that all final-states are possible and must be summed over in a theoretical calculation.

2.2 Derivation of the Inclusive Cross Section

If we sum over the final-states in Eq. 2.5 (Lorentz invariance and current conservation are taken into account), then the most general form for $W^{\mu\nu}$ is

$$W^{\mu\nu} = -W_1(q^2, q\cdot P)\left(g^{\mu\nu} - \frac{q^\mu q^\nu}{q^2}\right) + W_2(q^2, q\cdot P)\frac{1}{M_A^2}\left(P^\mu - \frac{P\cdot q}{q^2}q^\mu\right)\left(P^\nu - \frac{P\cdot q}{q^2}q^\nu\right) \tag{2.6}$$

(this assumes that we have a spin zero target, or that we have averaged over initial spin states of the target). The two functions W_1 and W_2 contain information about the structure of the target. There are only two independent variables left at this point, and they are generally taken to be q^2 and $q\cdot P$. These are both Lorentz scalars, and thus quite general, but we could also have chosen $\boldsymbol{q}$ and ω as our two variables. These will be used later on when we restrict ourselves to the lab frame. We can now collapse the tensor structure of the cross section to a simpler form

$$\frac{d^2\sigma}{dE'd\Omega'} = \sigma_M\left(W_2 + 2W_1\tan^2\frac{\theta}{2}\right) \quad , \tag{2.7}$$

where

$$\sigma_M = \frac{\alpha^2\cos^2\theta/2}{4E^2\sin^4\theta/2} \tag{2.8}$$

is the Mott cross section for elastic scattering of a point Dirac particle. A slight manipulation of the structure functions gives an alternate form

$$\frac{d^2\sigma}{dE'd\Omega'} = \sigma_M\left(\left(\frac{Q^2}{\boldsymbol{q}^2}\right)^2 W_L(q, q\cdot P) + \frac{1}{2}\left(\frac{Q^2}{\boldsymbol{q}^2} + 2\tan^2\frac{\theta}{2}\right)W_T(q, q\cdot P)\right) \quad , \tag{2.9}$$

where $W_{L(T)}$ represents the longitudinal(transverse) structure function. These can be defined in terms of W_1 and W_2 as

$$W_L = \left(\frac{\boldsymbol{q}^2}{Q^2}\right)^2 W_2 - \left(\frac{\boldsymbol{q}^2}{Q^2}\right)W_1$$
$$W_T = 2W_1\,.$$

These labels indicate which part of the photon polarization the nuclear current has coupled to.

2.3 The Impulse Approximation

Fig. 2.3 shows the Feynman diagram for the quasielastic process if we assume that it is dominated by single nucleon knockout.

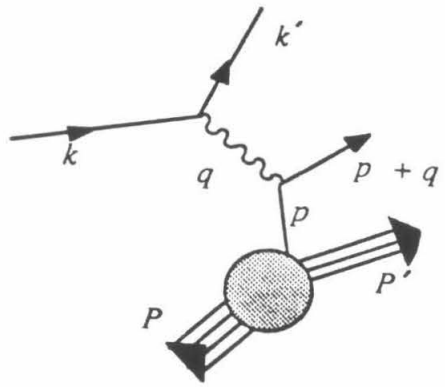

Figure 2.3 Feynman diagram for single nucleon knockout. Final-state interactions are ignored at this level.

Energy-momentum conservation at the nuclear vertex gives us

$$\omega + M_A = \sqrt{(\boldsymbol{q}+\boldsymbol{p})^2 + M^2} + \sqrt{\boldsymbol{p}^2 + \overline{M}_{A-1}^2} \quad , \tag{2.10}$$

where M_A is the mass of the target nucleus, M is the nucleon mass, $\boldsymbol{p}$ is the momentum of the struck nucleon (and also of the recoiling fragment), and $\overline{M}_{A-1}$ is the mass of the recoil fragment. The latter term is the major unknown here.

Since we have summed over final-states, and the target is in its ground state, Eq. 2.5 reduces to a ground-state expectation value

$$W^{\mu\nu} = \frac{1}{2\pi}\mathrm{Re}\int d^4x e^{iq\cdot x}\langle 0|T(J^\mu(x)J^\nu(0))|0\rangle \quad , \tag{2.11}$$

where $T(AB)$ represents the time-ordered product of A and B. This is now in the form of a forward Compton amplitude. The simplest representation of this is the absorption by a nucleon in the target of a photon at time 0, and the emission of a photon with the same quantum numbers by the same nucleon at time x_0 later (Fig. 2.4).

This simple model is the Impulse Approximation (IA). It assumes that there is

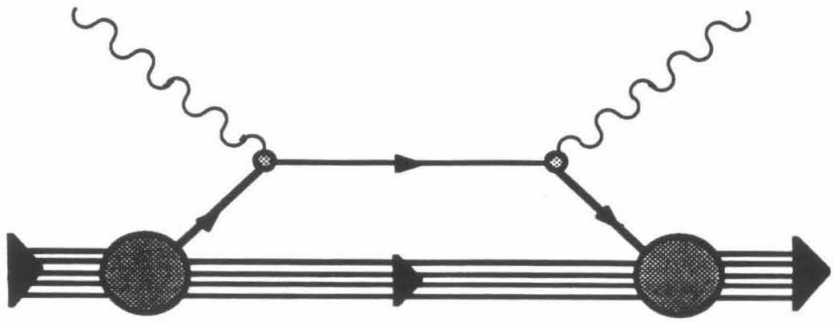

Figure 2.4 Feynman diagram for forward Compton scattering from a nucleus. In this figure, the photon is absorbed and emitted by the same nucleon. No interactions are allowed in the intermediate state.

no intermediate state interaction, and that the whole process takes place on one nucleon with the rest of the nucleus purely in a spectator role. An extended and more generalized version of IA allows a second Compton amplitude to contribute to the result (Fig. 2.5), but as we will see later, its contribution falls off very rapidly with q.

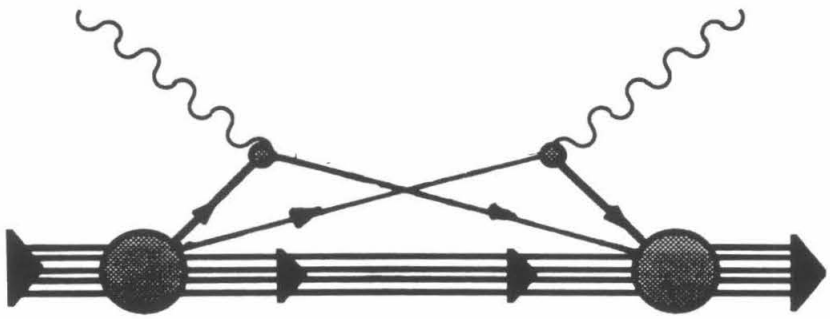

Figure 2.5 Same as Fig. 2.4 except that the photon is absorbed by one nucleon and emitted by another.

2.4 Scaling in Nuclear Targets

To derive the scaling function for QES, it is simplest to start with the non-relativistic approximation to the cross section (This follows West [8]). Here

$$\frac{d^2\sigma}{dE'd\Omega'} = \sigma_R Z S(q,\omega) \quad , \tag{2.12}$$

where σ_R is the Rutherford cross section. $S(q,\omega)$ is the pure charge scattering limit of W_L/Z (Z is the number of charges), defined as

$$S(q,\omega) = \frac{1}{A\pi}\mathrm{Re}\int_0^\infty dt\, e^{i\omega t}\langle 0|\rho^\dagger(\boldsymbol{q},t)\rho(\boldsymbol{q},0)|0\rangle \; . \tag{2.13}$$

(Note that isospin is left out in this derivation, and that all particles are assumed to take part in the interaction) S is generally called the "dynamic structure factor" for the many-body system. $\rho(\boldsymbol{q},t)$ is the operator for injecting a momentum $\boldsymbol{q}$ at time t into the system, defined as

$$\rho(\boldsymbol{q},t) = \sum_{\boldsymbol{k}} a^\dagger_{\boldsymbol{k}+\boldsymbol{q}}(t)a_{\boldsymbol{k}}(t) \quad . \tag{2.14}$$

We can remove the time dependence of ρ by rewriting it as

$$\rho(\boldsymbol{q},t) = e^{iHt}\rho(\boldsymbol{q},0)e^{-iHt} \quad . \tag{2.15}$$

ρ can now be written in terms of momentum states for an A-body system as

$$\rho(\boldsymbol{q},t) = \frac{1}{(2\pi)^{3A}}\sum_i \int d\boldsymbol{k}_1 ... d\boldsymbol{k}_A\, e^{-iHt}|\boldsymbol{k}_1,...,\boldsymbol{k}_i+\boldsymbol{q},...,\boldsymbol{k}_A\rangle\langle\boldsymbol{k}_1,...,\boldsymbol{k}_i,...,\boldsymbol{k}_A|\, e^{iHt} \; . \tag{2.16}$$

Inserting this into Eq. 2.13 allows us to write S as

$$\begin{aligned} S(q,\omega) = & \frac{1}{A\pi}\frac{1}{(2\pi)^{6A}}\mathrm{Re}\int dt\, e^{i\omega t}\int d\boldsymbol{k}_1 ... d\boldsymbol{k}_A d\boldsymbol{p}_1 ... d\boldsymbol{p}_A \\ & \sum_{i,j}\langle 0|e^{iHt}|\boldsymbol{k}_1,...,\boldsymbol{k}_A\rangle \\ & \langle\boldsymbol{k}_1,...,\boldsymbol{k}_i+\boldsymbol{q},...,\boldsymbol{k}_A|e^{-iHt}|\boldsymbol{p}_1,...,\boldsymbol{p}_j+\boldsymbol{q},...,\boldsymbol{p}_A\rangle \\ & \langle\boldsymbol{p}_1,...,\boldsymbol{p}_A|0\rangle \quad . \end{aligned} \tag{2.17}$$

Now we need some information on the Hamiltonian. To keep things simple, we will ignore any momentum dependence of the potential energy term. Thus, if

$$H = \sum_{i=1}^{A} \frac{\boldsymbol{p}_i^2}{2M} + V(1,...,A) \quad , \tag{2.18}$$

then we can write

$$\begin{aligned} H\langle \boldsymbol{p}_1,..,\boldsymbol{p}_i+\boldsymbol{q},..,\boldsymbol{p}_A|0\rangle &= \Big(\sum_{j\neq i} \frac{\boldsymbol{p}_j^2}{2M} + \frac{(\boldsymbol{p}_i+\boldsymbol{q})^2}{2M} + V(1,...,A)\Big)\langle \boldsymbol{p}_1,...,\boldsymbol{p}_i+\boldsymbol{q},...,\boldsymbol{p}_A|0\rangle \\ &= (E_0 + \frac{2\boldsymbol{p}_i\cdot\boldsymbol{q}+\boldsymbol{q}^2}{2M})\langle \boldsymbol{p}_1,..,\boldsymbol{p}_i+\boldsymbol{q},..,\boldsymbol{p}_A|0\rangle \quad , \end{aligned} \tag{2.19}$$

where E_0 is the energy of the initial state, given by

$$H\langle \boldsymbol{p}_1,..,\boldsymbol{p}_A|0\rangle = E_0\langle \boldsymbol{p}_1,..,\boldsymbol{p}_A|0\rangle \quad . \tag{2.20}$$

After some very straightforward algebra, we can evaluate the integral over time in Eq. 2.17 and also most of the momentum integrals to find

$$\begin{aligned} S(q,\omega) = \frac{M}{q}\Big(&\int_{-q/2+M\omega/q}^{\infty} \frac{kdk}{(2\pi)^2} n(k) \\ &+ \int_{-q/2+M\omega/q}^{\infty} \frac{kdk}{(2\pi)^2}\frac{d\boldsymbol{k}'}{(2\pi)^3} f(\boldsymbol{k},\boldsymbol{k}';\boldsymbol{q})\Big) \end{aligned} \tag{2.21}$$

as the final result for the structure factor, where $n(k)$ is the momentum distribution as defined in Chapter 1 (normalized to unity) and $f(\boldsymbol{k},\boldsymbol{k}';\boldsymbol{q})$ is the two-body momentum space correlation function, written as

$$f(\boldsymbol{k},\boldsymbol{k}';\boldsymbol{q}) = (A-1)\int \frac{d\boldsymbol{k}_3}{(2\pi)^3}...\frac{d\boldsymbol{k}_A}{(2\pi)^3}\langle 0|\boldsymbol{k},\boldsymbol{k}'+\boldsymbol{q},\boldsymbol{k}_3,...,\boldsymbol{k}_A\rangle\langle \boldsymbol{k}+\boldsymbol{q},\boldsymbol{k}',\boldsymbol{k}_3,...,\boldsymbol{k}_A|0\rangle \ . \tag{2.22}$$

The first term of Eq. 2.21 corresponds to the Compton amplitude of Fig. 2.4, and gives the naive result expected from IA. The second term corresponds to Fig. 2.5. In a simple single-particle model it falls off very sharply with q[8]. We will examine the strength of this term for nuclear matter in Chapter 4. If we now define a new variable y as $y = -q/2 + M\omega/q$, then we can see that

$$S(q,\omega) = \frac{M}{q}\Big(F(y) + F_c(y,q)\Big) \ , \tag{2.23}$$

so that in the limit $Q^2 \to \infty$, qS becomes a function of the single variable y. This is scaling! West's original motivation for this calculation likely came from sum rules. If we consider the coulomb sum rule for S

$$\lim_{Q^2 \to \infty} \int_{\omega_{el}}^{\infty} S(q,\omega) d\omega = 1 \,, \tag{2.24}$$

then we can change variables from ω to y to see that

$$\lim_{Q^2 \to \infty} \int_{\infty}^{\infty} qS(q,y) dy = M \,. \tag{2.25}$$

The fact that this integral is finite and independent of q indicates that qS does indeed become a function of the single variable y. This is valid only as a check, since the existence of the sum rule alone makes it possible to define an arbitrary number of variable transforms, all of which could (or could not) really scale. The detailed analysis is required to confirm whether or not a scaling variable can be found.

Many authors have generalized West's derivation beyond what is equivalent to a naive Fermi gas model[17,22]. This mainly involved replacing the energy-conserving delta function with a more general form, and ignoring the correlation term, which is known to be very small. The structure factor is now written as

$$S(q,\omega) = \int \frac{d\boldsymbol{k}}{(2\pi)^3} n(k) \delta(\omega + E_0 - E_f) \,. \tag{2.26}$$

E_0 is taken as the initial energy of the nuclear system (M_A), and E_f is the sum of the final-state energy of the struck nucleon, and the recoil energy of the residual nucleus. We will now work with relativistic kinematics. The latter is generally written as

$$E_f = \sqrt{(\boldsymbol{k}+\boldsymbol{q})^2 + M^2} + \sqrt{\boldsymbol{k}^2 + \overline{M}_{A-1}^2} \,, \tag{2.27}$$

where $\overline{M}_{A-1}$ is the mass of the residual nucleus– possibly in an excited state. The integration over the delta function is then done with respect to the angle between $\boldsymbol{k}$ and $\boldsymbol{q}$ ($\theta_{\boldsymbol{kq}}$). Given q and ω, and the fact that $|\cos\theta_{\boldsymbol{kq}}|$ is bounded by one, then

there is a restricted set of allowed values of k ($k_{min} < k < k_{max}$). The form of the structure factor is then

$$S(q,\omega) = \left|\frac{\partial k_{||}}{\partial \omega}\right| \int_{k_{min}}^{k_{max}} \frac{dk}{(2\pi)^2} n(k)\,, \tag{2.28}$$

where $k_{||} = k\cos\theta_{\boldsymbol{kq}}$. In strict analogy to West's derivation, y is defined as $k_{||}$. The equation for y is then

$$\omega + M_A = \sqrt{(y+q)^2 + M^2} + \sqrt{y^2 + M_{A-1}^2}\,, \tag{2.29}$$

where transverse components of k have been neglected as small. Using Eqs. 2.27 and 2.29, we find that $k_{min} \approx |y|$ and $k_{max} \approx |y+2q|$. Now we see an explicit dependence on q of the structure factor, which might give us deviations from scaling at finite Q^2. When $y \approx -q$, then the scaling function necessarily goes to zero. Thus there are now kinematic cutoffs that were simply not present in West's model.

If we are to work in a relativistic framework, there are some things that must be worried about before we can predict scaling. Before, we had simple coulomb scattering. Now there is a second structure function, W_T, which contains information on the electron coupling to magnetic moments of both the neutrons and the protons, as well as on coupling to the convection current created by the moving protons. To study this we can use the Fermi gas model of Moniz[14]. Here, the nucleus is considered as a non-interacting gas of fermions, with filled states up to the Fermi level k_F. The struck nucleon must have momentum $k < k_F$ in the initial state, and $k' > k_F$ in the final-state. We can write down W_L and W_T as

$$W_L = \frac{3M_T}{4\pi A k_F^3}\frac{\boldsymbol{q}^2}{Q^2}\int d\boldsymbol{k}\frac{\delta(\omega + E_i - E_f)\Theta(k_F - k)\Theta(|\boldsymbol{k}+\boldsymbol{q}| - k_F)}{\sqrt{k^2+M^2}\sqrt{(\boldsymbol{k}+\boldsymbol{q})^2+M^2}}$$
$$\times\left[\frac{T_2(Q^2)}{M^2}\left(\frac{\boldsymbol{q}^2}{Q^2}\right)\left(\sqrt{k^2+M^2} - \frac{\omega}{|\boldsymbol{q}|}\boldsymbol{k}\cdot\hat{\boldsymbol{q}}\right)^2 - T_1(Q^2)\right] \tag{2.30}$$

$$W_T = \frac{3M_T}{2\pi A k_F^3}\int d\boldsymbol{k}\frac{\delta(\omega + E_i - E_f)\Theta(k_F - k)\Theta(|\boldsymbol{k}+\boldsymbol{q}| - k_F)}{\sqrt{k^2+M^2}\sqrt{(\boldsymbol{k}+\boldsymbol{q})^2+M^2}}$$
$$\times\left[T_1(Q^2) + \frac{1}{2M^2}T_2(Q^2)(k^2 - (\boldsymbol{k}\cdot\hat{\boldsymbol{q}})^2)\right]. \tag{2.31}$$

T_1 and T_2 are linear combinations of the nucleon form factors, and only depend on Q^2 (T_1 is, in fact, proportional to Q^2). Looking at W_T, we see that there is a second structure factor S' which must be considered, defined as

$$S'(q,\omega) = \left|\frac{\partial k_{||}}{\partial \omega}\right| \int_{k_{min}}^{k_{max}} \frac{k dk}{(2\pi)^2} n(k)(k^2 - (\boldsymbol{k}\cdot\hat{\boldsymbol{q}})^2) \,. \tag{2.32}$$

If this is comparable to $Q^2 S$, then the scaling derivation no longer holds, and scaling should not be observed experimentally. Fortunately, this is not a problem. We can study the effects of convection currents using the Fermi Gas model of Moniz [14], and for the Q^2 and y's considered, the convection current contributions are only a few percent (Fig. 2.6).

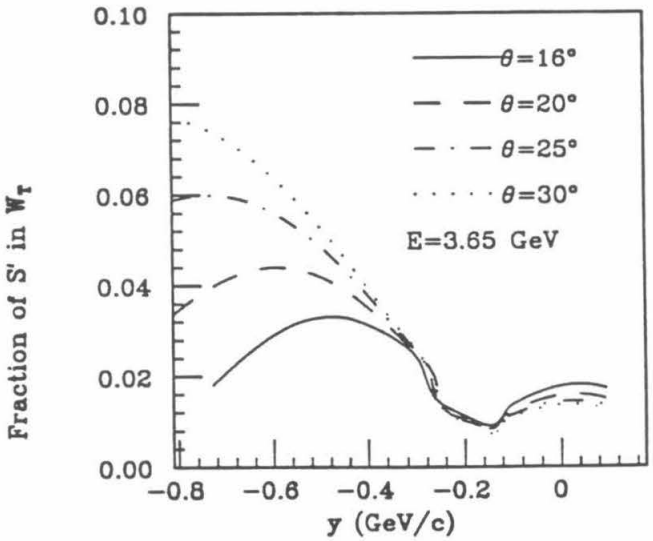

Figure 2.6 The fraction of the structure function W_T due to the structure factor S'. This is calculated using the Fermi gas model of Moniz [14], but using a momentum distribution which has a correlation tail for $k > k_F$. The larger the angle, the larger the value of Q^2.

2.5 Overview of World's Results

There have already been a number of experiments performed whose data sets can be used to look for y-scaling in nuclei. The first were on light systems such as ^{2}H and ^{3}He, and more recently an experiment has been performed on the heavier nuclei. These have all been performed at the highest Q^2 feasible for extraction of a scaling function. Many more experiments have been performed at low Q^2, but it is fairly certain that a scaling analysis is far from reasonable there. Correlation effects certainly still dominate [23] and are considered the solution to problems with the experimental verification of the coulomb sum rule[24,25].

The major experiments have all been performed at SLAC, the latest as part of the Nuclear Physics At SLAC (NPAS) program. The analysis by Sick *et al.* [17] of the scaling function of ^{3}He at high Q^2 and out to large $|y|$ was the first real test of the scaling hypothesis. Previous scaling analyses had all been at too low a Q^2 for the Impulse Approximation to be even naively considered valid[26]. The initial data set used by Sick showed a reasonable scaling function out to $y = -1$ GeV/c, with some rather significant discrepancies around -0.2 GeV/c (Fig. 2.7) It should be noted here that scaling analyses only study the region $y < 0$. This corresponds to the low ω side of the quasielastic peak, where we believe that inelastic effects such as meson-exchange currents, internal nucleon excitations and deep-inelastic structure are not significant (which they are for $y > 0$ as can be seen by the obvious lack of scaling in the experimental results). Later analyses by Sick using the data sets of Refs. [13] and [27] removed these deviations[11] (Fig. 2.8). Soon after, Bosted *et al.* investigated the scaling function for ^{2}H for roughly the same Q^2 and y, and found that scaling did indeed occur [18] (Fig. 2.9). Theoretical agreement with the ^{2}H data is quite good, but it is quite horrendous for the case of ^{3}He. Calculations of the scaling function using Faddeev wavefunctions are a factor of 10 too small at large $|y|$[17], and do not even agree in the $Q^2 \rightarrow \infty$ limit[29,30]. Variational calculations agree

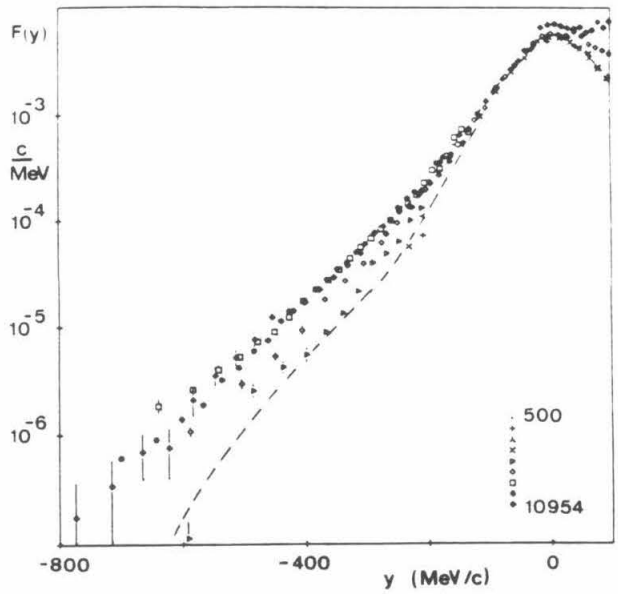

Figure 2.7 $F(y)$ extracted from the inclusive quasielastic cross section for electron scattering on ^{3}He. Theoretical curve is the result of a Faddeev calculation using the Reid Soft Core potential [28] (from Ref. [17]).

in the asymptotic limit[31,22], but also fail to reproduce the approach to scaling (Fig. 2.10). Even the good agreement with the ^{2}H data is somewhat dubious, in that the agreement is in the asymptotic limit, and the approach to scaling still disagrees. The ^{3}He data suffer another problem. Rather than use the kinematic term $\partial\omega/\partial k_{||}$, Sick *et al.* use $\partial\omega/\partial y$. Using Eqns. 2.29 and 2.27, we can see that these two expressions are *very* different at finite Q^2, with

$$\frac{d\omega}{dy} = \frac{q+y}{\sqrt{(q+y)^2+M^2}} + \frac{y}{\sqrt{y^2+M_{A-1}^2}} \tag{2.33}$$

$$\frac{d\omega}{dk_{||}} = \frac{q}{\sqrt{(q+y)^2+M^2}}\,, \tag{2.34}$$

and that each one can change the approach to scaling dramatically. For a heavy system, the ratio of Eqn. 2.33 to Eqn. 2.34 is given by $(q+y)/q$. At large q, this is one. However, at the finite Q^2 studied, this ratio is quite different from one, as can be seen in Fig. 2.11, where the approach to scaling is studied using both

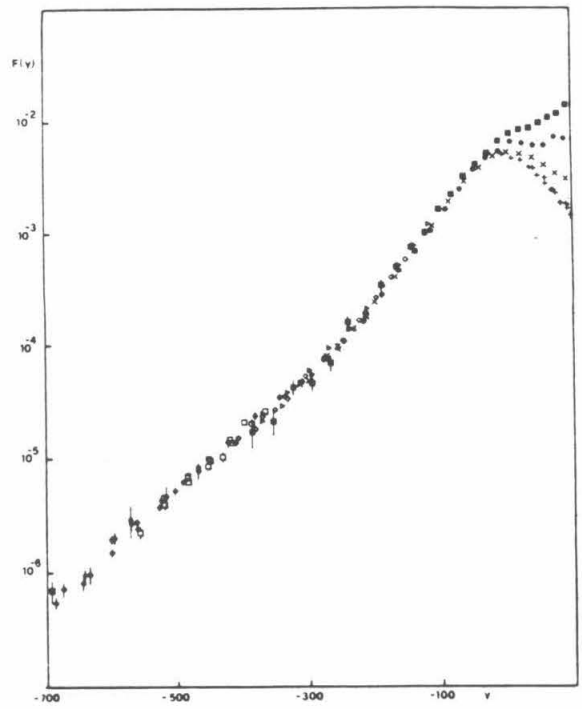

Figure 2.8 Same as Fig. 2.7, except that the data set has been expanded, different kinematic cuts on the data have been made and the definition of y has been modified (from Ref. [11]).

kinematic factors. If the data set is reanalyzed using the correct factor, the scaling function is different from Sick's, and on close analysis, the approach to scaling is from above (Fig. 2.12)[33]. The disagreement between experiment and IA is even more dramatic than before, as IA can do nothing but approach scaling from below.

What can be wrong? It would seem that somehow the Impulse Approximation is still not valid. Then we have to decide what mechanism is causing it to break down. Laget has speculated on the contribution of scattering off quasi-deuteron states in the nucleus, and found strong contributions to the ^{3}He cross section[34]. We can see in Fig. 2.13 that these effects fall rapidly with Q^2, and we will still have the same problems in the asymptotic limit. Frankfurt and Strickman have done a similar calculation in a relativistic framework[35]. Their results are shown in Fig. 2.14. However, all of these are somewhat naive as to how they put the two-body system

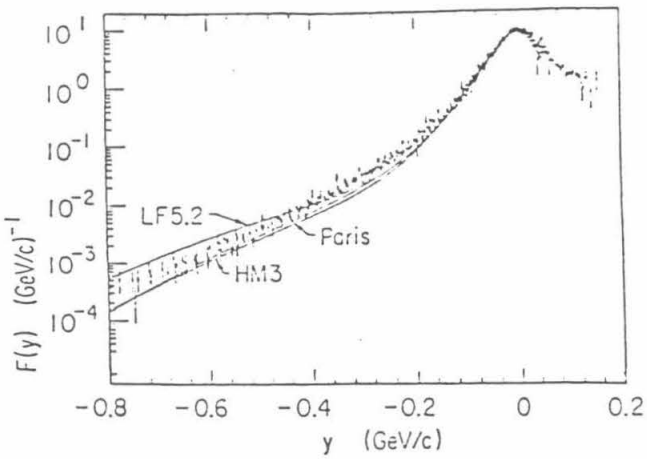

Figure 2.9 $F(y)$ extracted from quasielastic scattering on ^{2}H (from Ref. [18]).

in the nucleus. Another way of thinking about the two-body idea is in terms of final-state interactions. The nucleon that is struck by the virtual photon is strongly correlated with its nearest neighbors. The effects of this are still manifest in the final-state, and the nucleon continues to interact strongly with its neighbors as it moves out of the nucleus. This approach will be discussed in detail in Chapter 4.

The most recent set of data comes from the NE3 experiment at NPAS[32]. They have analysed cross sections for quasielastic scattering off ^{4}He, ^{12}C, ^{27}Al, ^{56}Fe and ^{197}Au. Here the scaling is not as impressive as for the lighter nuclei. For example, the scaling function of ^{12}C is seen in Fig. 2.15 There are strong deviations from scaling at large $|y|$. The different curves all seem to agree rather well at $y = 0$ however, so the effect is not likely due to a mistake in the kinematic definitions. An interesting curve in their paper shows $F(y)$ vs. A at a specific value of y and Q^2. In Fig. 2.16 we see that for large A, $F(y)$ seems to approach an asymptotic limit that we might associate with nuclear matter. This result was obtained after our decision to use nuclear matter as a test medium, and encourages us to believe that any effects we find will indeed be found in real nuclei.

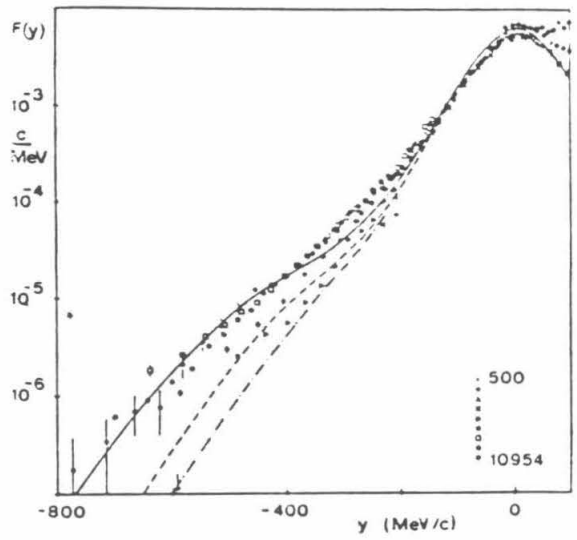

Figure 2.10 Variational calculation of the scaling function $F(y)$ for ^{3}He. The dot-dashed, dashed and solid lines denote calculations at momentum transfers of 5 fm^{-1}, 9 fm^{-1} and ∞ respectively. Note that the asymptotic limit agrees with the experimental results, but that the approach to scaling is still not reproduced (From Ref. [22]).

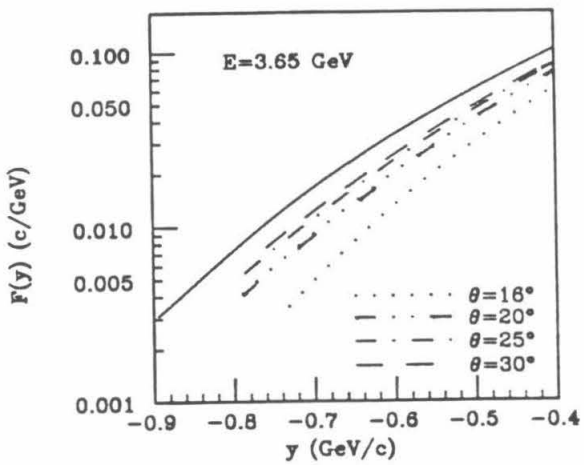

Figure 2.11 An example of the effect on the approach to scaling from using $d\omega/dy$ vs. $d\omega/dk_{||}$ in the Impulse Approximation. The kinematics studied are those of the NE3 experiment[32]. The solid curve is the result of the "correct" analysis for all the kinematics considered, and is also the asymptotic limit of Sick's analysis. We can see that Sick's analysis has not converged to the asymptotic result even at these high Q^2.

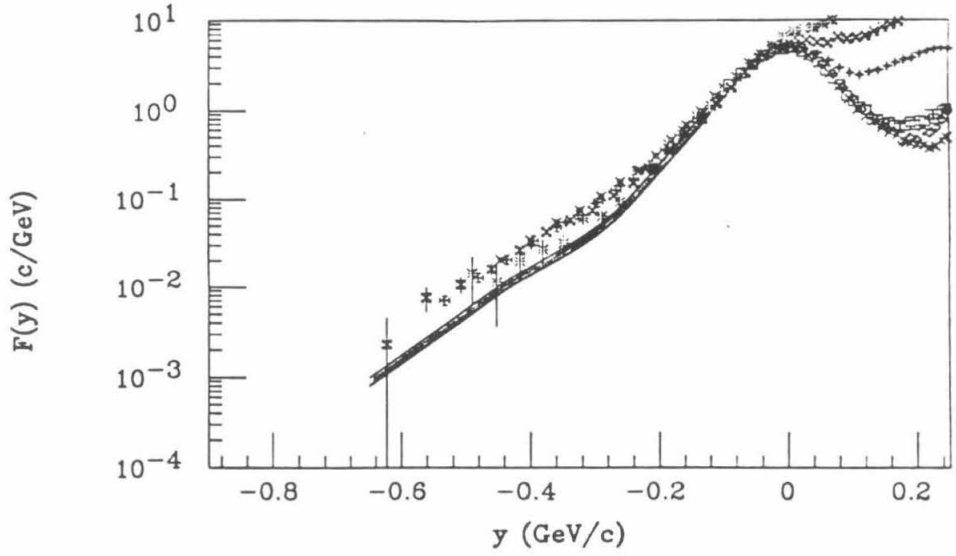

Figure 2.12 The ^{3}He results reanalyzed using the theoretically rigorous kinematic factor of $d\omega/dk_{||}$. The shaded area is the scaling function of Fig. 2.8 (from Ref. [33]).

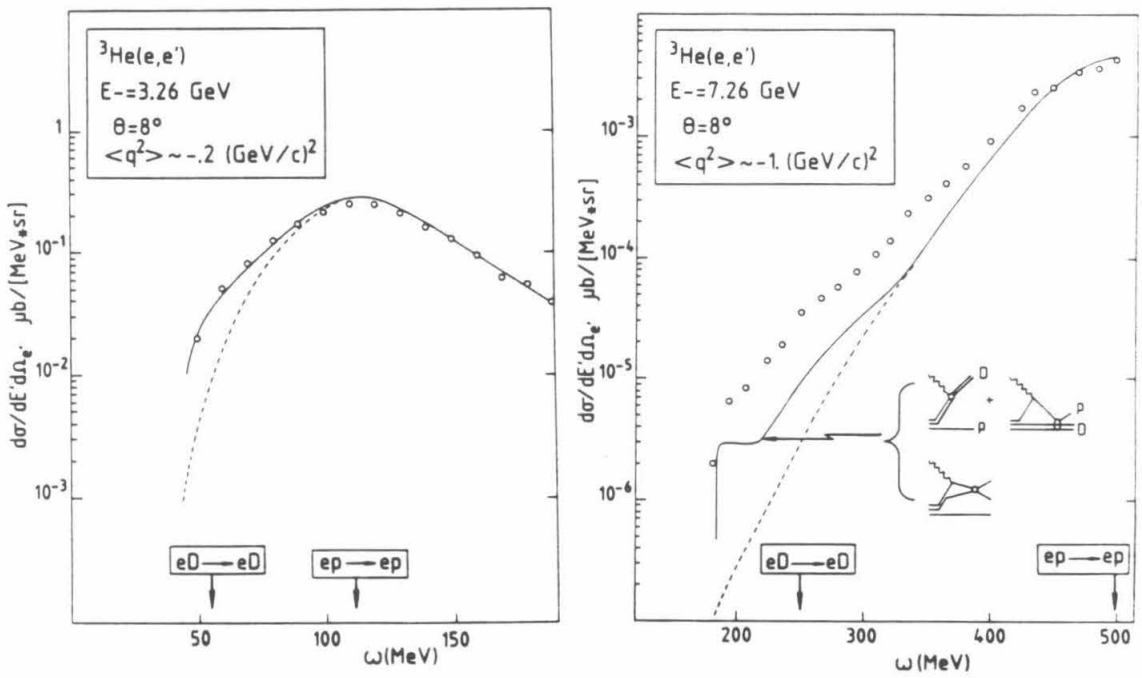

Figure 2.13 Calculation by Laget of the contribution of scattering from quasi-deuterons to the inclusive ^{3}He quasielastic cross section (from Ref. [34]).

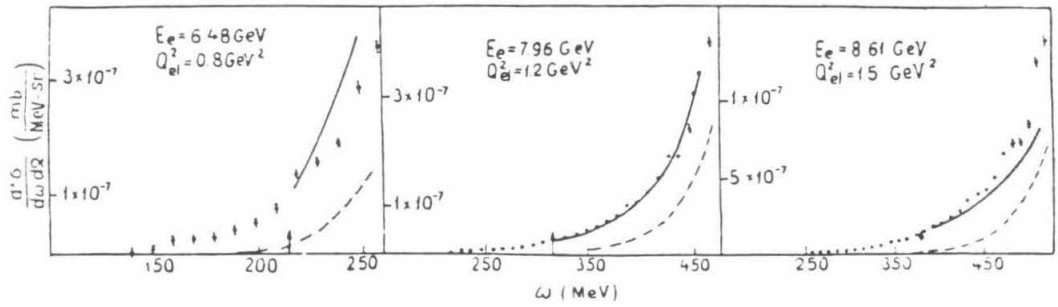

Figure 2.14 Calculation by Frankfurt and Strickman of the contribution of quasi-deuteron scattering in a relativistic framework to the inclusive quasielastic ^{3}He cross section (from Ref. [35]).

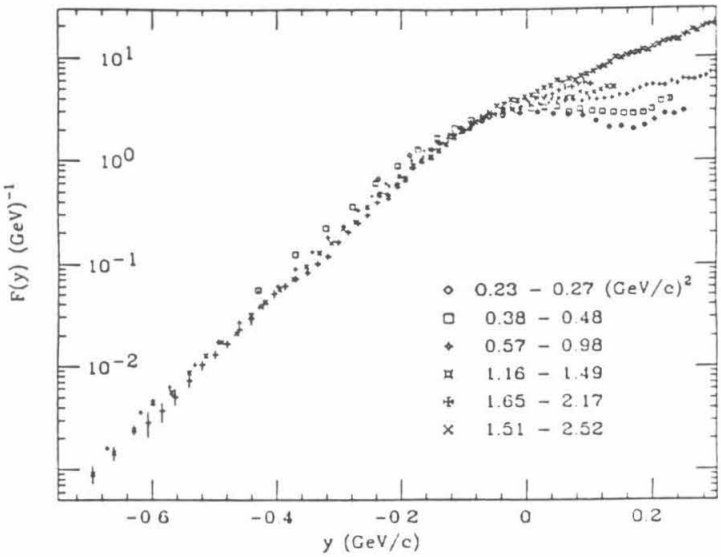

Figure 2.15 $F(y)$ for ^{12}C extracted from the results of the NE3 experiment at SLAC. (From Ref. [32])

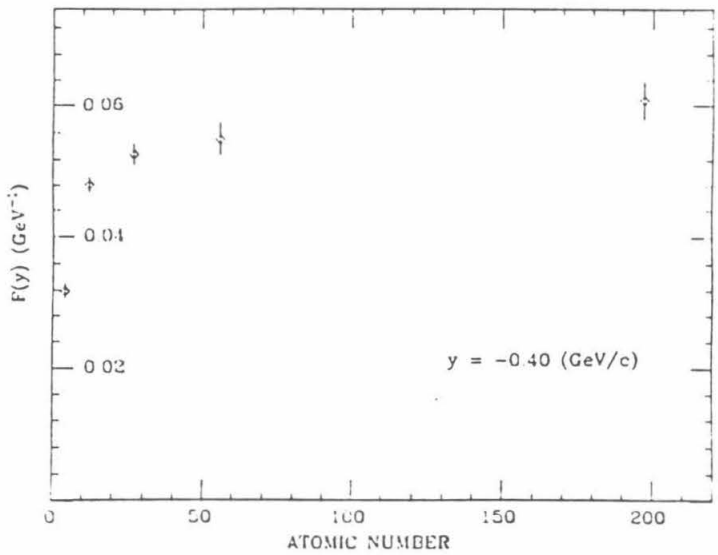

Figure 2.16 The A dependence of the NE3 extracted scaling function at $y = -0.5$ GeV/c. Note how the points appear to approach a constant value for large A (from Ref. [32]).

2.6 Scattering with Other Probes

The elements of y-scaling analysis have been used for probes and targets other than electrons and nuclei. There has been a great deal of work done on neutron scattering off liquid ^{3}He to obtain momentum distributions that look a great deal like Fermi distributions (Fig. 2.17)[15]. Also, the Bose condensate has been searched

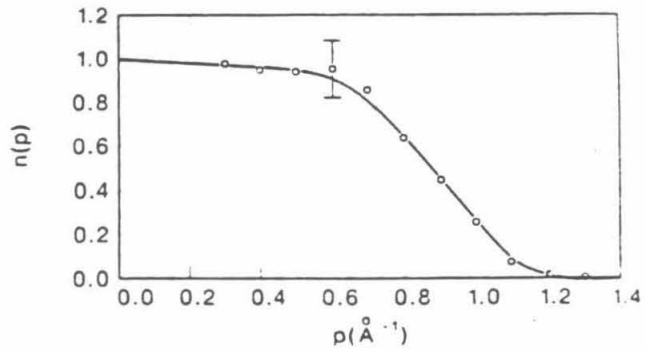

Figure 2.17 Momentum distribution extracted for liquid ^{3}He using quasielastic neutron scattering. The curve through the data corresponds to a Fermi distribution at 1.8 K. The ^{3}He was at 0.37 K (from Ref. [15]).

for in liquid ^{4}He[16], along with the spreading effects due to correlations (Fig. 2.18). These are all still looking at the low-momentum regions of the distributions, where

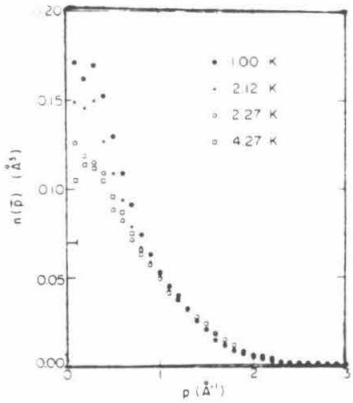

Figure 2.18 The momentum distribution for liquid ^{4}He obtained at various temperatures using quasielastic neutron scattering. The increase in strength near $p = 0$ for decreasing T is interpreted as the onset of a Bose-condensate phase (from Ref. [16]).

the effects of correlations are only weakly seen.

Gurvitz has analyzed pion-nucleus and proton-nucleus scattering data from TRIUMF at lower Q^2[36] and found scaling behavior there also (Fig. 2.19). This is

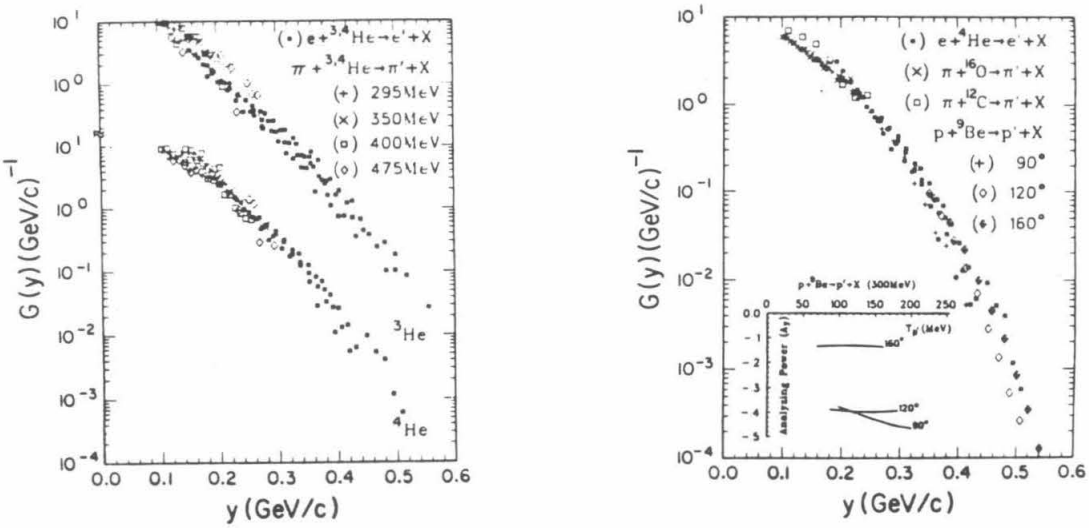

Figure 2.19 Scaling analysis by Gurvitz on π and p inclusive quasielastic scattering cross sections from TRIUMF. The ^{3}He electron scattering results are also shown for comparison (from Ref. [36]).

somewhat surprising given 1) the low Q^2; 2) the strong interaction problems associated with such scattering; and 3) the uncertainty of the real scattering mechanism in the case of the pion. This might almost make one worry that scaling seen experimentally is a nasty trick being played on us by nature, but that seems very unlikely.

Chapter 3

Many-Body Theory for Nuclear Matter

Nuclear physics presents two problems for many-body theorists. Standard techniques for other systems have generally consisted of a perturbation expansion in the two-body interaction using a basis obtained from mean-field theory. The nuclear force contains terms which, when considered in terms of perturbation theory, are of order one or greater. Thus, the perturbation series would not converge at low order. Also, the nuclear interaction contains a hard core of large (in some models infinite) strength. This can have the effect of making the perturbation terms divergent, and will likely make even the finding of a mean-field solution impossible. There were many attempts to bypass these problems, usually by the development of "effective interactions," such as the Wigner [37] or Skyrme [38,39] interactions, which strove to reproduce the observed nuclear properties via a phenomenological, rather than a fundamental, approach. These effective interactions did a reasonable job of reproducing static properties, such as binding energies and charge radii[40,41,42], but it was never clear what their connection to the real underlying physics was. (It is somewhat interesting to note that the Skyrme interaction was shown to be connected to more fundamental models of effective interactions if the Density Matrix Expansion (DME) of Negele and Vautherin is used [43,44].)

The starting point for a more fundamental technique to get around these prob-

lems comes from two-body scattering theory. The problem of divergences also comes in when the scattering problem is considered. A practical solution is found in the T-matrix, calculated from the Lippman-Schwinger equation. It is a non-relativistic technique that reduces the sum over all orders of perturbation theory to a simple integral equation. For many-body systems, the analogy to the T-matrix is the G-matrix. It too represents a sum to all orders of perturbation theory, but also takes into account Pauli blocking of states and the mean-field interaction of a particle with the bulk of the system. It is calculated via the Bethe-Goldstone equation, and the mean field interaction is calculated self-consistently using Brueckner-Hartree-Fock (BHF). The G-matrix changes the perturbation expansion from one in the number of interactions to one in the number of particles that can interact.

The derivation of both T and G-matrix algebra and also their application to real problems will be discussed in this chapter. The representation used for perturbation theory (Goldstone diagrams) will be introduced along with the appropriate rules.

3.1 Strong Interaction Perturbation Theory

Perturbation theory always considers matrix elements of the form $\langle\phi_0|\boldsymbol{A}|\phi_0\rangle$, where ϕ_0 is the unperturbed state, and $\boldsymbol{A}$ represents the perturbation (including propagators and intermediate states). Thus, we always have a situation where we evaluate ground-state expectation values, meaning the initial and final-states are the same. In a Feynman graph, this means that the external legs would match between initial and final-states (except for exchange effects). What Goldstone diagrams do is join up the external legs of equivalent initial and final states, The unperturbed states represent a "sea," which is filled. These states are called "holes." Thus, when we apply the perturbation interaction, the Pauli principle forces the fermions to scatter into unoccupied states (outside the sea) called "particles." Two simple examples are seen in Fig. 3.1. (Note the minus sign in the second diagram, and also the factor

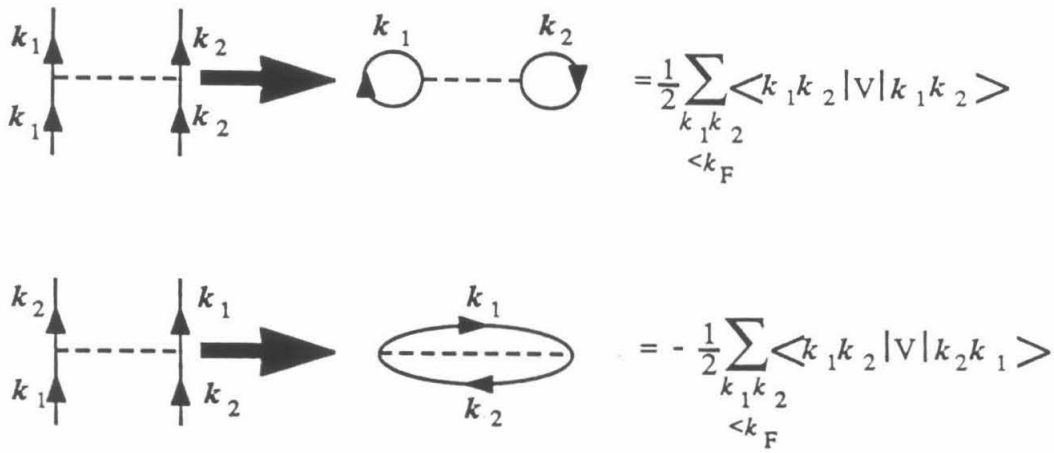

Figure 3.1 Two simple examples of Goldstone diagrams. The second diagram is an "exchange" diagram of the first. The prefactors and signs will be discussed later in the chapter.

of 1/2 which is in both diagrams; these will be explained when general rules for the diagrams are discussed.) Both diagrams above contain only hole states. However, we can also consider other cases, such as the diagram in Fig. 3.2, which have inter-

mediate particle states. Rules for Goldstone graphs come about in a similar way to

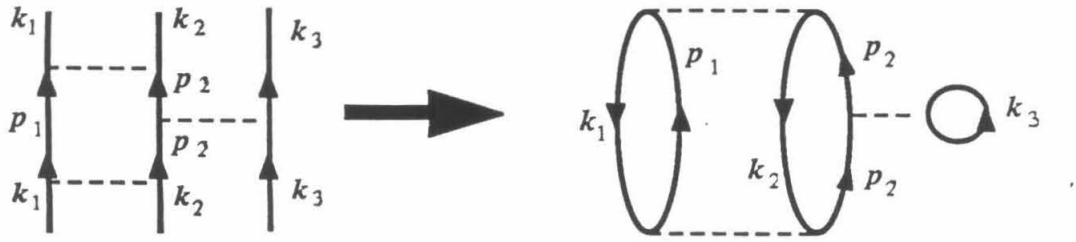

Figure 3.2 A slightly more complicated Goldstone diagram, this one with intermediate states above the Fermi sea.

rules for Feynman diagrams. The perturbation series is analyzed for its behavior under specific circumstances.

1. represents a hole;

2. represents a particle;

3. A propagator, given by $(\sum_{holes} E_h - \sum_{particles} E_p)^{-1}$, appears for the intermediate state between each interaction or operator;

4. A factor of $1/N$, where N is the number of reflections and other geometric operations under which the diagram is invariant

5. The sign of the diagram is $(-1)^{h+e+o}$, where h is the number of hole lines, e is the number of energy denominators and o is the number of one-body-potential operators in the diagram.

3.2 The T- and G-Matrices

The equation for the T-matrix can be derived very simply from diagrams in non-relativistic perturbation theory. T can be written as in Fig. 3.3, summed to all

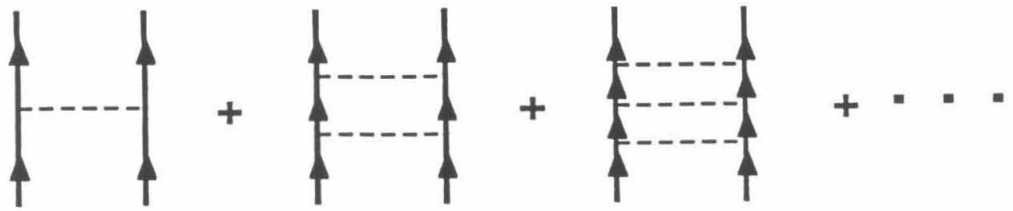

Figure 3.3 The ladder sum for the T-matrix. This series must be summed to all orders in the interaction.

orders. But it is easy to see that this series can be replaced by the truncated summation in Fig. 3.4. This, in diagrams, is what is commonly known as the

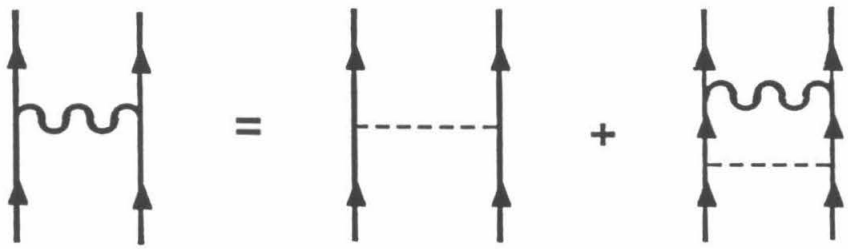

Figure 3.4 The diagrammatic expansion of the Lippman-Schwinger equation. If we iterate on T, we get back the ladder expansion of Fig. 3.3.

Lippman-Schwinger equation. It can be written algebraically as

$$T = V + V G_0 T \,. \tag{3.1}$$

V is the bare interaction, T is the T-matrix and G_0 is the free particle propagator, written as

$$G_0 = \frac{1}{E_0 - H_0 + i\eta} \,, \tag{3.2}$$

where H_0 is the unperturbed Hamiltonian for the interacting particle, and E_0 is some starting energy for the reaction (typically the sum of the energies of the two-particles before interaction), and the imaginary part controls the influence of any singularities that might occur. Off-shell effects are possible, and these would be absorbed into the value of E_0.

If we rewrite the integral equation to solve for T as

$$T = \frac{1}{1 - VG_0} V \tag{3.3}$$

(remembering that this is a matrix equation), then we can see that for V becoming very large, T will likely be well behaved. This allows us to apply perturbation theory in T to problems that would have been unmanageable before.

The derivation of the G-matrix is very similar to that of the T-matrix. The difference now is that, since we are working with a many-particle system, we must take into account Pauli blocking and binding. Also, the "free" Hamiltonian H_1 of the system now will have a potential term that takes into account the mean-field interaction of one particle with all the others. The diagrammatic expansion is the same as for the T-matrix. Algebraically, we can write the equation for the G-matrix as

$$G = V + V \frac{Q}{W - H_1 + i\eta} G \quad . \tag{3.4}$$

The operator Q has the following eigenvalues,

$$Q|\alpha\beta\rangle = \begin{cases} 0 & \text{if } \alpha \text{ or } \beta \text{ is a hole state} \\ |\alpha\beta\rangle & \text{if } \alpha \text{ and } \beta \text{ are particle states,} \end{cases} \tag{3.5}$$

which ensure the Pauli blocking as prescribed. We write H_1 as $H_1 = E_k + U$ (where E_k is the kinetic term and U is the potential term to be defined later), and W is the "starting energy" of the system. It is determined by the structure of the Goldstone graph being considered. To determine W for a given G-matrix, first split up the matrix into its ladder sum and look at the energy denominators that pass through

the sum. Rewriting the denominator as $W - e(\boldsymbol{k}_a) - e(\boldsymbol{k}_b)$ gives us the definition of the starting energy.

3.3 Brueckner-Hartree-Fock for Nuclear Matter

This is a well-studied topic in nuclear physics, and there exist many good review articles on it. We will go through a brief discussion of the topic here, but for further and more detailed discussion, the review articles of Bethe [45], Sprung [46] and Day [47] are highly recommended.

Infinite nuclear matter is a uniform system of nucleons populated equally by neutrons and protons. Also, the coulomb interaction between protons has been turned off. In such a system, translational invariance immediately tells you that the mean-field wavefunctions are plane waves. Thus, our energy eigenstates are states of good momenta. The system obeys Fermi statistics (nucleons are spin 1/2 particles) and (in the non-interacting limit and at zero temperature) fully occupies states up to a momentum k_F, known as the Fermi momentum. This region forms our sea. Above k_F the states are empty. The effect of the two-body interactions to which we apply G-matrix theory is to excite the particles in the sea to momenta above k_F.

In Fig. 3.5 we show the diagram for the scattering of two particles via the G-matrix. Now we need to relate this in more detail to the algebraic structure. The

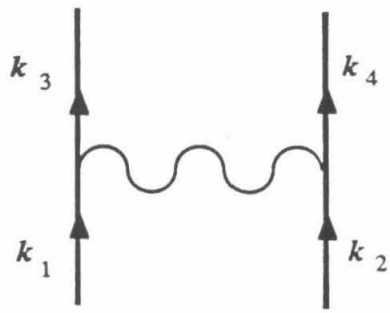

Figure 3.5 The labels associated with an interaction via the G-matrix.

full matrix element for the G-matrix is written as $\langle \boldsymbol{k}_3, \boldsymbol{k}_4 | G(W) | \boldsymbol{k}_1, \boldsymbol{k}_2 \rangle$, where the momenta correspond to the labels in Fig. 3.5. The full expression for the G-matrix

is then

$$\langle \boldsymbol{k}_3, \boldsymbol{k}_4 | G(W) | \boldsymbol{k}_1, \boldsymbol{k}_2 \rangle = \langle \boldsymbol{k}_3, \boldsymbol{k}_4 | V | \boldsymbol{k}_1, \boldsymbol{k}_2 \rangle + \sum_{k_a, k_b > k_F} \frac{\langle \boldsymbol{k}_3, \boldsymbol{k}_4 | V | \boldsymbol{k}_a, \boldsymbol{k}_b \rangle \langle \boldsymbol{k}_a, \boldsymbol{k}_b | G(W) | \boldsymbol{k}_1, \boldsymbol{k}_2 \rangle}{W - e(\boldsymbol{k}_a) - e(\boldsymbol{k}_b)} . \quad (3.6)$$

Now we need to discuss how to define the single-particle energies, or more exactly, the single particle potential. The "standard" definition of the single-particle potential comes from the Hartree-Fock terms in a G-matrix expansion. It can be expressed as

$$U(k) = \frac{1}{4\rho} \sum_{k_1 < k_F} (\langle \boldsymbol{k}, \boldsymbol{k}_1 | G(e(\boldsymbol{k}) + e(\boldsymbol{k}_1)) | \boldsymbol{k}, \boldsymbol{k}_1 \rangle - \langle \boldsymbol{k}, \boldsymbol{k}_1 | G(e(\boldsymbol{k}) + e(\boldsymbol{k}_1)) | \boldsymbol{k}_1, \boldsymbol{k} \rangle). \quad (3.7)$$

The first term is the Hartree direct potential, and the second term gives the Fock term. The diagrammatic expansion is given in Fig. 3.6. Original calculations only

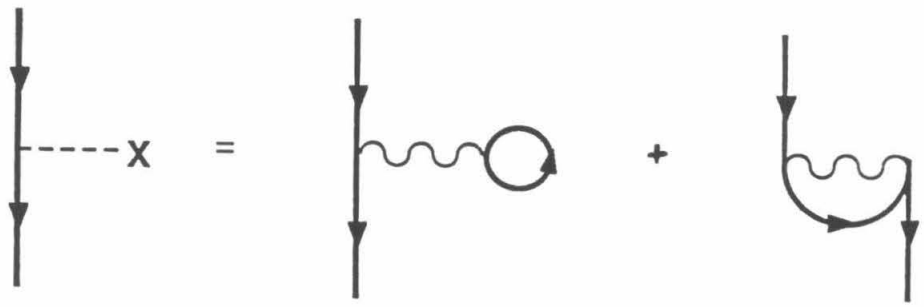

Figure 3.6 The single particle potential calculated in the Hartree-Fock approximation. Here, that corresponds to one-loop order in the hole-lines.

defined a potential for $k < k_F$, with the potential above the Fermi sea identically zero[48]. This avoided the problem of singularities in the propagator and greatly simplified the calculations. However, it is quite easy now to take into account the potential above the Fermi sea as well[49]. This prescription is reasonable only for considering the single particle energies. If the binding energy is wanted, rearrangement terms, like those discussed by Brueckner and Goldman, should be considered

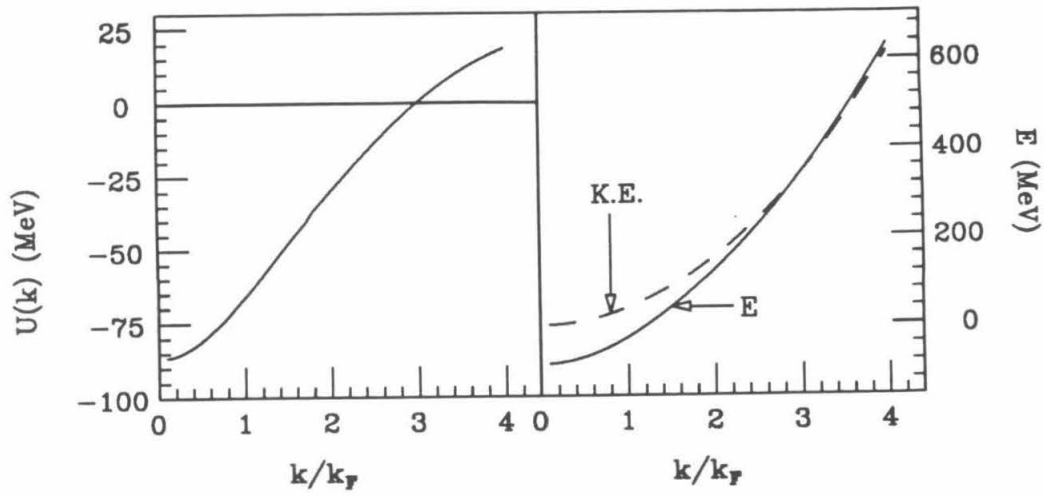

Figure 3.7 Contributions to the separation energy of a particle of momentum k. The single particle potential loses importance very rapidly with increasing k, and at about $k = 2k_F$, it is insignificant with respect to the kinetic energy.

as well[50]. The qualitative behavior of the potential is such that for momenta above $2k_F$, it is insignificant with respect to the kinetic energy term (Fig. 3.7).

The effects of continuing the potential above the Fermi sea can be easily understood. The binding energy/nucleon is increased (due to the suppression of the gap between the hole and particle states), but the saturation density is relatively unchanged.

Another useful quantity for measuring the strength of the two-particle-two-hole interaction is the wound integral. The wound is a measure of the change in the wavefunction due to the interactions. If we define a "defect" as the difference between the real wavefunction and the unperturbed wavefunction between two particles μ and ν as $|\zeta_{\mu\nu}\rangle$, then the wound (κ) is defined as

$$\kappa = 4\rho\langle\zeta_{\mu\nu}|\zeta_{\mu\nu} - \zeta_{\nu\mu}\rangle_{\mathrm{avg}} \,. \tag{3.8}$$

The subscript "avg" denotes that this result is averaged over the Fermi sea. We can find $\zeta_{\mu\nu}$ by again considering the equation for the G-matrix (Eqn. 3.4). The ladder expansion for G is equivalent to the statement that $G|\phi\rangle = V|\psi\rangle$, where

$|\phi\rangle$ is the unperturbed wavefunction, and $|\psi\rangle$ is the true wavefunction. Hence, $|\zeta_{\mu\nu}\rangle = |\psi\rangle - |\phi\rangle$. Let us operate on $|\phi\rangle$ with Eqn. 3.4. This yields

$$G|\phi\rangle = V|\phi\rangle + V\frac{Q}{W - H_1}G|\phi\rangle \,. \tag{3.9}$$

The LHS can be replaced by $V|\psi\rangle$ to give

$$V|\psi\rangle = V|\phi\rangle + V\frac{Q}{W - H_1}G|\phi\rangle \,. \tag{3.10}$$

We can immediately extract from this that

$$|\psi\rangle = |\phi\rangle + \frac{Q}{W - H_1}G|\phi\rangle \,. \tag{3.11}$$

It is now immediately obvious that

$$|\zeta_{\mu\nu}\rangle = \frac{Q}{W - H_1}G|\phi\rangle \,. \tag{3.12}$$

For practical reasons, it is convenient to work in terms of partial wave amplitudes when considering real quantities (The technology for this is discussed in Appendix I). For example, we can write the total wound κ as

$$\kappa = \sum_{\substack{JST \\ LL'}} \kappa_{LL'}^{JST} \,. \tag{3.13}$$

The partial wave amplitudes are given by

$$\kappa_{LL'}^{JST} = \frac{1}{6\pi^3}k_F^3(2J+1)(2T+1)\int \frac{d\boldsymbol{k}'\overline{Q}^2(k',P)|G_{LL'}^{JST}(P;k',k_a)|^2}{(W - e(|\boldsymbol{P}+\boldsymbol{k}'|) - e(|\boldsymbol{P}-\boldsymbol{k}'|))^2} \,, \tag{3.14}$$

and $\boldsymbol{k}_a$ is some "average" relative momentum inside the Fermi sea, and the value that we will use for W is given by $W = e(|\boldsymbol{P}+\boldsymbol{k}_a|) + e(|\boldsymbol{P}-\boldsymbol{k}_a|)$. This is simply the sum of the energies of the two hole states in the expression. In Table 3.1, the breakdown of the wound into partial wave channels is given for both the RSC and Paris potentials. As we will see in Chapter 4, the wound and the momentum distribution of nuclear matter are closely related. Analyzing the wound tells us

which channels most strongly perturb the Fermi gas distribution, and thus, which channels dominate the momentum distribution.

The wound can also be shown to be a good expansion parameter for the perturbation series in hole-lines. It takes the place of a coupling constant in standard theory. If the wound is small, then lowest-order perturbation theory is reasonable, and we need not worry too much about higher-order terms. As we see here, the wound is fairly small, and we can feel fairly confident about truncating the expansion at low order.

Now we can compare the effects of the extended potential on the energy, saturation density and wound integral for each potential. The exact values of the saturation properties are actually fairly sensitive to the number of partial waves considered, and the methods for considering the contributions for higher partial waves. Different authors will produce results that are different by about 5% or less (note that this discrepancy is for the potential energy; the deviation in the binding energy would be larger but is a misleading representation of the true error). The results in Table 3.2 are obtained with truncation at the partial waves shown.

There is a set of generally accepted approximations that have been made in the evaluation of the potential energy, related to the treatment of the center of mass momentum, and angular correlations between momenta. These will be discussed in Appendix I along with the details of how the results are obtained.

S	T	J	LL'	$\kappa^{JST}_{LL'}$ RSC	Paris
0	1	0	00	0.0242	0.0149
1	0	1	00	0.0336	0.0193
1	0	1	02	0.0959	0.0809
0	0	1	11	0.0042	0.0011
1	1	0	11	0.0021	0.0011
1	1	1	11	0.0046	0.0059
1	1	2	11	0.0025	0.0031
1	1	2	13	0.0029	0.0030
1	0	1	20	0.0000	0.0000
1	0	1	22	0.0000	0.0001
1	0	2	22	0.0003	0.0005
0	1	2	22	0.0001	0.0001
		κ		0.1704	0.130

Table 3.1 The contribution to the wound for different partial wave channels, evaluated for k_F=1.36 fm^{-1}. We see that the dominant wound contributions come from the $^1S_0$ and $^1S_1 - ^1D_1$ channels, with only minor contributions from higher partial waves.

		$U(k > k_F) = 0$	$U(k > k_F) \neq 0$
E_s	RSC	–11.2 MeV	–15. MeV
	Paris	–11.2	–15.
k_S	RSC	1.42 fm^{-1}	1.42 fm^{-1}
	Paris	1.51	1.51
κ	RSC	0.13	0.175
	Paris	0.11	0.14

Table 3.2 Saturation properties of the RSC and Paris potentials for two methods of calculating the single particle potential.

Chapter 4

Structure Function of Nuclear Matter

The structure function for nuclear matter can be written as the ground-state expectation value of an operator product. In Chapter 3 we saw that such an expectation value can be evaluated using Brueckner-Goldstone perturbation theory. Also, the physics of nuclear matter is much simpler and more easily analyzed than that of finite nuclei. Since for very heavy nuclei, high-momentum effects are expected to be independent of mass number[51], it would seem to be an ideal system for studying scaling in the large A nuclei. Indeed, we will see from the results of the NE3 experiment at SLAC[32] that the scaling function does indeed approach an asymptotic limit for large A.

We will first review what is known about the relationship between correlations and the momentum distribution for finite nuclei and nuclear matter. Then we will consider the problem of the uncertainties in the scaling function at large $|y|$. This is the region where the effects of correlations are dominant, and the contributions from the single-particle components have essentially vanished, so we will be sensitive to very small effects.

4.1 Momentum Distributions of Finite Nuclei

First, we will discuss what is known about the momentum distributions of finite nuclei. There has been a great deal of work on this subject, using both mean field approaches and two-body cluster-type expansions. The mean field approach suffers from the lack of short-range correlations in the wavefunction. Correlations can be modeled somewhat by multiplying the single-particle wavefunction by Jastrow functions [52], which mock up the short range behavior, but this method is somewhat arbitrary, and doesn't necessarily put the right physics into the problem. To demonstrate the problem with the mean-field theory, Fig. 4.1 shows the momentum distributions for ^{12}C, ^{56}Fe and ^{197}Au calculated using Hartree-Fock wavefunctions and the Skyrme III interaction[41]. The shaded area represents the approximate tail that exists in some of the more rigorous methods of calculation that we will now discuss. Obviously, the mean-field wavefunctions are missing orders of magnitude of strength in the tail.

There are equations for exact solutions (at the non-relativistic level) of the two- and three-body problems in quantum mechanics. Thus we can study ^{2}H, ^{3}H and ^{3}He. Let us start with the simplest, which is the deuteron. Here, if we write the wavefunction in coordinate space as

$$\psi(\boldsymbol{r}) = \psi_S(r)|^3S_1\rangle + \psi_D(r)|^3D_1\rangle \,, \tag{4.1}$$

then we can write $n(k)$ as

$$n(k) \propto |\phi_S(k)|^2 + |\phi_D(k)|^2 \,, \tag{4.2}$$

where the ϕ's are the Fourier transforms of the ψ's. We saw in Chapter 2 that the $F(y)$'s obtained from different potentials were in good agreement with the experimental results. This encourages us to believe that we can calculate the momentum distribution accurately for the deuteron. The next system that is obvious for study

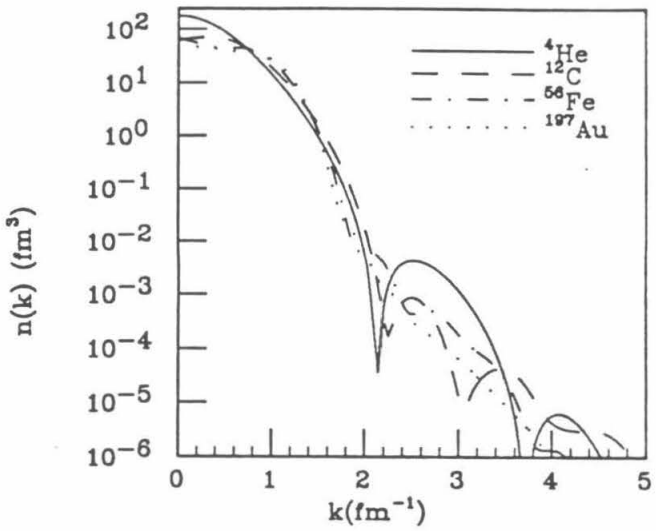

Figure 4.1 The momentum distributions of ^{12}C, ^{56}Fe and ^{197}Au from mean-field theory. The wavefunctions are from a Hartree-Fock calculation using the Skyrme III interaction.

is ^{3}He. Here, the Faddeev equations are an exact solution of the non-relativistic three-body system. From a practical point of view, this is not quite true. Calculations must, for storage reasons, be cut off at a finite number of partial waves, and cutoffs are common for the limits of integrals required in momentum space. All of these could affect the high-momentum components of $n(k)$. As seen, the theoretical $F(y)$'s do not agree at all with the data, even in the $Q^2 \rightarrow \infty$ limit (Sauer's results seem to come close, but the location of $y = 0$ in his calculation does not lie on top of the experimental point. Thus, his calculation needs to be shifted with respect to the data, at which point any glimpse of agreement goes away completely). Either there is another mechanism contributing to $F(y)$, or somehow, the calculations are suppressing high-momentum components. The latter is quite probable, since at the moment the Faddeev equations are used only for the bound state, and distorted waves are used for the continuum states.

What about systems with $A > 3$? There exist fairly good calculations in Brueck-

ner and exp(S) theory for light nuclei, up to ^{16}O. Van Orden, Truex and Banerjee have calculated $n(k)$ for ^{16}O using Brueckner theory[53], and their result is shown in Fig. 4.2. Zabolitzky and Ey have calculated $n(k)$ for ^{4}He and ^{16}O using the exp(S)

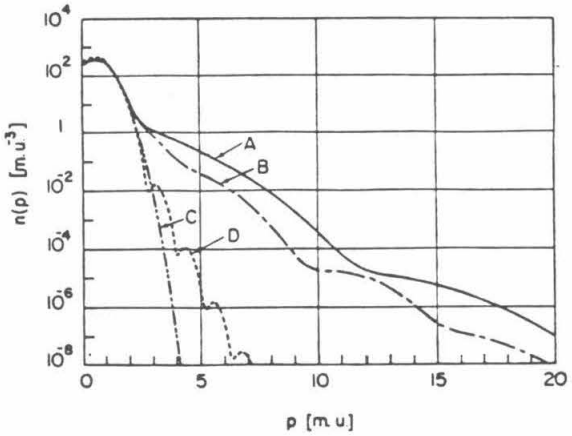

Figure 4.2 The momentum distribution of ^{16}O calculated by Van Orden *et al.* using Breuckner-Hartree-Fock on a harmonic oscillator basis. Curve C is the mean-field result; A and B are the full momentum distributions using RSC and the dTRS potential respectively. Curve D is the mean-field result using a Wood-Saxon potential. The units are given in "mesonic units," which are k (in fm^{-1})/ 0.7 fm^{-1} (from Ref. [53]).

coupled cluster method [54] (Brueckner theory is a subset of this method), along with various different potentials to study the sensitivity to short-range behavior in the potential (Fig. 4.3). The strong dependence of $n(k)$ on short-range behavior of the potential is quite evident from their results for the RSC potential[28], which has strong short-range Yukawa terms, and a strong tensor interaction, and the SSCB potential, which has a very soft core and a relatively weak tensor component. Except for nuclear matter, there exist no calculations for $A > 16$ of $n(k)$, which have a microscopic basis.

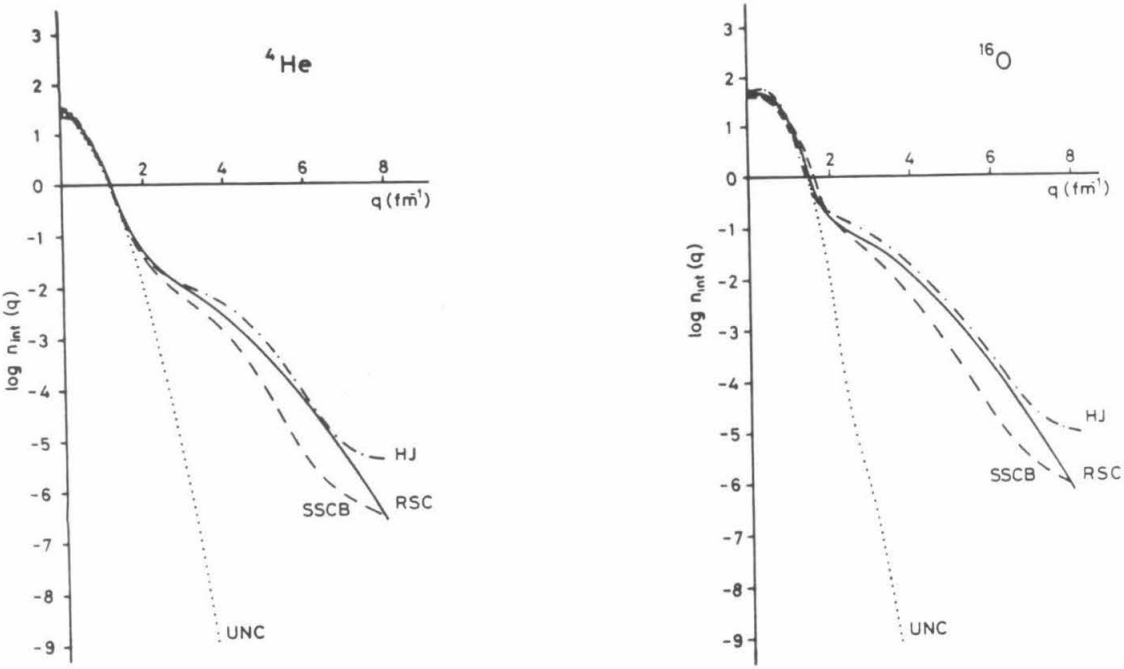

Figure 4.3 The momentum distributions of ^{4}He and ^{16}O calculated by Zabolitzky and Ey using the exp(S) method. Note the fairly strong dependence in the tail on the potential used. UNC is the result from the single particle basis used, SSCB is the dTRS potential, RSC is the Reid Soft Core potential, and HJ is the Hamada Johnston potential (from Ref. [54]).

4.2 Momentum Distribution of Nuclear Matter

The momentum distribution for nuclear matter interacting only through a mean field is trivial, given by a step function cutting of at k_F. Knowing this, we can immediately evaluate its magnitude via the normalization condition

$$\int \frac{d\boldsymbol{k}}{(2\pi)^3} n(k) = 1 \,. \tag{4.3}$$

For $n_0(k) = C\Theta(k_F - k)$, we find that $C = 6\pi^2 k_F^{-3}$. Using Brueckner theory, we should be able to calculate the momentum distribution of a fully interacting system. This is done by evaluating the ground-state expectation value of the operator $a_{\boldsymbol{k}}^\dagger a_{\boldsymbol{k}}$. This is the number operator for the density of particles at momentum $\boldsymbol{k}$. The Brueckner-Goldstone expansion is given in Fig. 4.4. The first graph is the

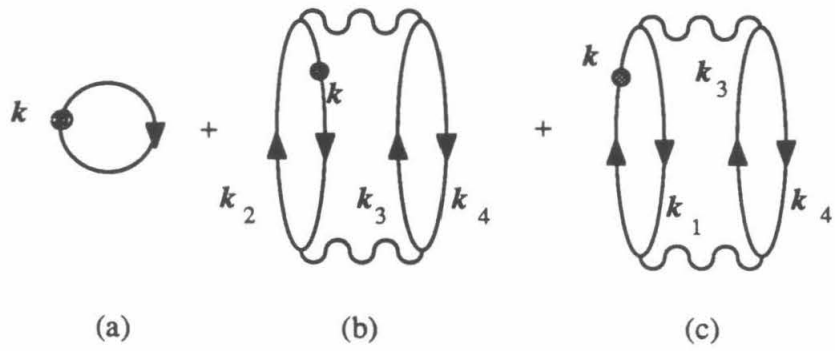

Figure 4.4 Brueckner-Goldstone expansion for the momentum distribution of nuclear matter through two-hole-lines.

unperturbed mean-field result, and the second is the depletion due to two-particle two-hole excitations out of the Fermi sea. The second graph is closely related to the wound integral of Brueckner many-body theory. The third graph gives the distribution of particles excited out of the sea. This is the most interesting component of the distribution, in that it is the part most easily studied in detail. The very high-momentum components of this graph will tell us about the short-range parts of the interaction we want to study.

The analytic structures of the graphs are quite simple. The first graph is given above (the mean-field result). The second and third have very similar forms

$$n_b(k) = -\frac{(2\pi)^3}{4\rho}\int d\boldsymbol{k}_2 d\boldsymbol{k}_3 d\boldsymbol{k}_4 \frac{|\langle \boldsymbol{k},\boldsymbol{k}_3|G|\boldsymbol{k}_2,\boldsymbol{k}_4\rangle|^2}{(e(\boldsymbol{k})+e(\boldsymbol{k}_3)-e(\boldsymbol{k}_2)-e(\boldsymbol{k}_4))^2} \times\Theta(k_F-k)\Theta(k_F-k_3)\Theta(k_2-k_F)\Theta(k_4-k_F) \quad (4.4)$$

$$n_c(k) = \frac{(2\pi^3)}{4\rho}\int d\boldsymbol{k}_1 d\boldsymbol{k}_3 d\boldsymbol{k}_4 \frac{|\langle \boldsymbol{k}_1,\boldsymbol{k}_3|G|\boldsymbol{k},\boldsymbol{k}_4\rangle|^2}{(e(\boldsymbol{k}_1)+e(\boldsymbol{k}_3)-e(\boldsymbol{k})-e(\boldsymbol{k}_4))^2} \times\Theta(k_F-k_1)\Theta(k_F-k_3)\Theta(k-k_F)\Theta(k_4-k_F)\,. \quad (4.5)$$

This expansion should preserve the normalization of $n(k)$ exactly. It is a strong test of the numerical techniques to meet this condition (the factor of $(2\pi)^3$ is present to make the normalization as given in Eq. 4.3).

Fig. 4.5 shows the momentum distributions obtained by us for the RSC[28] and Paris[55] potentials using Brueckner techniques. They are almost identical to the distribution of Fantoni and Pandharipande [56] obtained using the Argonne v14 potential and the coupled-cluster technique[57]. On the log scale, the effect of correlations for $k < k_F$ is not noticeable, and on a linear scale (Fig. 4.6) they are only marginal (about 10%). This corresponds to what we know about the wound integral, which is essentially the average deviation of the correlated and free distributions out to k_F (within a constant).

At this point we can take our momentum distribution and calculate a scaling function ($F(y)$) using the IA for nuclear matter (Fig. 4.7). The plateau around $y = 0$ is essentially the result for the free Fermi gas, and the tail is the result of correlations.

We should try to determine what physical properties the tail of the distribution is most sensitive to. This will be important when we try to make comparisons to experiment. One immediate point is that we do not do our calculation at the saturation density, and we might wonder what effect this can have on the strength of the tail. It is fairly simple to compare the momentum distributions for different

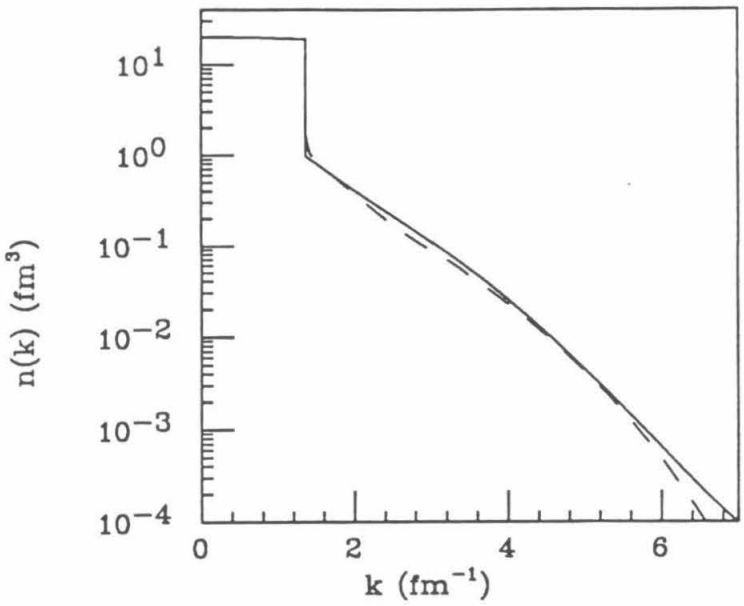

Figure 4.5 The momentum distribution of nuclear matter calculated at k_F=1.36 fm^{-1}, using the expansion of Fig. 4.4. Curves shown are for the RSC (solid) and Paris (dashed) potentials.

values of k_F. As we can see in Fig. 4.8, the sole major effect is to redistribute the strength in the peak; the correlation tail is fairly stable against change out to about 1.2 GeV/c. Another factor that influences the strength of the momentum distribution in the region of interest is the tensor interaction between nucleons. More specifically, the tensor interaction in the $^3S_1 - ^3D_1$ channel. Fig. 4.9 shows the consequences of removing the effects of the tensor force in nuclear matter. We do this by removing all G-matrix contributions of the form G_{LL+2} and G_{L+2L}. In each case, the removal of tensor effects can deplete the strength by an order of magnitude in the range 1.5 fm$^{-1} < k <$ 4 fm^{-1}.

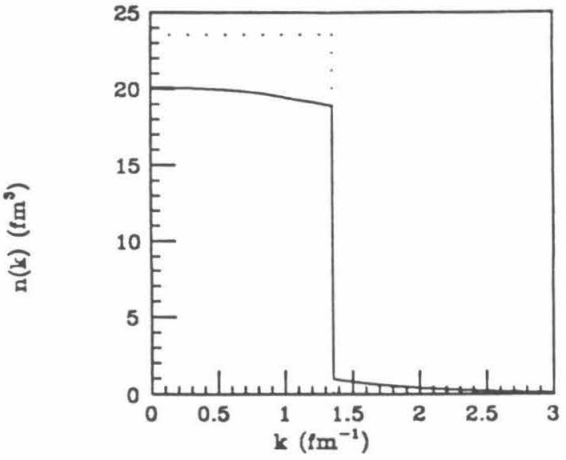

Figure 4.6 Same as Fig. 4.5, except shown on linear scale to show the depletion for $k < k_F$. The dotted line is the free Fermi gas, and the solid line is for the RSC potential.

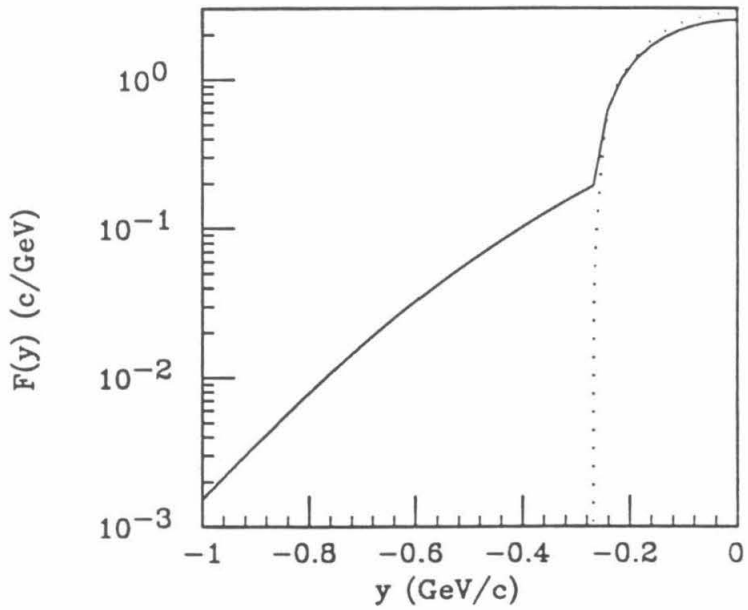

Figure 4.7 $F(y)$ as calculated using the RSC momentum distribution of Fig. 4.5. The dotted curve is the free Fermi gas result.

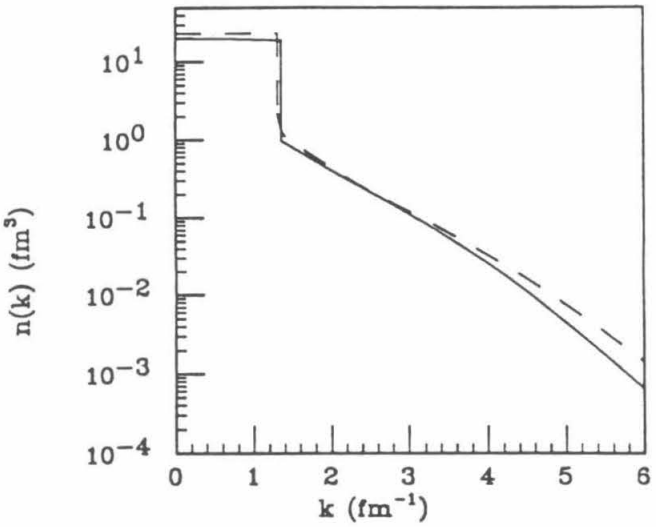

Figure 4.8 Effect of k_F on the momentum distribution of nuclear matter. The distributions are calculated using the RSC potential. The solid curve is the distribution at k_F=1.36 fm^{-1} and the dashed curve at k_F=1.31 fm^{-1}.

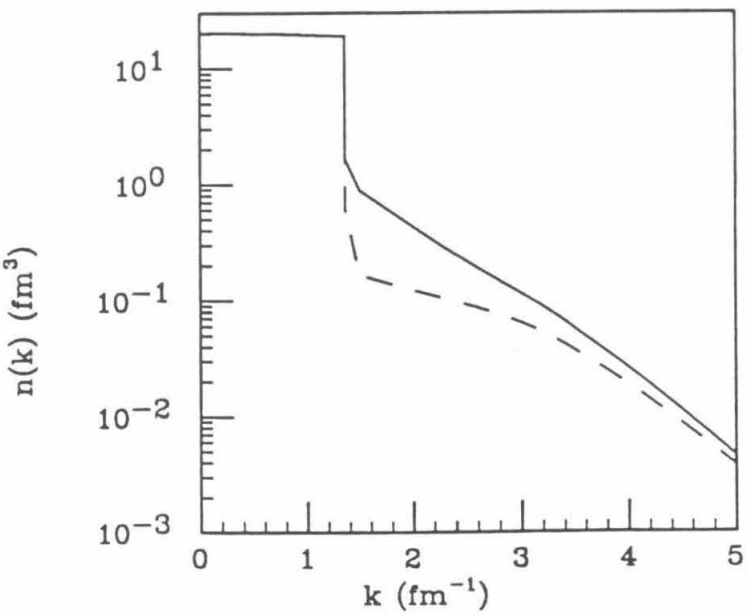

Figure 4.9 The contribution of tensor terms to the momentum distribution for nuclear matter. The full curve is $n(k)$ from Fig. 4.5, and the dashed curve is the distribution with all tensor terms removed (see text).

4.3 Many-Body Effects on the Structure Function

One question that must be asked when considering the relation between inclusive quasielastic electron scattering and the momentum distribution of the target is: Are there final-state or other strong correlation effects in the scattering reaction that destroy the simple relation given by the IA? The evaluation of final-state effects in an inclusive reaction is a difficult problem. Weinstein and Negele[58] and Weinstein[59] have discussed one possible approach, and applied it to the problem of an infinite Bose systems interacting via a hard-core potential. Their approach was to expand the structure factor $S(q,\omega)$ of Eqn. 2.13 using Brueckner-Goldstone perturbation theory. As we saw in Chapter 3, this is straightforward whenever a ground-state expectation value is involved. They found significant contributions from diagrams that contain an interaction between the two density operators. These play the role of final-state interaction contributions. We use their method to study the structure function for the more "physical" system of nuclear matter.

The complete expansion for $S(q,\omega)$ up to two-hole-lines is given in Fig. 4.10 (exchange graphs are calculated, but not shown here). There are some minor differences now between our diagrams and those of Weinstein and Negele. We consider the full single-particle potential above and below the Fermi surface, so one-loop graphs such as diagram (f) in Fig. 4.10 can contribute only through their imaginary components.

Here we can see the true many-body components of the structure function. The Diagrams (A,E,F,G and H) correspond to contributions due to the momentum distribution for $k < k_F$ (this is shown in Ref. [59]). Diagram (a) corresponds to the contribution of the momentum distribution for $k > k_F$, while diagram (b) represents the two-body correlation term in IA for particles above the Fermi sea. Diagrams in which an interaction takes place between the injection and removal of

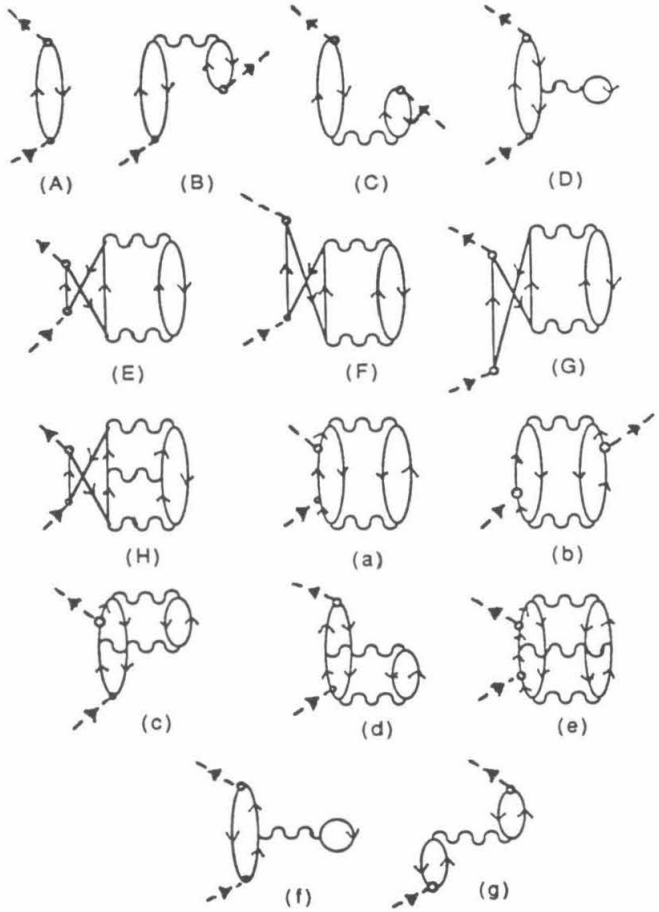

Figure 4.10 Goldstone diagrams for the expansion of $S(q,\omega)$ up to two-hole-lines. Wiggly lines represent G-matrix elements, and the dashed lines transport momentum and energy (q and ω) through the graphs.

energy and momentum correspond to final-state interaction effects (unfortunately, working in the framework of Compton amplitudes does not allow direct conversion back to scattering matrix elements). We can see that final-state interactions take place on a microscopic level with real two-body interactions between the struck nucleon and the spectator system This is much more fundamental than an optical model approach, which is a relatively simple mean-field approximation. As we have seen with the momentum distribution, we are studying a kinematic regime where mean-field approximations are simply not reliable.

A key component of the results of Weinstein and Negele's calculation is the

behavior of the off-shell matrix elements at high-momentum transfer. For Q^2 very large, the off-shell elements can be approximated as $\langle \boldsymbol{q}|\mathcal{G}(\omega+i\eta)|\boldsymbol{q}\rangle$. This in turn is equivalent to $\langle \boldsymbol{q}|T(\omega+i\eta)|\boldsymbol{q}\rangle$, where T is the free scattering matrix element defined in Chapter 2. If the scattering is purely due to a hard-core, then this matrix element is proportional to $|\boldsymbol{q}|$ to leading order. This is a simple consequence of the optical theorem, which states

$$\mathrm{Im}\langle \boldsymbol{q}|T|\boldsymbol{q}\rangle = -\frac{\hbar^2}{M}|\boldsymbol{q}|\sigma_T\,, \tag{4.6}$$

where σ_T is the total cross section. For the hard sphere, σ_T is a constant equal to $2\pi a^2$, where a is the radius of the sphere. Weinstein tabulated the q-dependence of each diagram, and his results are shown in Table 4.1. The final-state-interaction

Diagram	Leading q-behavior
a	q^{-1}
b	q^{-4}
c	q^{-1}
d	q^{-1}
e	q^{-1}
f	q^{-1}
g	q^{-1}

Table 4.1 The q dependence of the diagrams in Fig. 4.10 for an infinite hard-core potential (from Ref. [59])

graphs that contain imaginary components of matrix elements are all $\mathcal{O}(1/q)$ to first order. This is the same dependence as shown by the direct IA graph. It is thus possible for there to be finite corrections to IA even at $Q^2 \to \infty$. This is, in fact, the case, as can be seen in Fig. 4.11 This is, of course, *strongly* dependent on the behavior of the T-matrix elements at high Q^2 resulting from the hard core. With a softer core, σ_T will decrease with q, and this would result in the final-state effects vanishing in the asymptotic limit.

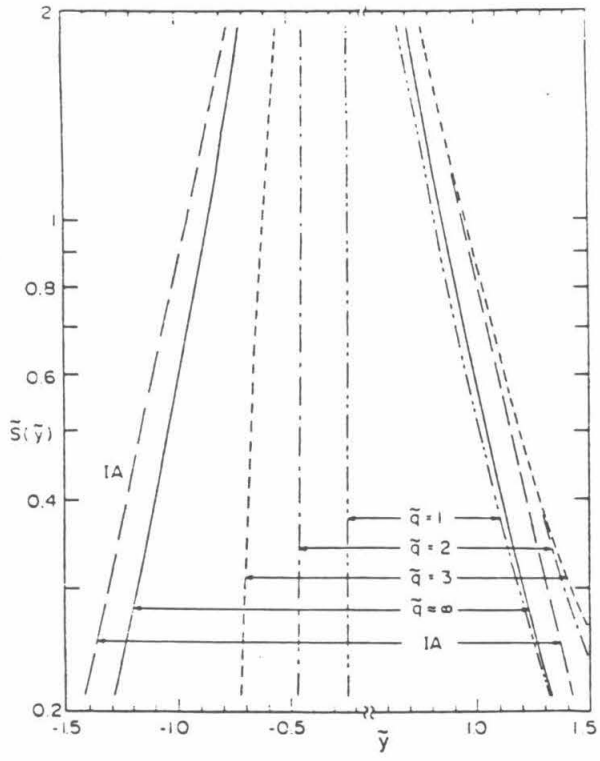

Figure 4.11 The results of Weinstein and Negele for the structure function of a Bose gas interacting with a hard-core potential. Results are given in a dimensionless form, with the radius of the hard core (a) setting the scale (from Ref. [58]).

4.4 Discussion of Results

We discuss the detailed algebraic expansions of the diagrams of Fig. 4.10 in Appendix II, and use the partial wave technology discussed in Appendix I. The integrals over angular coordinates are done using Gauss-Legendre quadrature. Third order was found sufficient for good convergence of the integrals. The "radial" k integrations are performed using Simpson's rule with a grid spacing of $k_F/10$. The effects of halving the grid spacing are on the order of 0.5% or less, consistent with the findings of Haftel and Tabakin[60]. In diagram (e), it is neccesary to perform principal value integrals in kinematic regions where the energy denominator can be zero. The method discussed in Appendix I is used to remove the singularities in the integral. For our definition of y, we choose a non-relativistic reduction of Eqn. 2.29. This is necessary because of the non-relativistic nature of our calculation, and the implications of this will be discussed later in this section. For nuclear matter (no recoil energy), this leaves us with

$$\omega + \bar{\epsilon} = \frac{(q+y)^2}{2M} \tag{4.7}$$

which in turn yields

$$y = -q + \sqrt{2M(\omega + \bar{\epsilon})}\,. \tag{4.8}$$

We use $\bar{\epsilon} = -51$ MeV, which is the mean single-particle energy for nuclear matter at $k_F = 1.36$ fm^{-1}.

Following the lead of Eqn. 2.23 in Section 2.4, we define a function

$$\mathcal{F}(q,y) = \frac{q}{M} S(q,\omega) \tag{4.9}$$

where we now allow for the fact that there might not be perfect scaling at finite Q^2. In the IA, $\mathcal{F}$ quickly approaches $F(y)$, but we are interested in studying any deviation that might occur from the IA because of the effects of final-state interactions. Our calculations are performed at four sets of kinematic parameters. These are

chosen to match up with part of the NE3 data sets, so that we might later compare our answers to the experimental results. The kinematics we study result from an incident electron beam energy of 3.6 GeV, and scattering angles of 16°, 20°, 25° and 30° (these are only a subset of the NE3 kinematics, which examine many other angle and energy combinations). Since we are actually interested in the Q^2 dependence of the approach to scaling, these kinematic sets will be examined in terms of the Q^2, which correspond to the appropriate scattering angle and energy transfer. The range of Q^2 that we study is then approximately $0.8(\mathrm{GeV/c})^2 < Q^2 < 2.6(\mathrm{GeV/c})^2$. Results are obtained for both the RSC[28] and Paris[55] potentials, although both turn out to be virtually identical, and thus they will discussed as a unit. Lastly, we only consider the region $y < -k_F$. For $|y| < k_F$, mean-field effects dominate and we cannot really study the effects of correlations in any detail (Sec. 4.1). However, for $|y| > k_F$, all the structure we see is the result of two-body correlations, so we are very sensitive to their effects in the initial and final states.

Fig. 4.12 compares results for IA and the full calculation for the range of Q^2 considered. Note the marked difference in behavior of the two with respect to Q^2, and also the sharp kinematic cutoffs. The latter is due to the the matching condition where the upper and lower integration limits become equal. In the Brueckner approach, the cutoff point is the minimum energy transfer for exciting two particle-hole pairs. This, however, does not correspond to the zero energy transfer point of the true scattering process and we will discuss that problem later. We now would like to see how well our calculation fares when compared to the data. Unfortunately, the data do not exist at nice, uniform values of y, and the values change for each Q^2. Thus, we must interpolate the data to the values of y that we study. Fig. 4.13 shows the experimental data and the interpolated results for ^{56}Fe. It is immediately clear that the interpolation is a reasonable procedure, given that the data lie on relatively smooth curves. The error bars are chosen to be representative of both the statistical

uncertainties of the data, and of the uncertainty of the interpolated values. Using these interpolated points we can now compare our results to the data. This is done for ^{56}Fe (Fig. 4.14) and ^{197}Au (Fig. 4.15). We can see that the trend is now correct for the approach to scaling. However, there are two very obvious problems, the most obvious being the normalization. The theoretical results are factors of 3–5 too large. What is the cause of this discrepancy? For the moment, let us assume that the problem lies in the potential. Indeed, such strong dependences can be seen in other calculations, such as that of Frankfurt and Strickman [35] for ωW_2 of the deuteron (Fig. 4.16). Using RSC vs. the Hamada-Johnston potential (the correct version) [61,62] caused an order of magnitude difference in the results, again showing the sensitivity of the momentum distribution to the short-range properties of the potential (as discussed in Sec. 4.2). We can attempt to remove the detailed dependence on the exact nature of the potential by normalizing the results and the data, so that the asymptotic result of each is unity. This entails taking the ratio

$$\frac{\mathcal{F}_D(q,y)}{\mathcal{F}_D(q_{\max},y)}, \tag{4.10}$$

with D representing the data, IA and the full calculation. $q_{\max}$ represents the maximum q studied for each y. The theory certainly seems to indicate that the asymptotic limit is effectively reached at the highest Q^2. However, we do not know this for sure with respect to the data. We will discuss this point later. In Fig. 4.17 we see the effects of "renormalizing" the results for ^{56}Fe (the experimental data for ^{197}Au does not extend to high enough Q^2 to determine an asymptotic limit, so we do not examine it here). The agreement is now much better, but now we need to turn our attention to the problem of the cutoffs.

The dominant diagrams can easily be written as the integral of some function $F(\boldsymbol{k})$ over all $\boldsymbol{k}$, constrained by a delta function forcing energy conservation. As discussed earlier, energy conservation in Brueckner-Goldstone theory takes the two-

body form resulting from two-particle-two-hole excitations. It thus takes the form

$$\omega + 2\bar{e} = e(\boldsymbol{k}) + e(2\boldsymbol{P} - \boldsymbol{k}) \tag{4.11}$$

(here we have replaced the exact hole energies with an average hole energy $\bar{e}$). If we recall the expression in Chapter 2 for the scaling function using IA, the algebraic structure was the same, except for the fact that the energy conservation took on the one-body form

$$\omega + \bar{\epsilon} = e(\boldsymbol{k}) \tag{4.12}$$

(the equivalent energy denominator would be for one particle-hole pair). Here, $\bar{e}$ and $\bar{\epsilon}$ play identical roles, as the average separation energy of a nucleon in nuclear matter (which is essentially the same as the average hole energy). We propose to make an arbitrary replacement of the two-body form with the one-body form. It must again be stressed that this is *not* rigorous within the strict format of the perturbation expansion, but there is a better phenomenological connection with the real scattering process, as now we can study the scaling function right down to the zero-energy transfer region. We now compare our results again to experiment and can see the same problems as before with the unnormalized results (Figs. 4.18 and 4.19), but there is much more reasonable agreement using the renormalized results (Fig. 4.20).

We should now address the question of whether the data has indeed reached an asymptotic limit. There has been a supplemental run of NE3 of ^{56}Fe (NE3′), which took data at higher Q^2 for large negative y . The kinematics of the run come from an initial beam energy of 4 GeV, and a scattering angle of 30°. This data recently became available to us[63], and in Fig. 4.21 we can see that the data do seem to approach a scaling limit, and if we reanalyze the approach to scaling (Fig. 4.22), the agreement is slightly better than before.

Given the apparent qualitative agreement between theory and experiment, we can study the contribution of each diagram to the approach to scaling. In Fig. 4.23,

we examine the approach to scaling diagram by diagram for $y = -0.5$ GeV/c (the results for other values of y are qualitatively the same). It is immediately clear that the only significant contributions come from the IA graph, and from diagrams (c) and (d). Diagram (e) is of slight importance, but plays no real role in the approach to scaling. Diagram (b) is extremely small, as anticipated in the discussion in Section 2.4.

Another question that should be addressed is the validity of using the non-relativistic equation relating ω, q and y. We compare the relativistic ($y_{\rm r}$) and non-relativistic ($y_{\rm nr}$) definitions for two kinematic sets in Table 4.2. The definitions valid for a finite target of A nucleons are

$$y_{\rm nr} = \left(\frac{A-1}{A}\right)\left(-q + \sqrt{2M(\omega+\bar{\epsilon}) - \frac{q^2}{A-1}}\right) \tag{4.13}$$

$$y_{\rm r} = \frac{-\left(q - \frac{qC}{2B^2}\right) + \sqrt{\left(q - \frac{qC}{2B^2}\right)^2 - \left(1 - \frac{q^2}{B^2}\right)\left(q^2 + m^2 - \frac{C^2}{4B^2}\right)}}{\left(1 - \frac{q^2}{B^2}\right)} \tag{4.14}$$

with

$$B = \omega + AM + \bar{\epsilon} \text{ and } C = q^2 + M^2 + B^2 - (A-1)^2M^2 .$$

In the limit of infinite A, these go over to

$$y_{\rm nr} = -q + \sqrt{2M(\omega+\bar{\epsilon})} \tag{4.15}$$

$$y_{\rm r} = -q + \sqrt{2M(\omega+\bar{\epsilon}) + (\omega+\bar{\epsilon})^2} . \tag{4.16}$$

The comparison is done for both nuclear matter and ^{56}Fe, so that we can see the effects of recoil. The value used for $\bar{\epsilon}$ is -51 MeV, obtained from the nuclear matter results at $k_F = 1.36$ fm^{-1}. This will tell us how well nuclear matter approximates the finite system in a kinematic sense.

We can see that for low Q^2, the non-relativistic definition works quite well, At high Q^2, the non-relativistic definition of y compares quite poorly to the relativistic

ω (GeV)	Q^2 ((GeV/c)^2)	NM		^{56}Fe	
		y_{nr}	y_r	y_{nr}	y_r
		θ=16°			
0.10	0.976	-0.687	-0.683	-0.705	-0.685
0.15	0.962	-0.559	-0.548	-0.570	-0.540
0.20	0.948	-0.463	-0.443	-0.472	-0.430
0.25	0.934	-0.386	-0.354	-0.394	-0.338
0.30	0.920	-0.320	-0.276	-0.328	-0.258
		θ=25°			
0.10	2.36	-1.233	-1.229	-1.291	-1.269
0.25	2.26	-0.911	-0.879	-0.930	-0.874
0.40	2.16	-0.712	-0.640	-0.725	-0.624
0.55	2.06	-0.567	-0.446	-0.579	-0.424
0.70	1.96	-0.460	-0.282	-0.471	-0.257

Table 4.2 The effects of recoil (in the case of ^{56}Fe) and of relativity on the relation between y and ω.

one. This is actually not a problem because at high Q^2, our results are dominated by IA. Here, the scaling function is exactly the same whether the derivation is relativistic or non-relativistic (as long as the energy conserving delta function is kept covariant). It is only where the final-state effects are important that we need worry about the exact kinematic relationship between ω and y. At low Q^2, there is reasonable agreement between the relativistic and non-relativistic definitions of y (within a few percent).

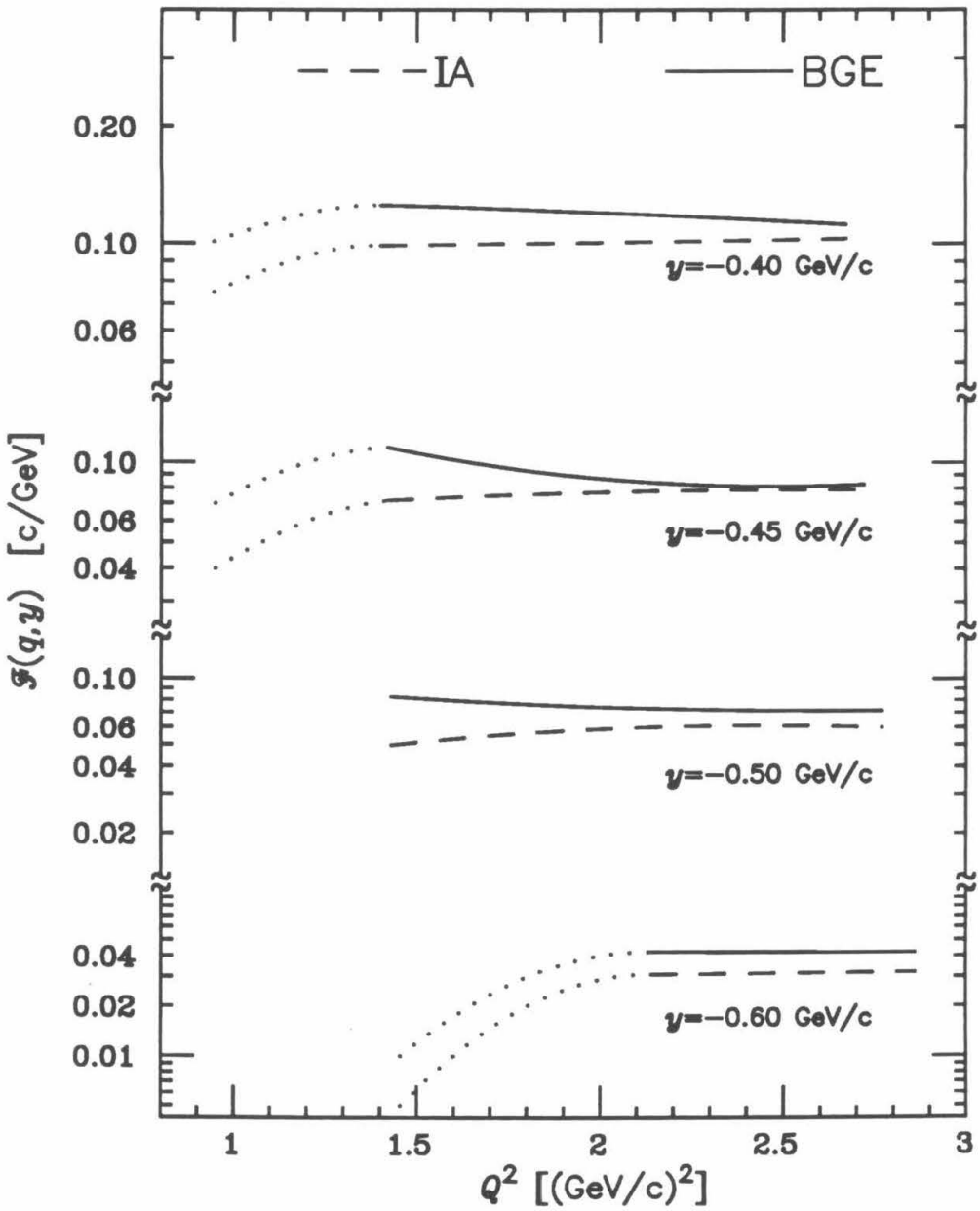

Figure 4.12 Results for the extraction of $\mathcal{F}(q, y)$ from the full Breuckner-Goldstone calculation (BGE), and the Impulse Approximation (IA). The approach to scaling is shown at various representative values of y which are in the correlation tail. The results for the RSC and Paris results are virtually identical, so they are only shown as one curve. The dotted extensions to lines represent points very near the kinematic cutoff, and should not be compared seriously with the data.

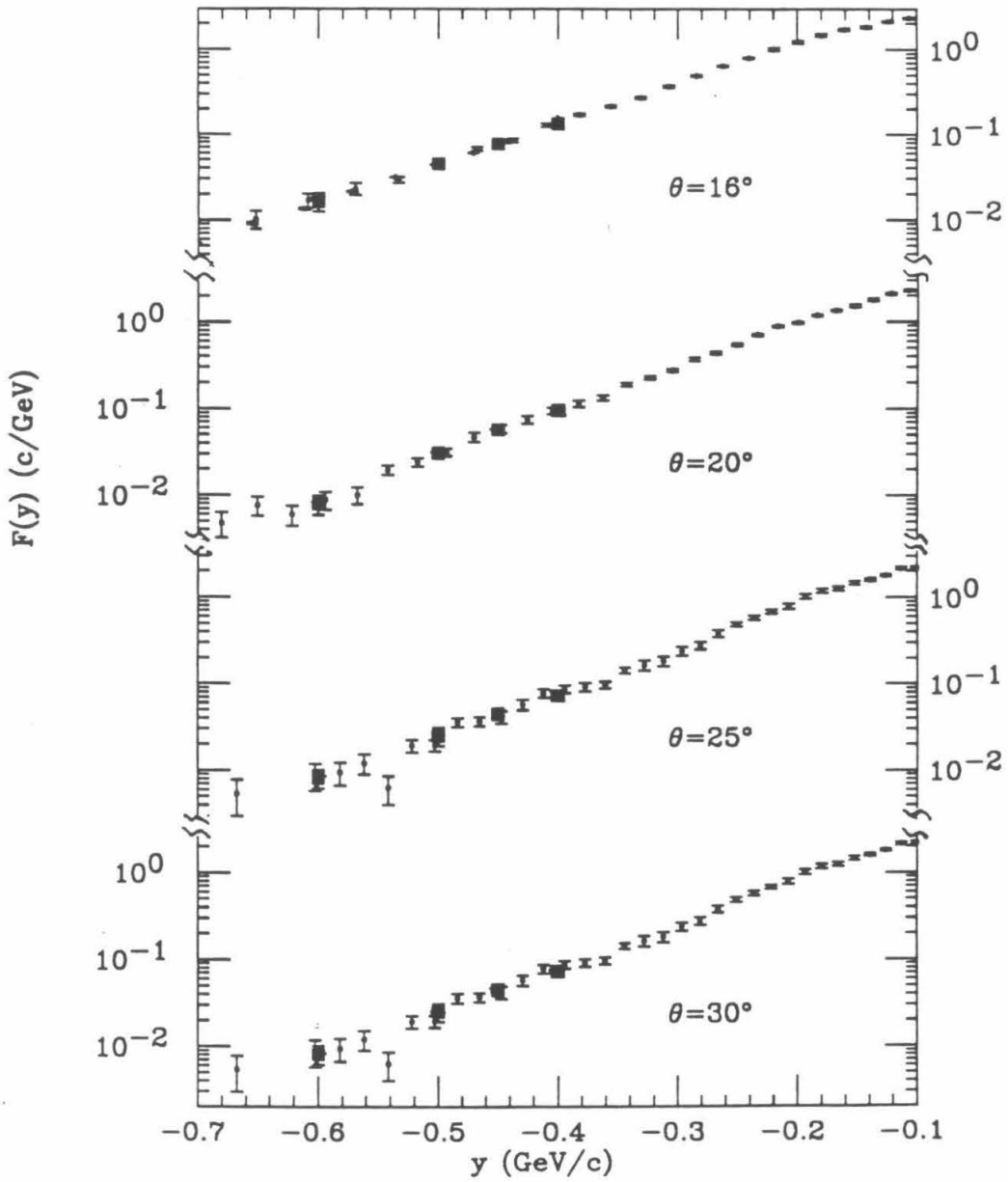

Figure 4.13 Interpolated data sets for ^{56}Fe. The interpolated values are marked by boxes (data from Ref. [32]).

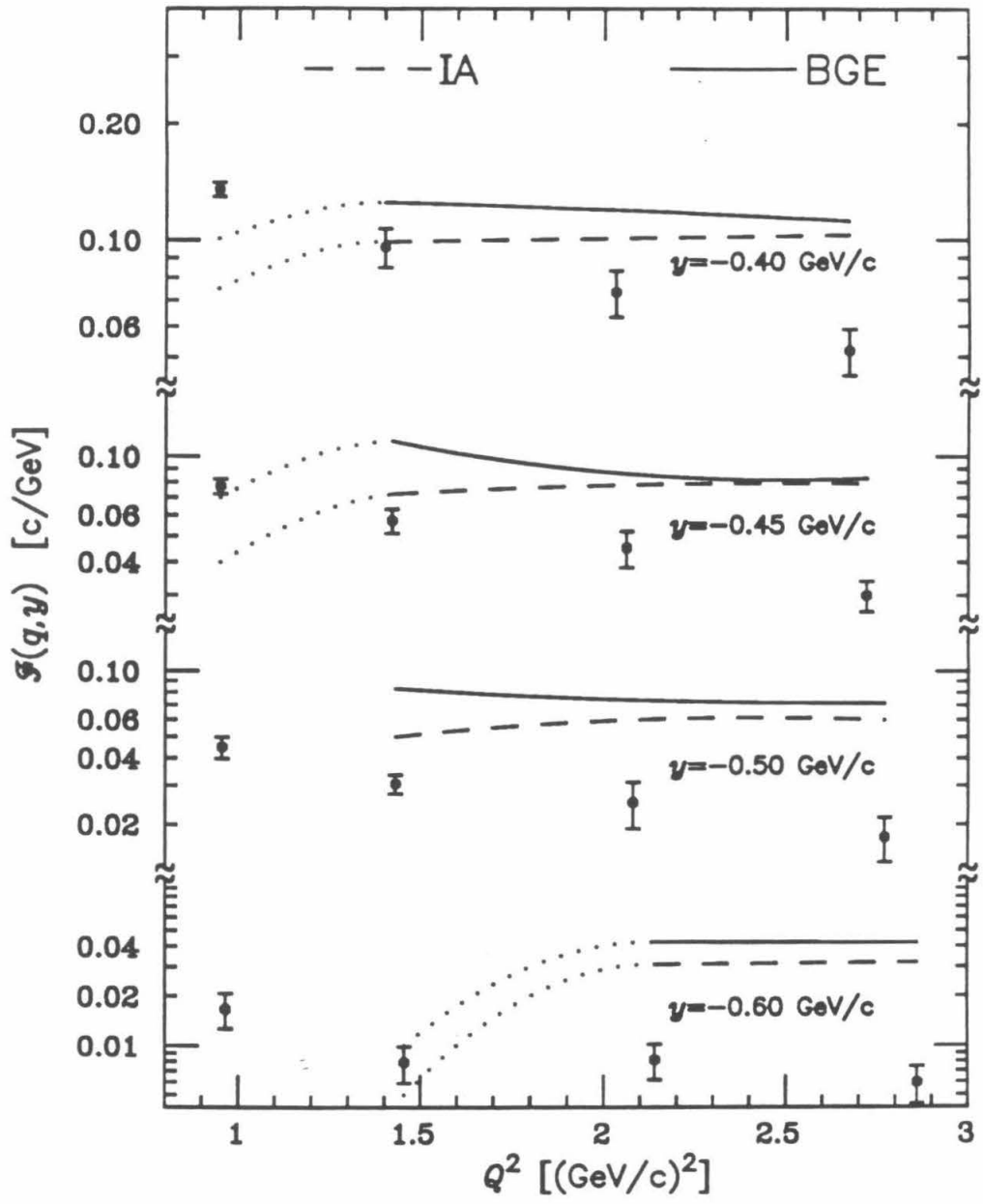

Figure 4.14 Comparison of the results of Fig. 4.12 with the (interpolated) NE3 data for ^{56}Fe[32]. Notice that the theoretical calculation is very restricted in kinematics compared to the experimental results.

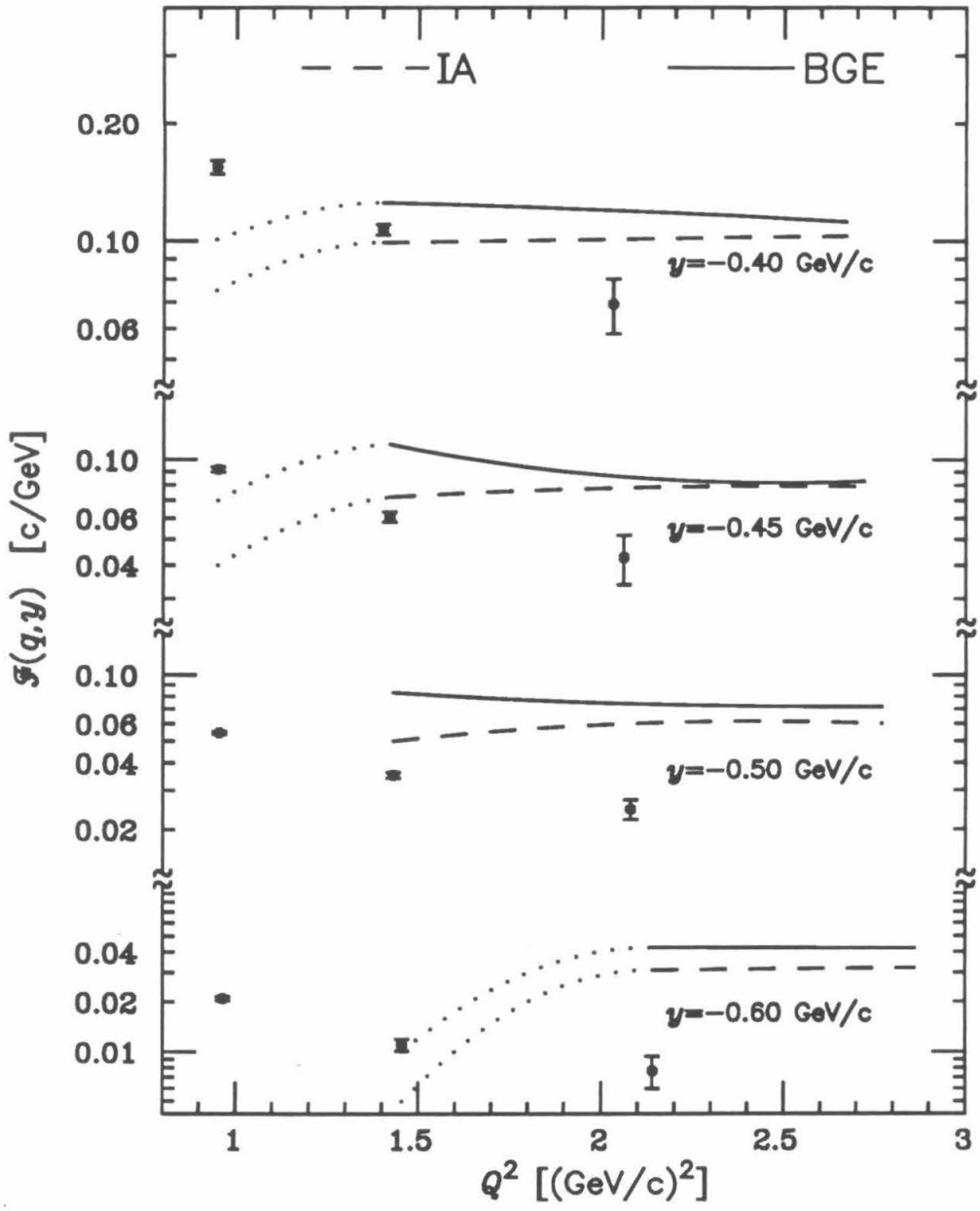

Figure 4.15 Same as Fig. 4.14, but now compared to the NE3 data for ^{197}Au.

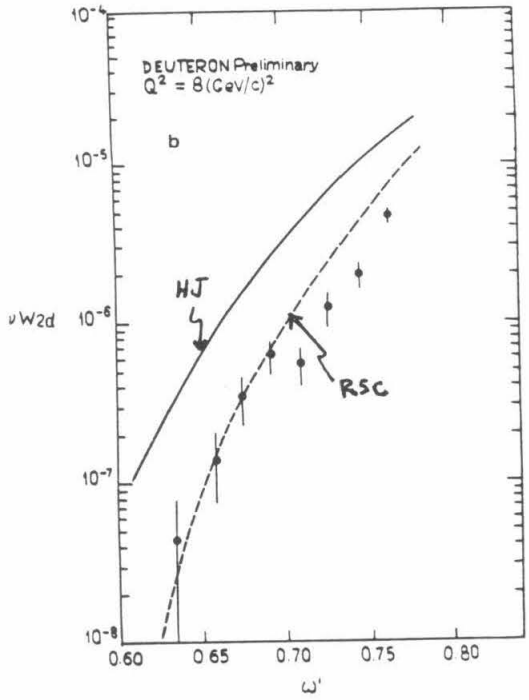

Figure 4.16 The structure function ωW_2 plotted against ω' ($\omega' = (2M^2 + 2M\omega)/Q^2$). Note that the theoretical results can vary by an order of magnitude depending on the potential model used. Both potentials do a reasonable job on static observables (from Ref. [35]).

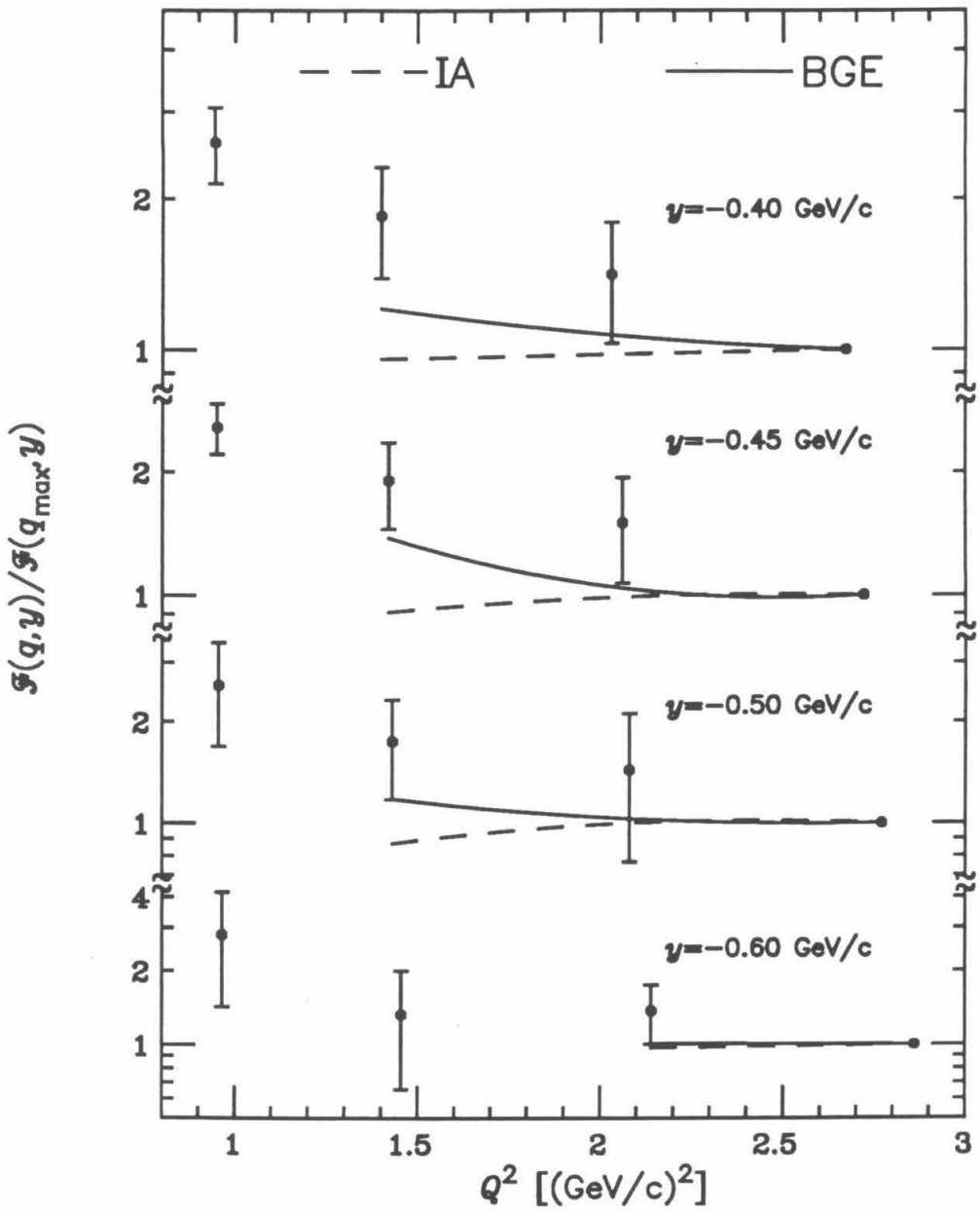

Figure 4.17 The approach to scaling of the results shown in Fig. 4.12 plotted against the approach to scaling of the NE3 data for ^{56}Fe. Only theoretical points away from the cutoffs are shown

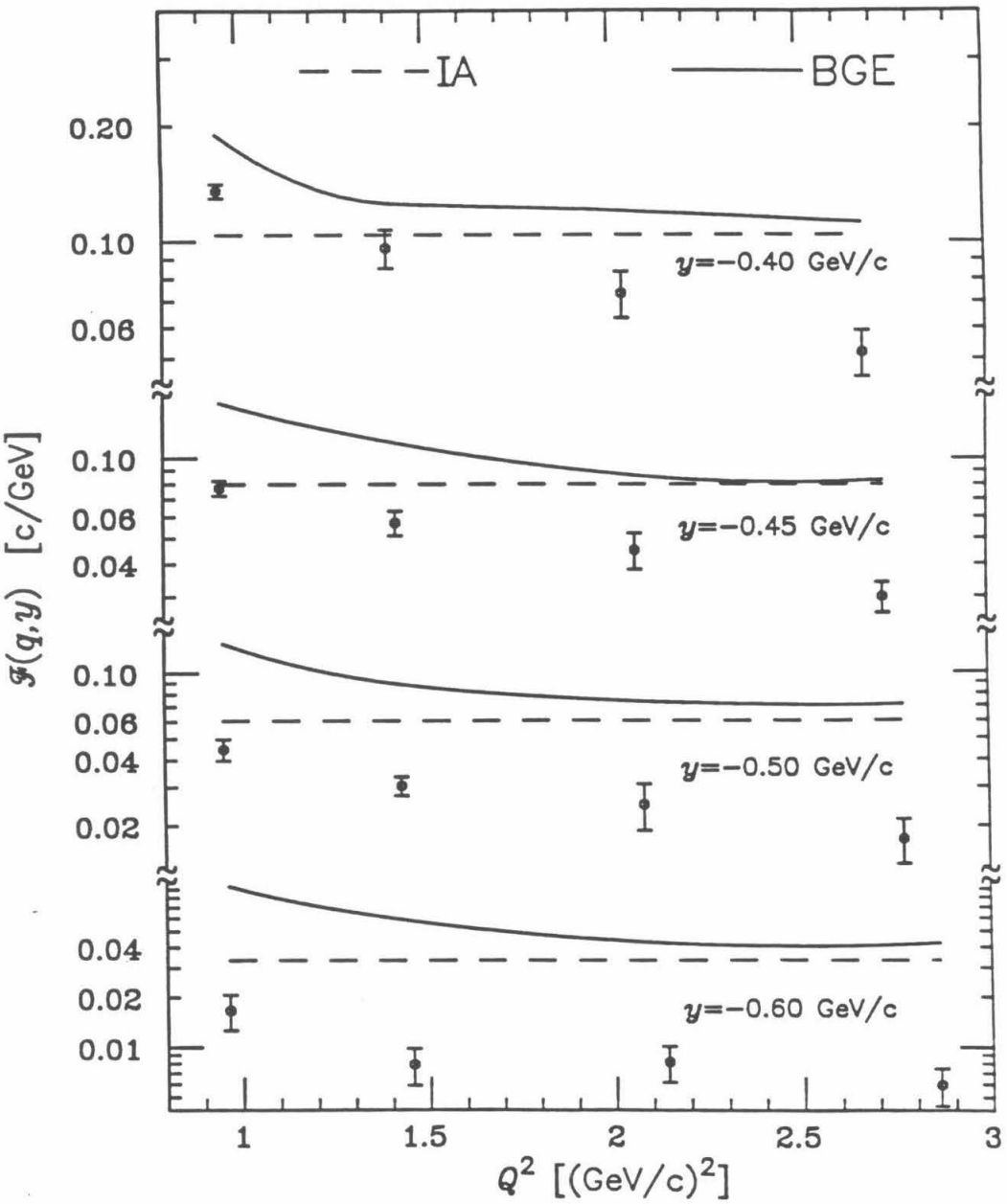

Figure 4.18 Same as Fig. 4.14 except that the one-body form for the energy conservation is used in the theoretical results.

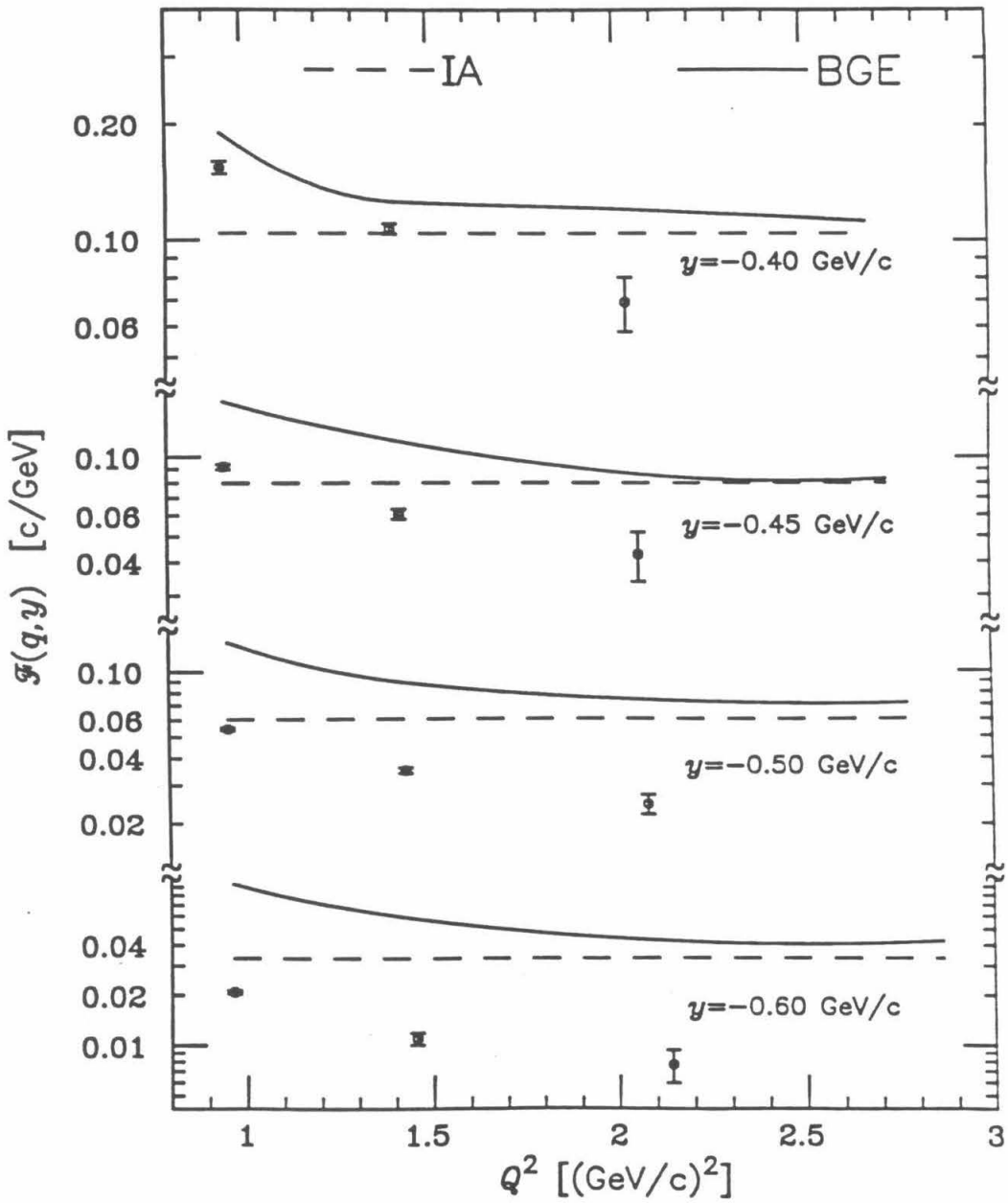

Figure 4.19 Same as Fig. 4.15 except that the one-body form for the energy conservation is used in the theoretical results.

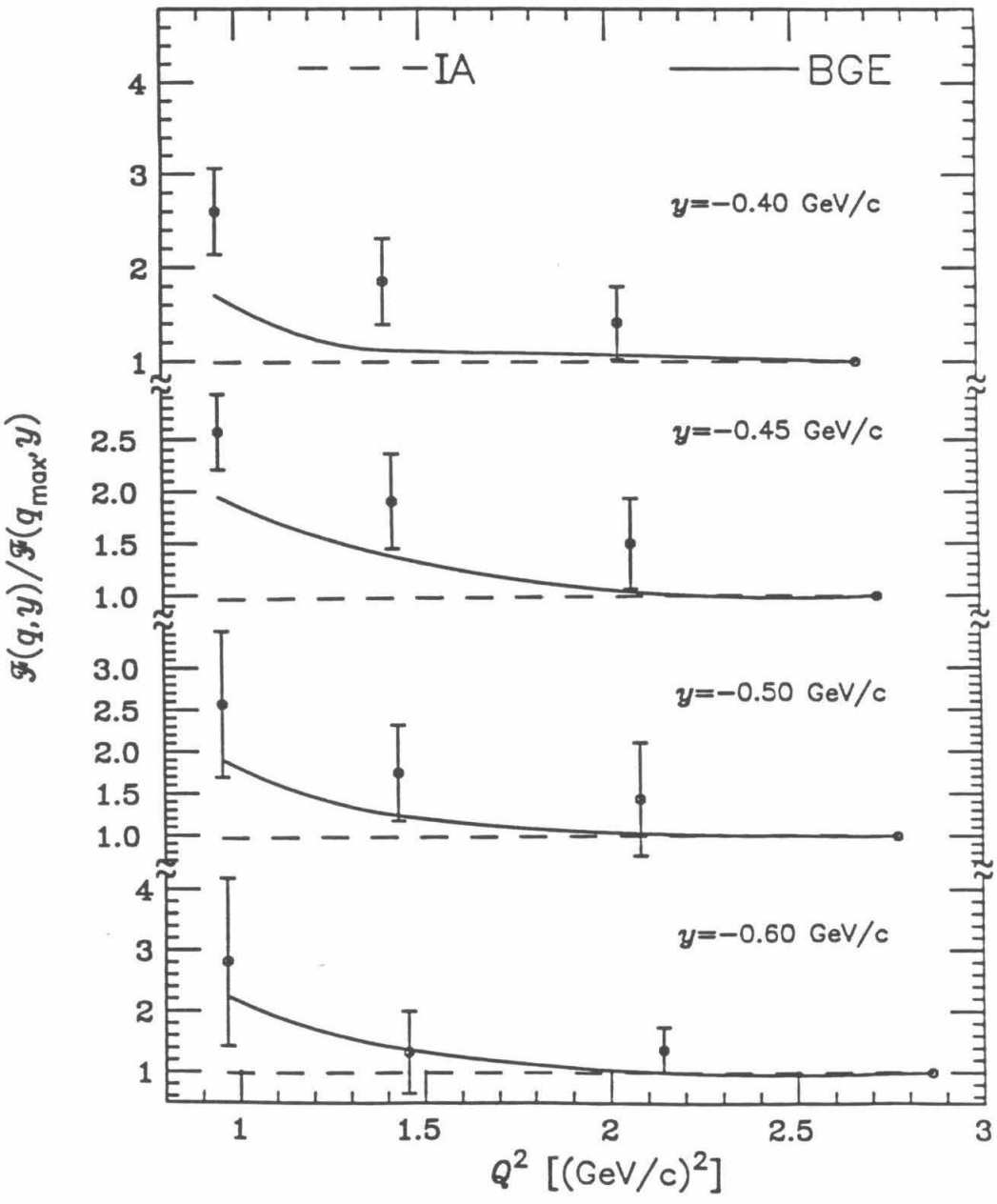

Figure 4.20 Same as Fig. 4.17 except that the calculations use the one-body form for the energy conservation.

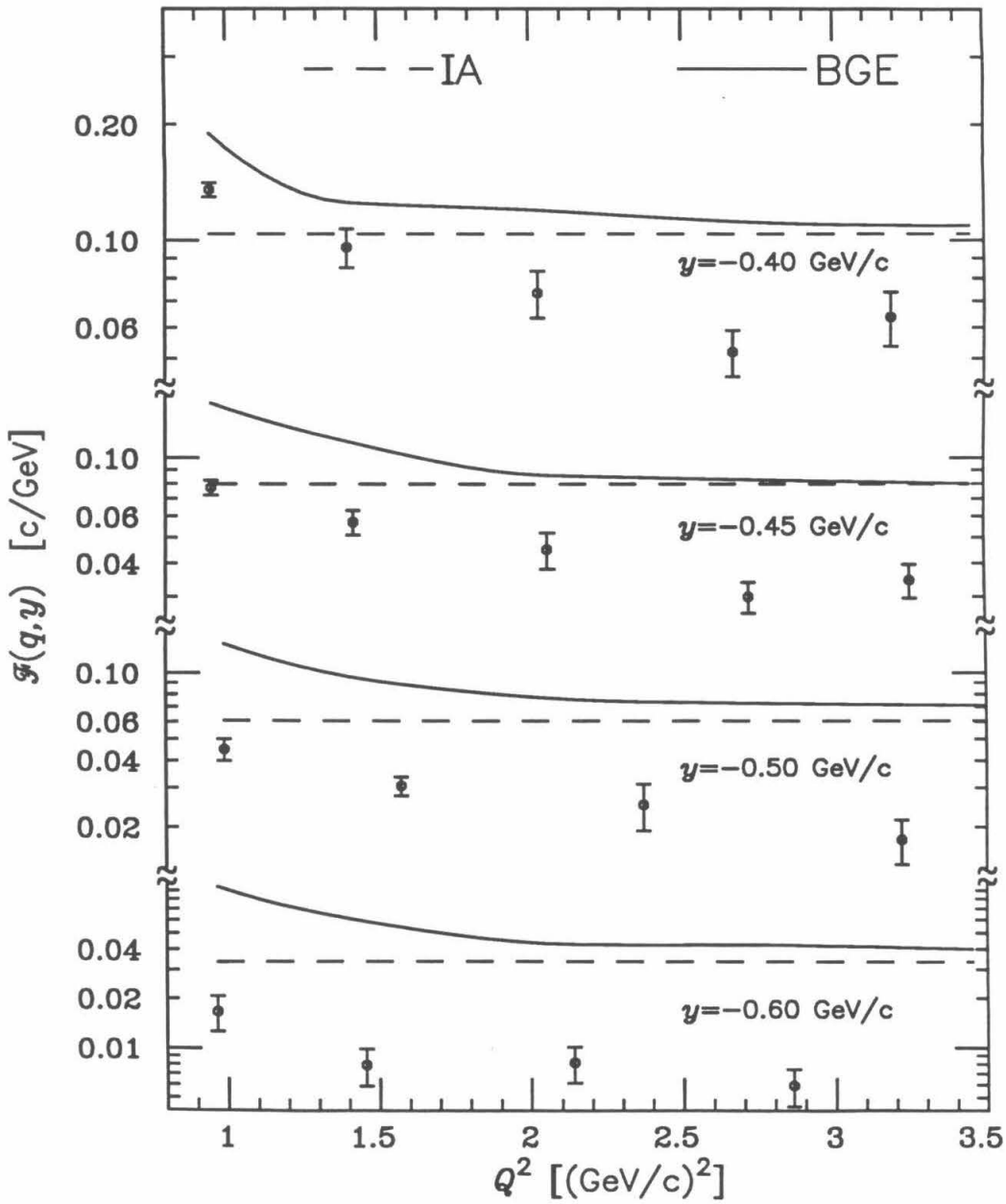

Figure 4.21 Comparison of our results to the NE3′ data for ^{56}Fe at higher Q^2. Notice that the data do seem to approach a scaling limit experimentally.

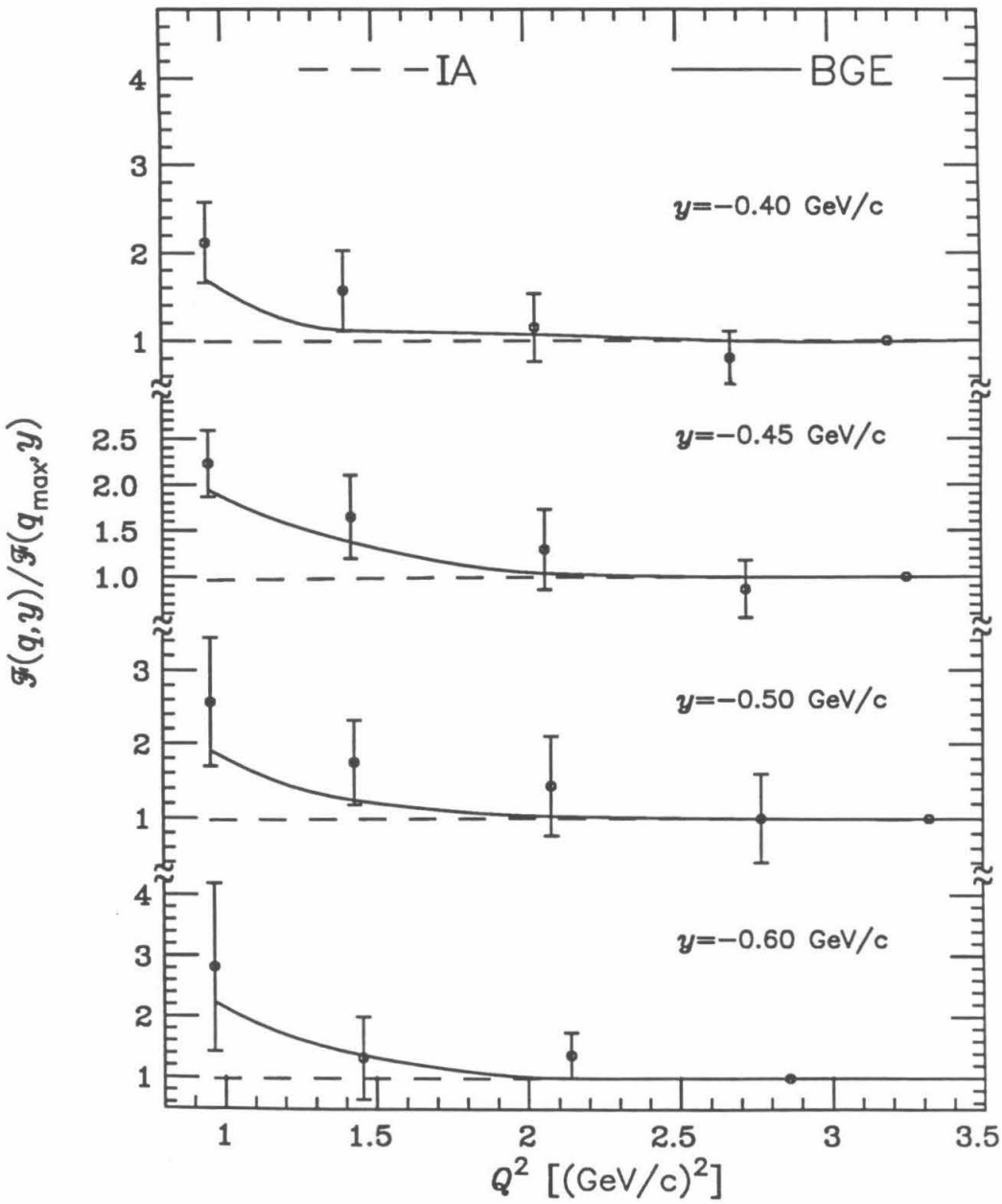

Figure 4.22 Approach to scaling for the ^{56}Fe NE3′ data. The agreement is the same or even better than in Fig. 4.20.

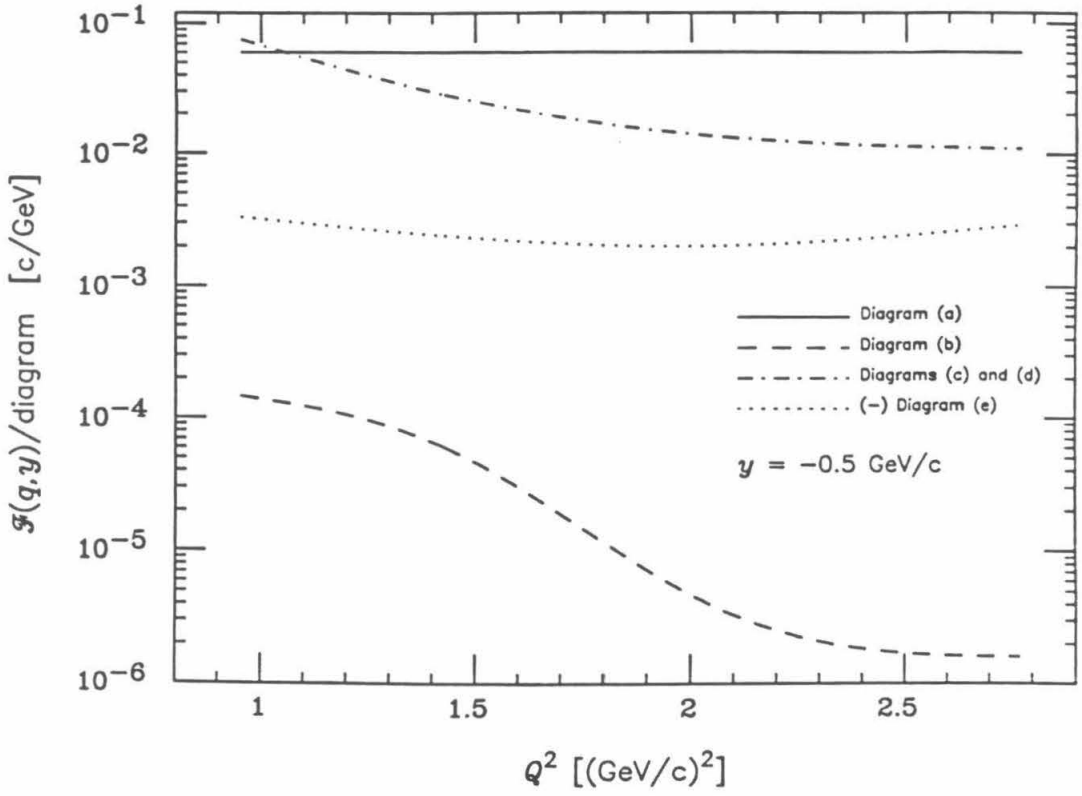

Figure 4.23 The contributions of various diagrams to the scaling function $\mathcal{F}(q,y)$. This is representative of all the situation for all of the values of y studied.

4.5 Other Results and Future Directions

Most other work to date on the problems of the scaling analysis have emphasized the problems with the kinematic factor, and also with the definition of y. Gurvitz and Rinat have studied the extraction of a scaling function using four different models for the scattering reaction (all non-relativistic) on a single particle in a potential well[64]. They found significant effects, but were very uncertain of the practicality of extending their results to a relativistic domain. We reviewed the work of Laget and Frankfurt and Strickman in Chapter 2, where they consider the effects of scattering from two nucleons in ^{3}He.

Vary and collaborators have been studying the effects of six- and nine-quark bags of the scattering cross section, should they be real and significant degrees of freedom in the nucleus. Pirner and Vary found that they could reproduce ωW_2 (as described in Chapter 2) for ^{3}He using this sort of model[65], and this would have immediate bearing on the extraction of a scaling function. Studies of the effects on the NE3 cross sections are in progress.

What should be next? Our calculations cannot really be extended to higher Q^2, because of its inherent non-relativistic nature. Relativistic nuclear many-body theories are currently undergoing a great deal of scrutiny, and Brockmann and Machleidt have been able to reproduce the empirical nuclear matter saturation energy and density from a relativistic Brueckner-Hartree-Fock calculation using a one-boson exchange potential which fits the N-N phase shifts [66]. If these theories turn out to have a rigorous founding, it might be interesting to repeat our calculation using a full relativistic framework, exploiting both the dynamics and kinematics present. It is also interesting that the Bonn potential has produced significantly softer tensor effects than other potentials[67], and as we pointed out, this may be a cure for our quantitative disagreement with the data.

From the experimental point of view, there are big problems. Higher Q^2's are

not really that practical, as the quasielastic peak is already getting lost under the deep-inelastic structure at the NE3 kinematics. One experiment that might yield intriguing results is NE9 at NPAS. The hope there is to take sufficient data to be able to extract the longitudinal and the transverse structure functions of the cross section separately This is done by fixing Q^2 and varying the scattering angle. Since the cross section is written as

$$\frac{d^2\sigma}{dE'd\Omega'} = \sigma_M \left(\left(\frac{Q^2}{\boldsymbol{q}^2} \right)^2 W_L(q, q \cdot P) + \frac{1}{2} \left(\frac{Q^2}{\boldsymbol{q}^2} + 2 \tan^2 \frac{\theta}{2} \right) W_T(q, q \cdot P) \right) \quad , \quad (4.17)$$

we can plot the differential cross section vs. $(Q^2/2\boldsymbol{q}^2 + \tan^2\theta/2)$ and extract W_T from the slope, and W_L from the intercept. This has already been done at low Q^2 by Barreau *et al.* [24] and Meziani *et al.* [25], who found that W_L seemed to be missing strength at the center of the quasielastic peak compared to naive Fermi gas estimates (which gave reasonable fits to W_T). Theoretical calculations seem to show that we understand where the strength has gone (correlation effects push the strength out into a tail at large energy transfer) [23], but these effects should also affect W_T at the peak. Measurements at high Q^2 should help sharpen our ideas about what is going on, as correlation effects in the peaks should get fairly small. Should theorists be able to fit both the transverse and the longitudinal cross sections independently, then we can strengthen our understanding of the reaction mechanism, and also of the behavior of the nucleon form factors in the medium. We look forward to this experiment with great interest.

Chapter 5

Summary and Conclusions

In Chapter 2, we reviewed the current state of inclusive quasielastic electron scattering on nuclei, especially as it relates to y-scaling. We discussed the problems that exist between theory and experiment, and discussed proposals to resolve the discrepancies.

Our approach was to look at the scaling analysis from the point of view of a microscopic many-body analysis. We chose nuclear matter as our test medium, and in Chapter 3, we reviewed the techniques of Brueckner-Goldstone theory, which we used to evaluate the dynamic structure function in nuclear matter.

In Chapter 4, we presented a microscopic calculation of the nuclear structure and two-body correlation effects on the extraction of a scaling function from quasielastic electron scattering. Although our results did not reproduce the quantitative results of experiment, the qualitative results were reproduced. Possible reasons for the discrepancies were discussed, and critically examined. The possible directions of theoretical work in the future were also discussed, with emphasis on the need for a comprehensive relativistic treatment of the nuclear many-body problem. The success of Machleidt and collaborators in reproducing the empirical saturation properties of nuclear matter may bode well for the development of such techniques.

Appendix I

Evaluation of G-Matrix Elements

We start with the partial wave expansions for both V and G;

$$\langle \boldsymbol{k}_1|V|\boldsymbol{k}_0\rangle = \frac{2}{\pi} \sum_{\substack{LL' \\ JSTM}} V^{JST}_{LL'}(k_1,k_0)\mathcal{Y}^M_{JLS}(\hat{\boldsymbol{k}}_1)\mathcal{Y}^{M\dagger}_{JL'S}(\hat{\boldsymbol{k}}_0)P_T \tag{I.1}$$

and

$$\langle \boldsymbol{P},\boldsymbol{k}_1|G|\boldsymbol{P},\boldsymbol{k}_0\rangle = \frac{2}{\pi} \sum_{\substack{LL' \\ JSTM}} G^{JST}_{LL'}(P;k_1,k_0)\mathcal{Y}^M_{JLS}(\hat{\boldsymbol{k}}_1)\mathcal{Y}^{M\dagger}_{JL'S}(\hat{\boldsymbol{k}}_0)P_T \quad . \tag{I.2}$$

P_T is the isospin operator for the two-body state, and $\mathcal{Y}^M_{JLS}(\hat{\boldsymbol{k}})$ is a spin-spherical harmonic, defined as

$$\mathcal{Y}^M_{JLS}(\hat{\boldsymbol{k}}_1) = \sum_{M_L M_S} \langle LM_L SM_S|JM\rangle\, Y_{LM_L}(\hat{\boldsymbol{k}}_1)\,|SM_s\rangle \quad , \tag{I.3}$$

with Y_{LM_L} a spherical harmonic, $\langle LM_L SM_S|JM\rangle$ a Clebsh-Gordon coefficient, and $|SM_S\rangle$ a spinor. The argument $\hat{\boldsymbol{k}}$ denotes the angular orientation of the unit vector.

The angle-averaged approximation for the Pauli operator Q will be used. It is given by the $L = 0$ component of a partial wave expansion, and in terms of center-of-mass momentum P, and relative momentum k'. It has the form

$$\overline{Q}(P,k') = \begin{cases} 0 & \text{if } P + k' < k_F; \\ \dfrac{k_F^2 - P^2 - k'^2}{2Pk'} & \text{if } \sqrt{P^2+k'^2} < k_F < P + k'; \\ 1 & \text{otherwise.} \end{cases} \tag{I.4}$$

We then substitute these expansions into the integral equation for G (Eqn. 3.6) to

find

$$\frac{2}{\pi}\sum_{\substack{LL'\\JSTM}} G^{JST}_{LL'}(P;k_1,k_0)\mathcal{Y}^M_{JLS}(\hat{\boldsymbol{k}}_1)\mathcal{Y}^{M\dagger}_{JL'S}(\hat{\boldsymbol{k}}_0)P_T$$

$$= \frac{2}{\pi}\sum_{\substack{LL'\\JSTM}} V^{JST}_{LL'}(k_1,k_0)\mathcal{Y}^M_{JLS}(\hat{\boldsymbol{k}}_1)\mathcal{Y}^{M\dagger}_{JL'S}(\hat{\boldsymbol{k}}_0)P_T$$

$$+\frac{4}{\pi^2}\sum_{\substack{LL'\\JSTM}}\sum_{\substack{ll'\\jstm}}\int d\boldsymbol{P}_a d\boldsymbol{k}_a V^{JST}_{LL'}(k_1,k_a)\mathcal{Y}^M_{JLS}(\hat{\boldsymbol{k}}_1)\mathcal{Y}^{M\dagger}_{JL'S}(\hat{\boldsymbol{k}}_a)P_T$$

$$G^{jst}_{ll'}(P_a;k_a,k_0)\mathcal{Y}^m_{jls}(\hat{\boldsymbol{k}}_a)\mathcal{Y}^{m\dagger}_{jl's}(\hat{\boldsymbol{k}}_0)P_t$$

$$\times\frac{\overline{Q}(P_a,k_a)\delta^3(\boldsymbol{P}-\boldsymbol{P}_a)}{W-e(\boldsymbol{P}_a+\boldsymbol{k}_a)-e(\boldsymbol{P}_a-\boldsymbol{k}_a)} \quad . \tag{I.5}$$

The delta function removes the center-of-mass integration, and then we can integrate over the angular component of the relative momentum $\boldsymbol{k}_a$ to get

$$\sum_{\substack{LL'\\JSTM}} G^{JST}_{LL'}(P;k_1,k_0)\mathcal{Y}^M_{JLS}(\hat{\boldsymbol{k}}_1)\mathcal{Y}^{M\dagger}_{JL'S}(\hat{\boldsymbol{k}}_0)P_T$$

$$= \sum_{\substack{LL'\\JSTM}} V^{JST}_{LL'}(k_1,k_0)\mathcal{Y}^M_{JLS}(\hat{\boldsymbol{k}}_1)\mathcal{Y}^{M\dagger}_{JL'S}(\hat{\boldsymbol{k}}_0)P_T$$

$$+\frac{2}{\pi}\sum_{\substack{LL'\\JSTM}}\sum_{L''}\int k_a^2 dk_a V^{JST}_{LL''}(k_1,k_a)G^{JST}_{L''L'}(P;k_a,k_0)\mathcal{Y}^M_{JLS}(\hat{\boldsymbol{k}}_1)\mathcal{Y}^{M\dagger}_{JL'S}(\hat{\boldsymbol{k}}_0)P_T$$

$$\times\frac{\overline{Q}(P,k_a)}{W-2e((P^2+k_a^2)^{1/2})} \quad . \tag{I.6}$$

Note that to do this we have averaged over the angle between $\boldsymbol{P}$ and $\boldsymbol{k}_a$ in the energy denominator. We can now use the orthogonality of each channel to show

$$G^{JST}_{LL'}(P;k_1,k_0) = V^{JST}_{LL'}(k_1,k_0)$$

$$+\frac{2}{\pi}\sum_{L''}\int k_a^2 dk_a \frac{V^{JST}_{LL''}(k_1,k_a)\overline{Q}(P,k_a)G^{JST}_{L''L'}(P;k_a,k_0)}{W-2e((P^2+k_a^2)^{1/2})} \quad . \tag{I.7}$$

This is the equation which we solve. Potentials are generally given in terms of their partial wave expansion, so it is quite straightforward to apply them here.

To solve the integral equation, we employ the method of Haftel and Tabakin [60], which is a direct solution of the equation using matrix methods. A general inhomogeneous integral equation has the form

$$F(x) = L(x) - \int dy K(x,y)F(y) \quad . \tag{I.8}$$

Assume for the moment that L and K are regular. We can discretize this as

$$F(x) = L(x) - \sum_{n=1}^{N} w_n K(x, y_n) F(y_n) \,, \tag{I.9}$$

where w_n and y_n are quadrature weights and points, respectively, and N is the number of quadrature points. If we solve for F at the points $y_1 ... y_N$, then we have N equations of the form

$$L(y_m) = \sum_{n=1}^{N} (K(y_m, y_n) + \delta_{mn}) F(y_n) \quad . \tag{I.10}$$

If we know L and K, we can solve these equations trivially using matrix inversion. Then F can be solved for arbitrary x.

But what if K is singular? This, in fact, is the case for the integral equation for the G-matrix. The solution will depend on the nature of the singularity. The singularity in Equation I.7 arises from the energy denominator. First, rewrite the starting energy as $W = W_0 + i\eta$. This tells us how to handle the contour integration. We find the pole from noting that there exists some k_s such that $W_0 = 2e((P^2 + k_s^2)^{1/2})$. We use the knowledge that $e(k) = k^2/2M + U(k)$, and that where U is important its behavior is well approximated by a quadratic in k. This means that the singularity is first order. Now we can replace $W - 2E$ by

$$(k_a^2 - k_s^2 + i\eta) C(k_a) \quad , \tag{I.11}$$

where

$$C(k_a) = \frac{(W_0 - 2E)}{(k_a^2 - k_s^2)} \,, \tag{I.12}$$

where $C(k_a)$ is now well behaved for $k_a \to k_s$. Why would this help? If there is a singularity in an integrand, there are two contributions to the results, one a principal value (PV) integral, and the other from the contour integration around the singularity. To evaluate the PV integral, we need to be able to eliminate the singularity in the integrand. First we note that

$$P.V. \int_0^\infty dx \frac{1}{x^2 - x_0^2} = 0 \quad . \tag{I.13}$$

This then tells us that

$$X(k_s)\int_0^\infty dk \frac{1}{k^2-k_s^2} = 0 \quad . \tag{I.14}$$

We can then define

$$X_{LL'}(k_s) = \sum_{L''} k_s^2 V_{LL''}(k_1,k_s)\overline{Q}(P,k_s)\frac{G_{L''L'}(P;k_s,k_0)}{C(k_s)} \quad , \tag{I.15}$$

so that we can rewrite Eqn. I.7 as

$$\begin{aligned} G^{JST}_{LL'}(P;k_1,k_0) &= V^{JST}_{LL'}(k_1,k_0) \\ &+ \left(\frac{2}{\pi}\int_0^\infty dk_a \, \frac{X^{JST}_{LL'}(k_a) - X^{JST}_{LL'}(k_s)}{k_a^2-k_s^2} + i\frac{X^{JST}_{LL'}(k_s)}{k_s}\right) , \end{aligned} \tag{I.16}$$

where we now have a principal value integral, since the singularity has been removed smoothly. It is now trivial to apply the matrix inversion techniques mentioned previously, except that now we solve for a complex-valued function.

We need to input the potential in momentum space, the single-particle potential, and the starting energy W. The latter we discussed in Chap. 3. First let us evaluate the potential in momentum space in each angular momentum channel. We need to evaluate $V^{JST}_{LL'}(k_1,k_0)$ explicitly, given $V(\boldsymbol{r},\boldsymbol{r}')$. We express V as

$$V(\boldsymbol{r},\boldsymbol{r}') = \sum_{\substack{LL' \\ JSTM}} V^{JST}_{LL'}(r)\mathcal{Y}^M_{JLS}(\hat{\boldsymbol{r}})\mathcal{Y}^{M\dagger}_{JL'S}(\hat{\boldsymbol{r}}')P_T \, , \tag{I.17}$$

where, for the potentials we use, $V^{JST}_{LL'}(r,r') = V^{JST}_{LL'}(r)\delta(r-r')$. Then we can write

$$\langle \boldsymbol{k}_1|V|\boldsymbol{k}_0\rangle = \int d\boldsymbol{r}\,d\boldsymbol{r}' e^{-i\boldsymbol{k}_1\cdot\boldsymbol{r}} e^{i\boldsymbol{k}_0\cdot\boldsymbol{r}'} V(\boldsymbol{r},\boldsymbol{r}') \, . \tag{I.18}$$

If the potential can be written as a sum of Yukawa terms (as can Reid Soft Core and Paris), then the transformation to momentum space is trivial and given by Haftel and Tabakin [60]. The transformations for the different Yukawa structures are as follows:

$$\int_0^\infty dr r^2 j_L(kr)\frac{e^{-mr}}{mr}j_L(k'r) = \frac{1}{2kk'}Q_L(z) \tag{I.19}$$

$$\int_0^\infty dr r^2 j_L(kr)\Big(\frac{1}{mr}+\frac{1}{(mr)^2}\Big)\frac{e^{-mr}}{mr}j_L(k'r)=\frac{-1}{2(2L+1)}(Q_{L+1}(z)-Q_{L-1}(z)) \quad \text{(I.20)}$$

$$\int_0^\infty dr r^2 j_L(kr)\frac{e^{-mr}}{mr}j_{L+2}(k'r)=\frac{k^2Q_{L+2}(z)+k'^2Q_l(z)}{2kk'}-Q_{L+1}(z) \quad \text{(I.21)}$$

where

$$z=\frac{k^2+k'^2+m^2}{2kk'}\,. \quad \text{(I.22)}$$

j_L is a spherical Bessel function, and Q_L is a Legendre polynomial of the second kind. Other essential Yukawa terms for RSC tensor terms are

$$\int_0^\infty dr r^2 j_0(kr)\frac{e^{-mr}}{mr}j_2(k'r)=\frac{1}{4kk'^3}\Big[6kk'+\frac{1}{2}(3m^2+k'^2-3k^2)\ln\Big(\frac{z+1}{z-1}\Big) + 6mk\Big\{\arctan\Big(\frac{m}{k+k'}\Big)-\arctan\Big(\frac{m}{k-k'}\Big)\Big\}\Big] \quad \text{(I.23)}$$

and

$$\int_0^\infty dr r^2 j_{L+1}(kr)\frac{e^{-mr}}{mr}j_{L+3}(k'r)=\frac{2L+5}{2L+3}\frac{k}{k'}\Big(\int_0^\infty dr r^2 j_L(kr)\frac{e^{-mr}}{mr}j_{L+2}(k'r)+\frac{Q_{L+2}(z)}{2kk'}\Big) - \frac{Q_{L+1}(z)}{2kk'}\,. \quad \text{(I.24)}$$

(The latter can be used to evaluate higher-order terms from the first). There is one other expression needed for the quadratic spin-orbit term of the Paris potential,

$$\int_0^\infty dr r^2 j_L(kr)\frac{1}{(mr)^2}\Big(1+\frac{3}{mr}+\frac{3}{(mr)^2}\Big)\frac{e^{-mr}}{mr}j_L(k'r)=\frac{1}{2}\frac{kk'}{m^5}(z^2-1)Q_L^{-2}(z)\,. \quad \text{(I.25)}$$

These are all easily confirmed using integral tables [68].

The potential energy is calculated in the Hartree-Fock approximation as mentioned in Chapter 2. We start with

$$U(k)=\frac{1}{4\rho}\sum_{k_1<k_F}\langle \boldsymbol{k},\boldsymbol{k}_1|G|b\boldsymbol{k},\boldsymbol{k}_1\rangle-\langle \boldsymbol{k},\boldsymbol{k}_1|G|\boldsymbol{k}_1,\boldsymbol{k}\rangle\,, \quad \text{(I.26)}$$

and now we need to consider the exchange structure of a G-matrix element. In the center of mass representation,

$$U(k)=\frac{1}{4\rho}\sum_{|\boldsymbol{P}-\boldsymbol{k}_0|<k_F}\langle \boldsymbol{P},\boldsymbol{k}_0|G|\boldsymbol{P},\boldsymbol{k}_0\rangle-\langle \boldsymbol{P},\boldsymbol{k}_0|G|\boldsymbol{P},-\boldsymbol{k}_0\rangle\,. \quad \text{(I.27)}$$

We now use Eqn. I.2 to look at $\langle \boldsymbol{P}, \boldsymbol{k}_0 | G | \boldsymbol{P}, -\boldsymbol{k}_0 \rangle$. It is given by

$$\langle \boldsymbol{P}, \boldsymbol{k}_0 | G | \boldsymbol{P}, -\boldsymbol{k}_0 \rangle = \frac{2}{\pi} \sum_{\substack{LL' \\ JSTM}} G^{JST}_{LL'}(P; k_1, k_0) \mathcal{Y}^M_{JLS}(\hat{\boldsymbol{k}}_0) \mathcal{Y}^{M\dagger}_{JL'S}(-\hat{\boldsymbol{k}}_0)(-)^T P_T \qquad \text{(I.28)}$$

and it is immediately obvious that

$$\langle \boldsymbol{P}, \boldsymbol{k}_0 | G | \boldsymbol{P}, -\boldsymbol{k}_0 \rangle = \frac{2}{\pi} \sum_{\substack{LL' \\ JSTM}} (-)^{L+S+T} G^{JST}_{LL'}(P; k_1, k_0) \mathcal{Y}^M_{JLS}(\hat{\boldsymbol{k}}_0) \mathcal{Y}^{M\dagger}_{JL'S}(-\hat{\boldsymbol{k}}_0) P_T \, . \qquad \text{(I.29)}$$

The N-N interaction is given only for states with $L + S + T$ odd (because the nucleons are fermions), so if we restrict our sum to such states, then we find that

$$\langle \boldsymbol{P}, \boldsymbol{k}_0 | G | \boldsymbol{P}, -\boldsymbol{k}_0 \rangle = -\langle \boldsymbol{P}, \boldsymbol{k}_0 | G | \boldsymbol{P}, \boldsymbol{k}_o \rangle \, , \qquad \text{(I.30)}$$

and that

$$U(k) = \frac{2}{4\rho} \sum_{|\boldsymbol{P} - \boldsymbol{k}_0| < k_F} \langle \boldsymbol{P}, \boldsymbol{k}_0 | G | \boldsymbol{P}, \boldsymbol{k}_0 \rangle \, . \qquad \text{(I.31)}$$

It is now fairly simple to write $U(k)$ in terms of the partial wave amplitudes as

$$U(k) = \frac{1}{2\rho} \sum_{k_1 < k_F} \sum_{\substack{JST \\ L}} G^{JST}_{LL}(P; \frac{|\boldsymbol{k} - \boldsymbol{k}_1|}{2}, \frac{|\boldsymbol{k} - \boldsymbol{k}_1|}{2}) \, , \qquad \text{(I.32)}$$

where ρ is the density of nucleons in nuclear matter, and $P = |\boldsymbol{k} + \boldsymbol{k}_1|/2$. Practically, this turns into an integral of the form

$$k < k_F$$

$$U(k) = \frac{4}{\pi} \frac{\hbar^2}{M} \frac{1}{k} \sum_{JSTL} (2J+1)(2T+1) \Big(\int_0^{(k_F - k)/2} dk_0 k_0 \int_{|k-k_0|}^{k+k_0} dP P \, G^{JST}_{LL}(P; k_0, k_0)$$
$$+ \int_{(k_F - k)/2}^{(k_F + k)/2} dk_0 k_0 \int_{|k-k_0|}^{\sqrt{(k_F^2 + k^2)/2 - k_0^2}} dP P \, G^{JST}_{LL}(P; k_0, k_0) \Big) \qquad \text{(I.33)}$$

$$k > k_F$$

$$U(k) = \frac{4}{\pi} \frac{\hbar^2}{M} \frac{1}{k} \sum_{JSTL} (2J+1)(2T+1)$$
$$\int_{(k - k_F)/2}^{(k_F + k)/2} dk_0 k_0 \int_{|k-k_0|}^{\sqrt{(k_F^2 + k^2)/2 - k_0^2}} dP P \, G^{JST}_{LL}(P; k_0, k_0) \, . \qquad \text{(I.34)}$$

It has been shown by Banerjee and others [60,69,70,71] that the center of mass dependence of G can be replaced by evaluating G at an average center of mass momentum $\overline{P}$ for each k_0. $\overline{P}$ is given by

$$\overline{P}^2(k,k_0,k_F) = \begin{cases} k^2+k_0^2 & 2k_0 \le k_F - k \\ k^2+k_0^2-\frac{1}{4}(2k_0+k-k_F)(2k_0+k+k_F) & k_F - k \le 2k_0 \le k_F + k\,. \end{cases} \tag{I.35}$$

In fact, the real dependence of G on P is rather weak, and the $\overline{P}$ dependence is a fairly good approximation. [69,71] In Fig. I.1 we plot the G-matrix elements from various channels against P as given in Refs. [69] and [71]. We can see that the

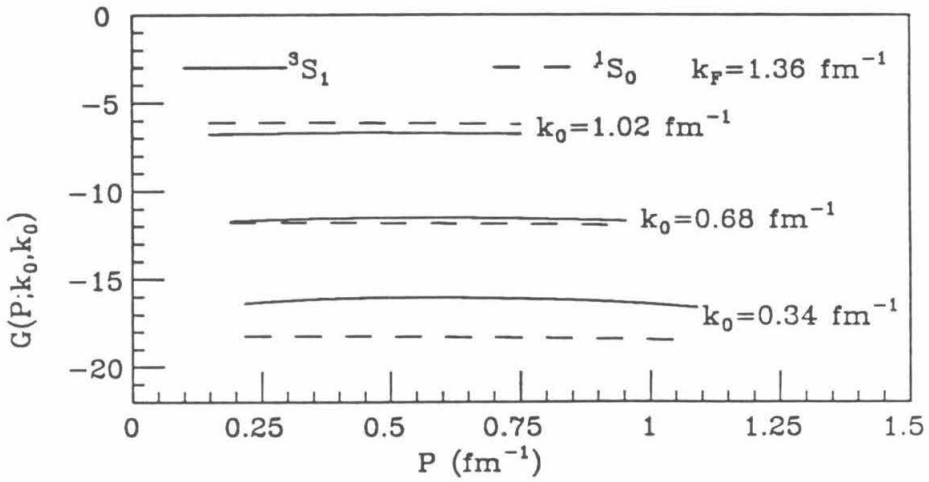

Figure I.1 The dependence of G-matrix elements on the center-of-mass momentum P. Numbers are from Refs. [69,71].

variation is on the order of 2–3%. This weak dependence will allow us to work with average center-of-mass momenta for all matrix elements.

Using these approximations, we now have an expression for $U(k)$ given by

$k < k_F$

$$U(k) = \frac{8}{\pi}\frac{\hbar^2}{M}\sum_{JSTL}(2J+1)(2T+1)\Big(\int_0^{(k_F-k)/2} dk_0 k_0^2\, G_{LL}^{JST}(\overline{P};k_0,k_0) + \frac{1}{k}\int_{(k_F-k)/2}^{(k_F+k)/2} dk_0 k_0 (\frac{1}{4}(k_F^2-k^2)-k_0(k_0-k))\, G_{LL}^{JST}(\overline{P};k_0,k_0)\Big) \quad \text{(I.36)}$$

$k > k_F$

$$U(k) = \frac{8}{\pi}\frac{\hbar^2}{M}\sum_{JSTL}(2J+1)(2T+1) \frac{1}{k}\int_{(k-k_F)/2}^{(k_F+k)/2} dk_0 k_0 (\frac{1}{4}(k_F^2-k^2)-k_0(k_0-k))\, G_{LL}^{JST}(\overline{P};k_0,k_0)\Big). \quad \text{(I.37)}$$

This integral is evaluated numerically using Simpson's rule. Ten points were used for each interval, and the effect of doubling this number was about a 0.5% change. For practical reasons, the potential is evaluated at a restricted series of points and then fit to analytic forms for various regions. Following the lead of Jeukenne *et al.* [49], we fit to a parabolic form for $k < 2k_F$, and to a Gaussian form for $k > 2k_F$ (the actual analytic form for this region is not very critical. As seen in Chap. 3, the potential is insignificant with respect to the kinetic energy for $k > 2k_F$). The points used for the fitting actually overlap both of these regions to ensure a smooth continuation of the potential.

A last topic which needs to be discussed is the behavior of adjoints of the G-matrices. If we return to the original equation for G as taken from a ladder summation, then we have

$$\langle \boldsymbol{k}_1,\boldsymbol{k}_2|G|\boldsymbol{k}_3,\boldsymbol{k}_4\rangle = \langle \boldsymbol{k}_1,\boldsymbol{k}_2|V|\boldsymbol{k}_3,\boldsymbol{k}_4\rangle + \sum_{k_a,k_b>k_F}\frac{\langle \boldsymbol{k}_1,\boldsymbol{k}_2|V|\boldsymbol{k}_a,\boldsymbol{k}_b\rangle\langle \boldsymbol{k}_a,\boldsymbol{k}_b|G|\boldsymbol{k}_3,\boldsymbol{k}_4\rangle}{W-e(\boldsymbol{k}_a)-e(\boldsymbol{k}_b)}. \quad \text{(I.38)}$$

But the ladder sum could also be written in such a way as to give

$$\langle \boldsymbol{k}_1,\boldsymbol{k}_2|G|\boldsymbol{k}_3,\boldsymbol{k}_4\rangle = \langle \boldsymbol{k}_1,\boldsymbol{k}_2|V|\boldsymbol{k}_3,\boldsymbol{k}_4\rangle + \sum_{k_a,k_b>k_F}\frac{\langle \boldsymbol{k}_1,\boldsymbol{k}_2|G|\boldsymbol{k}_a,\boldsymbol{k}_b\rangle\langle \boldsymbol{k}_a,\boldsymbol{k}_b|V|\boldsymbol{k}_3,\boldsymbol{k}_4\rangle}{W-e(\boldsymbol{k}_a)-e(\boldsymbol{k}_b)}. \quad \text{(I.39)}$$

It is fairly trivial to see that if W is chosen such that the energy denominator is never singular, then $\langle \boldsymbol{k}_1, \boldsymbol{k}_2 | G(W) | \boldsymbol{k}_3, \boldsymbol{k}_4 \rangle = (\langle \boldsymbol{k}_3, \boldsymbol{k}_4 | G(W) | \boldsymbol{k}_1, \boldsymbol{k}_2 \rangle)^\dagger$. However, if the denominator vanishes, then the problem might be more subtle. Consider the case where $W = \omega + i\eta$. Now the expression for G is

$$\langle \boldsymbol{k}_1, \boldsymbol{k}_2 | G | \boldsymbol{k}_3, \boldsymbol{k}_4 \rangle = \langle \boldsymbol{k}_1, \boldsymbol{k}_2 | V | \boldsymbol{k}_3, \boldsymbol{k}_4 \rangle + \sum_{k_a, k_b > k_F} \frac{\langle \boldsymbol{k}_1, \boldsymbol{k}_2 | V | \boldsymbol{k}_a, \boldsymbol{k}_b \rangle \langle \boldsymbol{k}_a, \boldsymbol{k}_b | G | \boldsymbol{k}_3, \boldsymbol{k}_4 \rangle}{\omega - e(\boldsymbol{k}_a) - e(\boldsymbol{k}_b) + i\eta} . \tag{I.40}$$

If we conjugate this, we get

$$\langle \boldsymbol{k}_3, \boldsymbol{k}_4 | G | \boldsymbol{k}_1, \boldsymbol{k}_2 \rangle = \langle \boldsymbol{k}_3, \boldsymbol{k}_4 | V | \boldsymbol{k}_1, \boldsymbol{k}_2 \rangle + \sum_{k_a, k_b > k_F} \frac{\langle \boldsymbol{k}_3, \boldsymbol{k}_4 | G | \boldsymbol{k}_a, \boldsymbol{k}_b \rangle \langle \boldsymbol{k}_a, \boldsymbol{k}_b | V | \boldsymbol{k}_1, \boldsymbol{k}_2 \rangle}{\omega - e(\boldsymbol{k}_a) - e(\boldsymbol{k}_b) - i\eta} . \tag{I.41}$$

We can see that Eqn. I.39 is the integral equation for $\langle \boldsymbol{k}_3, \boldsymbol{k}_4 | G(\omega - i\eta) | \boldsymbol{k}_1, \boldsymbol{k}_2 \rangle$. It is then clear that $\langle \boldsymbol{k}_3, \boldsymbol{k}_4 | G(\omega + i\eta) | \boldsymbol{k}_1, \boldsymbol{k}_2 \rangle = \langle \boldsymbol{k}_1, \boldsymbol{k}_2 | G(\omega - i\eta) | \boldsymbol{k}_3, \boldsymbol{k}_4 \rangle$. Now, when we have a term $\langle \boldsymbol{k}_3, \boldsymbol{k}_4 | G(\omega + i\eta) | \boldsymbol{k}_1, \boldsymbol{k}_2 \rangle + \langle \boldsymbol{k}_1, \boldsymbol{k}_2 | G(\omega + i\eta) | \boldsymbol{k}_3, \boldsymbol{k}_4 \rangle$, this translates to $\langle \boldsymbol{k}_3, \boldsymbol{k}_4 | G(\omega + i\eta) | \boldsymbol{k}_1, \boldsymbol{k}_2 \rangle + \langle \boldsymbol{k}_3, \boldsymbol{k}_4 | G(\omega - i\eta) | \boldsymbol{k}_1, \boldsymbol{k}_2 \rangle$, where the imaginary parts will cancel and leave us with twice the real part. This is an important point when considering RPA type diagrams and also some of the important diagrams in the main expansion.

Appendix II

Detailed Algebraic Expansions of Diagrams

Here we will deal with the detailed algebraic expressions for the diagrams discussed in Chapter 4. Their partial wave expansions are also discussed, along with methods for dealing with the angular integrations when necessary. The first two diagrams of Fig. 4.10 are discussed in the most detail, as they demonstrate nicely all the techniques used for the other diagrams. One point of notational convenience– when writing the G-matrix elements, the notation $\langle \boldsymbol{k}_1, \boldsymbol{k}_2 | G | \boldsymbol{k}_3, \boldsymbol{k}_4 \rangle$ will be used for on-shell matrix elements, and the starting energy will be implicit from the diagram. The off-shell elements will be written $\langle \boldsymbol{k}_1, \boldsymbol{k}_2 | \mathcal{G}(\omega + i\eta) | \boldsymbol{k}_3, \boldsymbol{k}_4 \rangle$, where again the starting energy is assumed implicit from the diagram, but the "external" contribution is mentioned, as the sign of the contribution of the imaginary part will be important in some of the diagrams.

II.1 Diagram (a)

First, let us discuss the direct IA term.

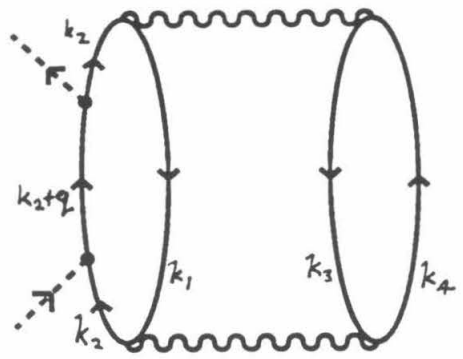

It can be expanded as

$$
\begin{aligned}
S_a(q,\omega) = -\frac{1}{2\pi\rho}\mathrm{Im}\int d\boldsymbol{k}_1 d\boldsymbol{k}_2 d\boldsymbol{k}_3 d\boldsymbol{k}_4 \\
&\langle \boldsymbol{k}_1,\boldsymbol{k}_3|G|\boldsymbol{k}_2,\boldsymbol{k}_4\rangle\langle \boldsymbol{k}_2,\boldsymbol{k}_4|G|\boldsymbol{k}_1,\boldsymbol{k}_3\rangle \\
&\times \frac{1}{(e(\boldsymbol{k}_1)+e(\boldsymbol{k}_3)-e(\boldsymbol{k}_2)-e(\boldsymbol{k}_4))^2} \\
&\times \frac{1}{\omega+e(\boldsymbol{k}_1)+e(\boldsymbol{k}_3)-e(\boldsymbol{k}_2+\boldsymbol{q})-e(\boldsymbol{k}_4)+i\eta} \\
&\times \Theta(k_F-|\boldsymbol{k}_1|)\Theta(k_F-|\boldsymbol{k}_3|)\Theta(|\boldsymbol{k}_2|-k_F)\Theta(|\boldsymbol{k}_4|-k_F) \\
&\times \Theta(|\boldsymbol{k}_2+\boldsymbol{q}|-k_F) \\
&\times \delta^3(\boldsymbol{k}_1+\boldsymbol{k}_3-\boldsymbol{k}_2-\boldsymbol{k}_4)\,.
\end{aligned}
\tag{II.1}
$$

This includes the exchange term, which we can evaluate using the information in Appendix I. We make a transformation to center-of-mass coordinates $\boldsymbol{P} = (\boldsymbol{k}_1 + \boldsymbol{k}_3)/2$ and $\boldsymbol{k}_0 = (\boldsymbol{k}_1 - \boldsymbol{k}_3)/2$. Then we can write

$$
\begin{aligned}
S_a(q,\omega) = -\frac{4}{\pi\rho}\mathrm{Im}\int d\boldsymbol{P} d\boldsymbol{k}_0 d\boldsymbol{k}_2 \,\frac{1}{D_1^2}\frac{1}{D_2}\Theta_1\Theta_2\Theta_3\Theta_4\Theta_5 \\
\langle \boldsymbol{P}\boldsymbol{k}_0|G|\boldsymbol{P},\boldsymbol{k}_2{-}\boldsymbol{P}\rangle\langle \boldsymbol{P},\boldsymbol{k}_2{-}\boldsymbol{P}|G|\boldsymbol{P},\boldsymbol{k}_0\rangle\,,
\end{aligned}
\tag{II.2}
$$

where the integration over $\boldsymbol{k}_4$ has been performed to remove the δ-function. Note

also the definitions

$$D_1 = e(\boldsymbol{P}+\boldsymbol{k}_0) + e(\boldsymbol{P}-\boldsymbol{k}_0) - e(\boldsymbol{k}_2) - e(2\boldsymbol{P}-\boldsymbol{k}_2)$$

$$D_2 = \omega + e(\boldsymbol{P}+\boldsymbol{k}_0) + e(\boldsymbol{P}-\boldsymbol{k}_0) - e(\boldsymbol{k}_2+\boldsymbol{q}) - e(2\boldsymbol{P}-\boldsymbol{k}_2) + i\eta$$

$$\Theta_1 = \Theta(k_F - |\boldsymbol{P}-\boldsymbol{k}_0|)\ ,\ \Theta_2 = \Theta(k_F - |\boldsymbol{P}+\boldsymbol{k}_0|)$$

$$\Theta_3 = \Theta(|\boldsymbol{k}_2| - k_F)\ ,\ \Theta_4 = \Theta(|2\boldsymbol{P}-\boldsymbol{k}_2| - k_F)$$

$$\Theta_5 = \Theta(|\boldsymbol{k}_2 + \boldsymbol{q}| - k_F) \quad .$$

Now define (for notation) $\boldsymbol{k}' = \boldsymbol{k}_2 - \boldsymbol{P}$. This will be used for the evaluation of the G-matrix elements.

Consider first the product of G-matrix elements $\langle \boldsymbol{P}, \boldsymbol{k}_0|G|\boldsymbol{P}, \boldsymbol{k}'\rangle\langle \boldsymbol{P}, \boldsymbol{k}'|G|\boldsymbol{P}, \boldsymbol{k}_0\rangle$. Using the partial wave expansions, we can rewrite this as

$$\left(\frac{2}{\pi}\right)^2 \sum_{\substack{JST\\LL'}} \sum_{\substack{jst\\ll'}} i^{l-l'+L-L'} G^{JST}_{LL'}(P;k_0,k') G^{jst}_{ll'}(P;k',k_0)$$
$$\times \sum_{mm_t} \sum_{MM_T} \mathcal{Y}^m_{jls}(\hat{\boldsymbol{k}}') \mathcal{Y}^{m\dagger}_{jl's}(\hat{\boldsymbol{k}}_0) \mathcal{Y}^M_{JLS}(\hat{\boldsymbol{k}}_0) \mathcal{Y}^{M\dagger}_{JL'S}(\hat{\boldsymbol{k}}') \langle tm_t|TM_T\rangle \ . \quad \text{(II.3)}$$

If G is purely real, then $G^{JST}_{LL'}(P;k_0,k') = G^{JST}_{L'L}(P;k',k_0)$ (from Appendix I), and we can sum over m, M, m_t, M_T to get

$$\frac{1}{4\pi^4} \sum_{\substack{JST\\LL'}} (2J+1)(2T+1) |G^{JST}_{LL'}(P;k',k_0)|^2 \ . \quad \text{(II.4)}$$

We can insert this into Eqn. II.2 to get

$$S_a(q,\omega) = -\frac{1}{\pi^5\rho} \sum_{\substack{JST\\LL'}} (2J+1)(2T+1)$$
$$\text{Im} \int d\boldsymbol{P} d\boldsymbol{k}_0 d\boldsymbol{k}_2 \, |G^{JST}_{LL'}(P;k',k_0)|^2 \frac{1}{D_1^2} \frac{1}{D_2} \Theta_1\Theta_2\Theta_3\Theta_4\Theta_5 \quad \text{(II.5)}$$

II.2 Diagram (b)

Now we consider the two-nucleon term of IA.

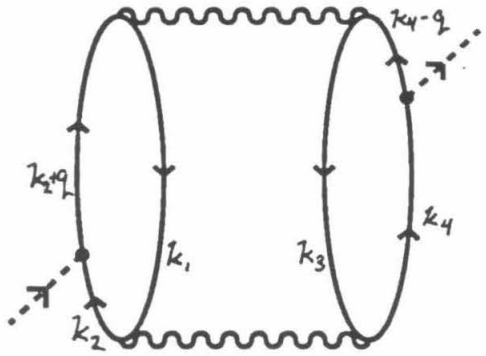

It is interesting because it now has $\boldsymbol{q}$ as part of the argument of a G-matrix element. Here we will see how angular momentum mixing works in all the rest of the diagrams. The full expression can be written as

$$
\begin{aligned}
S_b(q,\omega) = -\frac{1}{2\pi\rho}\mathrm{Im}\int d\boldsymbol{k}_1 d\boldsymbol{k}_2 d\boldsymbol{k}_3 d\boldsymbol{k}_4 \\
&\langle \boldsymbol{k}_1, \boldsymbol{k}_3 | G | \boldsymbol{k}_2{+}\boldsymbol{q}, \boldsymbol{k}_4{-}\boldsymbol{q}\rangle \langle \boldsymbol{k}_2, \boldsymbol{k}_4 | G | \boldsymbol{k}_1, \boldsymbol{k}_3\rangle \\
&\times \frac{1}{e(\boldsymbol{k}_1)+e(\boldsymbol{k}_3)-e(\boldsymbol{k}_2{+}\boldsymbol{q})-e(\boldsymbol{k}_4{-}\boldsymbol{q})} \\
&\times \frac{1}{D_1}\frac{1}{D_2}\Theta_1\Theta_2\Theta_3\Theta_4\Theta_5\,\Theta(|\boldsymbol{k}_4-\boldsymbol{q}|-k_F) \\
&\times \delta^3(\boldsymbol{k}_1+\boldsymbol{k}_3-\boldsymbol{k}_2-\boldsymbol{k}_4)\,.
\end{aligned}
\tag{II.6}
$$

Here, one of the G-matrix elements carries a momentum $\boldsymbol{q}$. The main effect of this in the analytic structure is to change the angular momentum couplings between the two interactions in the diagram. We write

$$
\begin{aligned}
\langle \boldsymbol{k}_1, \boldsymbol{k}_3 | G | \boldsymbol{k}_2{+}\boldsymbol{q}, \boldsymbol{k}_4{-}\boldsymbol{q}\rangle &= \langle \boldsymbol{P}, \boldsymbol{k}_0 | G | \boldsymbol{P}, \boldsymbol{k}'{+}\boldsymbol{q}\rangle \\
&= \left(\frac{2}{\pi}\right)\sum_{\substack{JST\\LL'\\MM_T}} G^{JST}_{LL'}(P; k_0, |\boldsymbol{k}'{+}\boldsymbol{q}|)\, \mathcal{Y}^{M}_{JLS}(\hat{\boldsymbol{k}}_0)\, \mathcal{Y}^{M\dagger}_{JL'S}(\widehat{\boldsymbol{k}'{+}\boldsymbol{q}})|TM_T\rangle\,.
\end{aligned}
\tag{II.7}
$$

Coupling this to the other G-matrix element gives

$$\left(\frac{2}{\pi}\right)^2 \sum_{\substack{JST\\LL'}} \sum_{\substack{jst\\ll'}} i^{l-l'+L-L'} G^{JST}_{LL'}(P;k_0,|\boldsymbol{k}'+\boldsymbol{q}|) G^{jst}_{ll'}(P;k',k_0) \times \sum_{mM} \mathcal{Y}^{m}_{jls}(\hat{\boldsymbol{k}}') \mathcal{Y}^{m\dagger}_{jl's}(\hat{\boldsymbol{k}}_0) \mathcal{Y}^{M}_{JLS}(\hat{\boldsymbol{k}}_0) \mathcal{Y}^{M\dagger}_{JL'S}(\widehat{\boldsymbol{k}'+\boldsymbol{q}}) \sum_{m_t M_T} \langle t m_t | T M_T \rangle \,. \tag{II.8}$$

We can see that there is closure in $\hat{\boldsymbol{k}}_0$, so that we have $\delta_{Ll'}\delta_{Jj}$. However, the closure does not work over $\hat{\boldsymbol{k}}'$, so that all combinations of l and L' should be considered.

Thus, the final result for S_b is then

$$\begin{aligned} S_b(q,\omega) = -\frac{4}{\pi^3\rho}\mathrm{Im} \int d\boldsymbol{P} d\boldsymbol{k}_0 d\boldsymbol{k}' \sum_{\substack{JST\\LL'l}} i^{l-L'}(2T+1) \\ G^{JST}_{L'L}(P;|\boldsymbol{k}'+\boldsymbol{q}|,k_0) G^{JST}_{lL}(P;k',k_0) \sum_{M} \mathcal{Y}^{M}_{JlS}(\hat{\boldsymbol{k}}') \mathcal{Y}^{M\dagger}_{JL'S}(\widehat{\boldsymbol{k}'+\boldsymbol{q}}) \\ \times \frac{1}{e(\boldsymbol{P}+\boldsymbol{k}_0)+e(\boldsymbol{P}-\boldsymbol{k}_0)-e(\boldsymbol{P}+\boldsymbol{k}'+\boldsymbol{q})-e(\boldsymbol{P}-\boldsymbol{k}'-\boldsymbol{q})} \\ \times \frac{1}{D_1}\frac{1}{D_2}\Theta_1\Theta_2\Theta_3\Theta_4\Theta_5\,\Theta(|\boldsymbol{P}-\boldsymbol{k}'-\boldsymbol{q}|-k_F) \end{aligned} \tag{II.9}$$

How the angular integrations over $\widehat{\boldsymbol{k}'}$ are performed should be discussed. We can expand the product over spherical harmonics as

$$\mathcal{Y}^{M}_{JlS}(\hat{\boldsymbol{k}}')\mathcal{Y}^{M\dagger}_{JL'S}(\widehat{\boldsymbol{k}'+\boldsymbol{q}}) = \frac{1}{2\pi} \sum_{\substack{m_l m_{L'}\\ m_S M_S}} \langle l m_l S m_S | J M\rangle \langle L' m_{L'} S M_S | J M\rangle \bar{P}_l^{m_l}(\theta_{\boldsymbol{k}'}) \bar{P}_{L'}^{m_{L'}}(\theta_{\boldsymbol{k}'+\boldsymbol{q}}) \times e^{i m_l \phi} e^{-i m_{L'}\phi} \langle S M_s | S m_S\rangle \,. \tag{II.10}$$

From this we get $\delta_{m_l m_{L'}}$ and $\delta_{M_S m_S}$. Then we are left with

$$\frac{1}{2\pi} \sum_{m_l m_S} \langle l m_l S m_S | J M\rangle \langle L' m_l S m_S | J M\rangle \bar{P}_l^{m_l}(\theta_{\boldsymbol{k}'}) \bar{P}_{L'}^{m_l}(\theta_{\boldsymbol{k}'+\boldsymbol{q}}) \,. \tag{II.11}$$

$\bar{P}$ is the normalized form of the associated Legendre function. The relation between $\cos\theta_{\boldsymbol{k}'}$ and $\cos\theta_{\boldsymbol{k}'+\boldsymbol{q}}$ is easily derived. If we consider $\boldsymbol{q}$ to be in the z-direction, then we can use Fig. II.1 to show that

$$\cos\theta_{\boldsymbol{k}'+\boldsymbol{q}} = \frac{q + k'\cos\theta_{\boldsymbol{k}'}}{\sqrt{q^2+k'^2+2qk'\cos\theta_{\boldsymbol{k}'}}} \,. \tag{II.12}$$

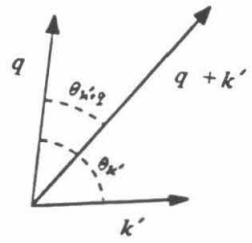

Figure II.1 The relation between $\theta_{k'}$ and $\theta_{k'+q}$, assuming that q points along the z-axis.

The integrals can now be performed using Gauss-Legendre quadrature, which is discussed in the main text.

At this point, it is sufficient just to list the general expression and the angular momentum expansion for each of the remaining diagrams. All the techniques for expanding carry through.

II.3 Diagrams (c) and (d)

Now we begin evaluating the final-state interaction diagrams. The first of these are actually paired, in the sense that they appear as time-reversed cases of one another. These are diagrams (c) and (d) of Fig. 4.10.

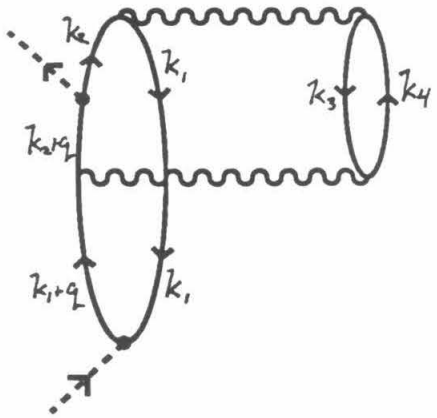

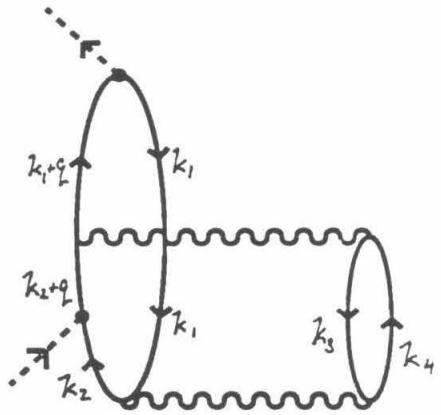

The general expressions for these are given by

$$
\begin{aligned}
S_c(q,\omega) = -\frac{1}{\pi\rho}\mathrm{Im}\int d\boldsymbol{k}_1 d\boldsymbol{k}_2 d\boldsymbol{k}_3 d\boldsymbol{k}_4 \\
&\frac{\langle \boldsymbol{k}_1, \boldsymbol{k}_3 | G | \boldsymbol{k}_2, \boldsymbol{k}_4 \rangle \langle \boldsymbol{k}_2{+}\boldsymbol{q}, \boldsymbol{k}_4 | \mathcal{G}(\omega + i\eta) | \boldsymbol{k}_1{+}\boldsymbol{q}, \boldsymbol{k}_3 \rangle}{(e(\boldsymbol{k}_1) + e(\boldsymbol{k}_3) - e(\boldsymbol{k}_2) - e(\boldsymbol{k}_4))} \\
&\times \frac{1}{\omega + e(\boldsymbol{k}_1) + e(\boldsymbol{k}_3) - e(\boldsymbol{k}_2{+}\boldsymbol{q}) - e(\boldsymbol{k}_4) + i\eta} \\
&\times \frac{1}{\omega + e(\boldsymbol{k}_1) - e(\boldsymbol{k}_1{+}\boldsymbol{q}) + i\eta} \qquad \text{(II.13)} \\
&\times \Theta(k_F - |\boldsymbol{k}_1|)\Theta(k_F - |\boldsymbol{k}_3|)\Theta(|\boldsymbol{k}_2| - k_F)\Theta(|\boldsymbol{k}_4| - k_F) \\
&\times \Theta(|\boldsymbol{k}_2{+}\boldsymbol{q}| - k_F)\Theta(|\boldsymbol{k}_1{+}\boldsymbol{q}| - k_F) \\
&\times \delta^3(\boldsymbol{k}_1 + \boldsymbol{k}_3 - \boldsymbol{k}_2 - \boldsymbol{k}_4)
\end{aligned}
$$

and

$$
\begin{aligned}
S_d(q,\omega) = -\frac{1}{\pi\rho}\mathrm{Im}\int d\boldsymbol{k}_1 d\boldsymbol{k}_2 d\boldsymbol{k}_3 d\boldsymbol{k}_4 \\
&\frac{\langle \boldsymbol{k}_1{+}\boldsymbol{q},\boldsymbol{k}_3|\mathcal{G}(\omega+i\eta)|\boldsymbol{k}_2{+}\boldsymbol{q},\boldsymbol{k}_4\rangle\langle \boldsymbol{k}_2,\boldsymbol{k}_4|G|\boldsymbol{k}_1,\boldsymbol{k}_3\rangle}{(e(\boldsymbol{k}_1)+e(\boldsymbol{k}_3)-e(\boldsymbol{k}_2)-e(\boldsymbol{k}_4))} \\
&\times \frac{1}{\omega+e(\boldsymbol{k}_1)+e(\boldsymbol{k}_3)-e(\boldsymbol{k}_2{+}\boldsymbol{q})-e(\boldsymbol{k}_4)+i\eta} \\
&\times \frac{1}{\omega+e(\boldsymbol{k}_1)-e(\boldsymbol{k}_1{+}\boldsymbol{q})+i\eta} \\
&\times \Theta(k_F-|\boldsymbol{k}_1|)\Theta(k_F-|\boldsymbol{k}_3|)\Theta(|\boldsymbol{k}_2|-k_F)\Theta(|\boldsymbol{k}_4|-k_F) \\
&\times \Theta(|\boldsymbol{k}_2{+}\boldsymbol{q}|-k_F)\Theta(|\boldsymbol{k}_1{+}\boldsymbol{q}|-k_F) \\
&\times \delta^3(\boldsymbol{k}_1+\boldsymbol{k}_3-\boldsymbol{k}_2-\boldsymbol{k}_4)\,.
\end{aligned}
\tag{II.14}
$$

These two expressions can be combined to form

$$
\begin{aligned}
S_{c+d}(q,\omega) = -\frac{1}{\pi\rho}\mathrm{Im}\int d\boldsymbol{k}_1 d\boldsymbol{k}_2 d\boldsymbol{k}_3 d\boldsymbol{k}_4 \\
&[(\langle \boldsymbol{k}_1{+}\boldsymbol{q},\boldsymbol{k}_3|\mathcal{G}(\omega+i\eta)|\boldsymbol{k}_2{+}\boldsymbol{q},\boldsymbol{k}_4\rangle\langle \boldsymbol{k}_2,\boldsymbol{k}_4|G|\boldsymbol{k}_1,\boldsymbol{k}_3\rangle \\
&+\langle \boldsymbol{k}_1,\boldsymbol{k}_3|G|\boldsymbol{k}_2,\boldsymbol{k}_4\rangle\langle \boldsymbol{k}_2{+}\boldsymbol{q},\boldsymbol{k}_4|\mathcal{G}(\omega+i\eta)|\boldsymbol{k}_1{+}\boldsymbol{q},\boldsymbol{k}_3\rangle] \\
&\times \frac{1}{(e(\boldsymbol{k}_1)+e(\boldsymbol{k}_3)-e(\boldsymbol{k}_2)-e(\boldsymbol{k}_4))} \\
&\times \frac{1}{\omega+e(\boldsymbol{k}_1)+e(\boldsymbol{k}_3)-e(\boldsymbol{k}_2{+}\boldsymbol{q})-e(\boldsymbol{k}_4)+i\eta} \\
&\times \frac{1}{\omega+e(\boldsymbol{k}_1)-e(\boldsymbol{k}_1{+}\boldsymbol{q})+i\eta} \\
&\times \Theta(k_F-|\boldsymbol{k}_1|)\Theta(k_F-|\boldsymbol{k}_3|)\Theta(|\boldsymbol{k}_2|-k_F)\Theta(|\boldsymbol{k}_4|-k_F) \\
&\times \Theta(|\boldsymbol{k}_2{+}\boldsymbol{q}|-k_F)\Theta(|\boldsymbol{k}_1{+}\boldsymbol{q}|-k_F) \\
&\times \delta^3(\boldsymbol{k}_1+\boldsymbol{k}_3-\boldsymbol{k}_2-\boldsymbol{k}_4)\,,
\end{aligned}
\tag{II.15}
$$

and it can be shown, using the discussion in Appendix I, that only the real parts of the $\mathcal{G}$-matrices survive this addition. We can go through the same procedures as

for the previous diagrams to find

$$
\begin{aligned}
S_{c+d}(q,\omega) = -\frac{16}{\pi^5\rho}\mathrm{Im}\int d\boldsymbol{P}d\boldsymbol{k}_0 d\boldsymbol{k}' \frac{1}{D_1 D_2} \quad & \frac{1}{\omega+e(\boldsymbol{P}+\boldsymbol{k}_0)-e(\boldsymbol{P}+\boldsymbol{k}_0+\boldsymbol{q})+i\eta} \\
& \times \sum_{\substack{LL' \\ \mathcal{L}\mathcal{L}' \\ J\mathcal{J}ST}} (i)^{L-L'+\mathcal{L}'-\mathcal{L}} G_{LL'}^{JST}(P;k',k_0) \\
& \quad \mathrm{Re}\,\{\mathcal{G}_{\mathcal{L}'\mathcal{L}}^{\mathcal{J}ST}(|\boldsymbol{P}+\boldsymbol{q}/2||\boldsymbol{k}_0+\boldsymbol{q}/2|,|\boldsymbol{k}'+\boldsymbol{q}/2|)\} \\
& \times \sum_{\substack{M \\ abcd}} \langle L'aSb|JM\rangle\langle LcSd|JM\rangle \qquad \text{(II.16)} \\
& \quad \times\langle \mathcal{L}'aSb|\mathcal{J}M\rangle\langle \mathcal{L}cSd|\mathcal{J}M\rangle \\
& \times \bar{P}_{L'}^{a}(\theta_{\boldsymbol{k}_0})\bar{P}_{\mathcal{L}'}^{a}(\theta_{\boldsymbol{k}_0+\boldsymbol{q}/2})\bar{P}_{L}^{c}(\theta_{\boldsymbol{k}'})\bar{P}_{\mathcal{L}}^{c}(\theta_{\boldsymbol{k}'+\boldsymbol{q}/2}) \\
& \times \Theta_1\Theta_2\Theta_3\Theta_4\Theta_5\Theta(|\boldsymbol{P}+\boldsymbol{k}_0+\boldsymbol{q}|-k_F)\,.
\end{aligned}
$$

II.4 Diagram (e)

The last important contribution comes from diagram (e) of Fig. 4.10.

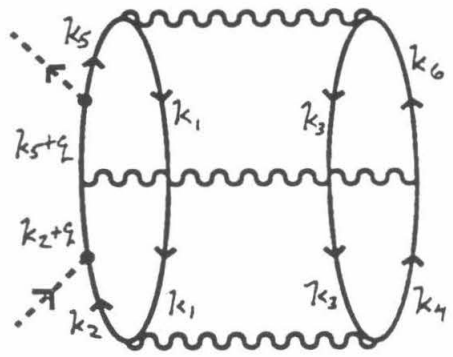

We can write it out as

$$
\begin{aligned}
S_e(q,\omega) = -\frac{1}{\pi\rho}\mathrm{Im}\int & d\boldsymbol{k}_1 d\boldsymbol{k}_2 d\boldsymbol{k}_3 d\boldsymbol{k}_4 d\boldsymbol{k}_5 d\boldsymbol{k}_6 \\
& \langle \boldsymbol{k}_1, \boldsymbol{k}_3 | G | \boldsymbol{k}_2, \boldsymbol{k}_4 \rangle \langle \boldsymbol{k}_2{+}\boldsymbol{q}, \boldsymbol{k}_4 | \mathcal{G}(\omega + i\eta) | \boldsymbol{k}_5{+}\boldsymbol{q}, \boldsymbol{k}_6 \rangle \langle \boldsymbol{k}_5, \boldsymbol{k}_6 | G | \boldsymbol{k}_1, \boldsymbol{k}_3 \rangle \\
& \times \frac{1}{e(\boldsymbol{k}_1) + e(\boldsymbol{k}_3) - e(\boldsymbol{k}_2) - e(\boldsymbol{k}_4)} \\
& \times \frac{1}{e(\boldsymbol{k}_1) + e(\boldsymbol{k}_3) - e(\boldsymbol{k}_5) - e(\boldsymbol{k}_6)} \\
& \times \frac{1}{\omega + e(\boldsymbol{k}_1) + e(\boldsymbol{k}_3) - e(\boldsymbol{k}_2{+}\boldsymbol{q}) - e(\boldsymbol{k}_4) + i\eta} \\
& \times \frac{1}{\omega + e(\vec{k}_1) + e(\boldsymbol{k}_4) - e(\boldsymbol{k}_5{+}\boldsymbol{q}) - e(\boldsymbol{k}_6) + i\eta} \\
& \times \Theta(k_F - |\boldsymbol{k}_1|)\Theta(k_F - |\boldsymbol{k}_3|)\Theta(|\boldsymbol{k}_2| - k_F)\Theta(|\boldsymbol{k}_4| - k_F) \\
& \times \Theta(|\boldsymbol{k}_5| - k_F)\Theta(|\boldsymbol{k}_6| - k_F)\Theta(|\boldsymbol{k}_2{+}\boldsymbol{q}| - k_F)\Theta(|\boldsymbol{k}_5{+}\boldsymbol{q}| - k_F) \\
& \times \delta^3(\boldsymbol{k}_1 + \boldsymbol{k}_3 - \boldsymbol{k}_2 - \boldsymbol{k}_4) \\
& \times \delta^3(\boldsymbol{k}_1 + \boldsymbol{k}_3 - \boldsymbol{k}_5 - \boldsymbol{k}_6)\,.
\end{aligned}
\tag{II.17}
$$

The final expression for this diagram is given by

$$
\begin{aligned}
S_e(q,\omega) = -\frac{4}{\pi^7\rho}\mathrm{Im}\int d\boldsymbol{P}d\boldsymbol{k}_0 d\boldsymbol{k}' d\boldsymbol{k}''
&\sum_{\substack{LL'\\ ll'\\ \mathcal{L}}}\sum_{\substack{J_j\\ ST}}(2T+1)i^{L-\mathcal{L}+l-l'} \\
&G^{JST}_{LL'}(P;k'',k_0)G^{JST}_{\mathcal{L}L'}(P;k',k_0) \\
&\mathcal{G}^{jST}_{ll'}(|\boldsymbol{P}+\boldsymbol{q}/2|;|\boldsymbol{k}'+\boldsymbol{q}/2|,|\boldsymbol{k}''+\boldsymbol{q}/2|) \\
&\times \sum_{\substack{abe\\ M=a+b}} \langle \mathcal{L}aSb|JM\rangle\langle laSb|jM\rangle \qquad \text{(II.18)} \\
&\quad \times\langle LeSM-e|JM\rangle\langle l'eSM-e|jM\rangle \\
&\times \bar{P}^a_{\mathcal{L}}(\theta_{\boldsymbol{k}'})\bar{P}^a_l(\theta_{\boldsymbol{k}'+\boldsymbol{q}/2})\bar{P}^e_L(\theta_{\boldsymbol{k}''})\bar{P}^e_{l'}(\theta_{\boldsymbol{k}''+\boldsymbol{q}/2}) \\
&\times \frac{1}{e(\boldsymbol{P}+\boldsymbol{k}_0)+e(\boldsymbol{P}-\boldsymbol{k}_0)-e(\boldsymbol{P}+\boldsymbol{k}')-e(\boldsymbol{P}-\boldsymbol{k}')} \\
&\times \frac{1}{e(\boldsymbol{P}+\boldsymbol{k}_0)+e(\boldsymbol{P}-\boldsymbol{k}_0)-e(\boldsymbol{P}+\boldsymbol{k}'')-e(\boldsymbol{P}-\boldsymbol{k}'')} \qquad \text{(II.19)} \\
&\times \frac{1}{\omega+e(\boldsymbol{P}+\boldsymbol{k}_0)+e(\boldsymbol{P}-\boldsymbol{k}_0)-e(\boldsymbol{P}+\boldsymbol{k}'+\boldsymbol{q})-e(\boldsymbol{P}-\boldsymbol{k}')+i\eta} \\
&\times \frac{1}{\omega+e(\boldsymbol{P}+\boldsymbol{k}_0)+e(\boldsymbol{P}-\boldsymbol{k}_0)-e(\boldsymbol{P}+\boldsymbol{k}''+\boldsymbol{q})-e(\boldsymbol{P}-\boldsymbol{k}'')+i\eta} \\
&\times \Theta(k_F-|\boldsymbol{P}+\boldsymbol{k}_0|)\Theta(k_F-|\boldsymbol{P}-\boldsymbol{k}_0|) \\
&\times \Theta(|\boldsymbol{P}+\boldsymbol{k}'|-k_F)\Theta(|\boldsymbol{P}-\boldsymbol{k}'|-k_F) \\
&\times \Theta(|\boldsymbol{P}+\boldsymbol{k}''|-k_F)\Theta(|\boldsymbol{P}-\boldsymbol{k}''|-k_F) \\
&\times \Theta(|\boldsymbol{P}+\boldsymbol{k}''+\boldsymbol{q}|-k_F)\Theta(|\boldsymbol{P}+\boldsymbol{k}'+\boldsymbol{q}|-k_F)\,.
\end{aligned}
$$

II.5 Diagrams (f) and (g)

There are two diagrams that we have not yet discussed. These are (f) and (g) of Fig. 4.10. Both are easily written as

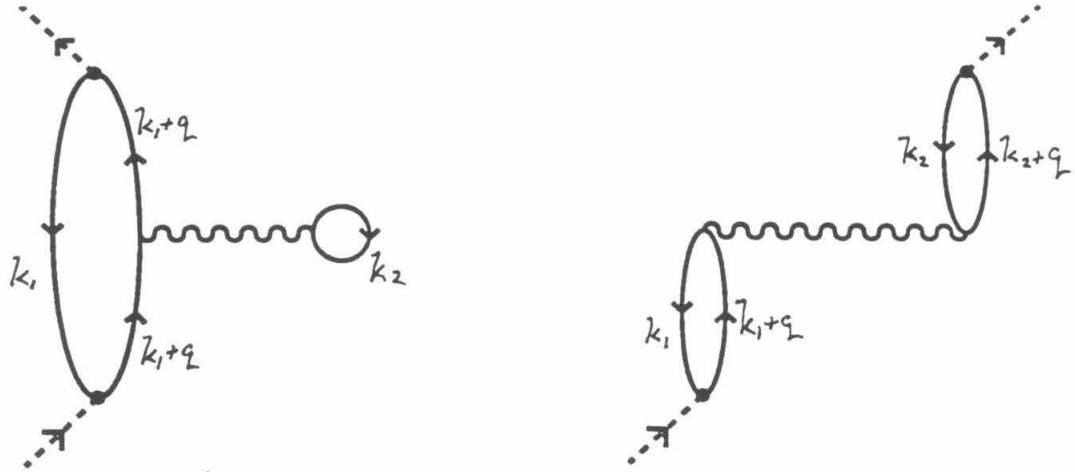

$$S_f(q,\omega) = -\frac{1}{2\pi\rho}\mathrm{Im}\int d\boldsymbol{k}_1 d\boldsymbol{k}_2 \langle \boldsymbol{k}_1+\boldsymbol{q}, \boldsymbol{k}_2|\mathcal{G}(\omega+i\eta)|\boldsymbol{k}_1+\boldsymbol{q}, \boldsymbol{k}_2\rangle$$

$$\times \frac{1}{(\omega + e(\boldsymbol{k}_1) - e(\boldsymbol{k}_1+\boldsymbol{q}) + i\eta)^2} \qquad \text{(II.20)}$$

$$\times \Theta(k_F - k_1)\Theta(k_F - k_2)\Theta(|\boldsymbol{k}_1+\boldsymbol{q}| - k_F) \qquad \text{(II.21)}$$

$$S_g(q,\omega) = -\frac{1}{2\pi\rho}\mathrm{Im}\int d\boldsymbol{k}_1 d\boldsymbol{k}_2 \langle \boldsymbol{k}_1+\boldsymbol{q}, \boldsymbol{k}_2|\mathcal{G}(\omega+i\eta)|\boldsymbol{k}_1, \boldsymbol{k}_2+\boldsymbol{q}\rangle$$

$$\times \frac{1}{(\omega + e(\boldsymbol{k}_1) - e(\boldsymbol{k}_1+\boldsymbol{q}) + i\eta)}$$

$$\times \frac{1}{(\omega + e(\boldsymbol{k}_2) - e(\boldsymbol{k}_2+\boldsymbol{q}) + i\eta)} \qquad \text{(II.22)}$$

$$\times \Theta(k_F - k_1)\Theta(k_F - k_2)$$

$$\times \Theta(|\boldsymbol{k}_1+\boldsymbol{q}| - k_F)\Theta(|\boldsymbol{k}_2+\boldsymbol{q}| - k_F)\,. \qquad \text{(II.23)}$$

We can rewrite the expression for S_g under exchange of the two particles in the intial state to yield

$$S_g(q,\omega) = \frac{1}{2\pi\rho}\mathrm{Im}\int d\boldsymbol{k}_1 d\boldsymbol{k}_2 \langle \boldsymbol{k}_1+\boldsymbol{q}, \boldsymbol{k}_2|\mathcal{G}(\omega+i\eta)|\boldsymbol{k}_2+\boldsymbol{q}, \boldsymbol{k}_1\rangle$$
$$\times \frac{1}{(\omega + e(\boldsymbol{k}_1) - e(\boldsymbol{k}_1+\boldsymbol{q}) + i\eta)}$$
$$\times \frac{1}{(\omega + e(\boldsymbol{k}_2) - e(\boldsymbol{k}_2+\boldsymbol{q}) + i\eta)} \qquad \text{(II.24)}$$
$$\times \Theta(k_F - k_1)\Theta(k_F - k_2)$$
$$\times \Theta(|\boldsymbol{k}_1+\boldsymbol{q}| - k_F)\Theta(|\boldsymbol{k}_2+\boldsymbol{q}| - k_F)\,. \qquad \text{(II.25)}$$

Now let us take the $Q^2 \to \infty$ limit of both expressions. This yields

$$S_f(q,\omega) = -\frac{1}{2\pi\rho}\mathrm{Im}\int d\boldsymbol{k}_1 d\boldsymbol{k}_2 \langle \boldsymbol{q}, 0|\mathcal{G}(\omega+i\eta)|\boldsymbol{q}, 0\rangle$$
$$\times \frac{1}{(\omega - e(\boldsymbol{q}) + i\eta)^2} \qquad \text{(II.26)}$$
$$\times \Theta(k_F - k_1)\Theta(k_F - k_2)$$

$$S_g(q,\omega) = \frac{1}{2\pi\rho}\mathrm{Im}\int d\boldsymbol{k}_1 d\boldsymbol{k}_2 \langle \boldsymbol{q}, 0|\mathcal{G}(\omega+i\eta)|\boldsymbol{q}, 0\rangle \qquad \text{(II.27)}$$
$$\times \frac{1}{(\omega - e(\boldsymbol{q}) + i\eta)^2}$$
$$\times \Theta(k_F - k_1)\Theta(k_F - k_2)\,. \qquad \text{(II.28)}$$

It is obvious now that these two terms are equal and opposite, and thus will cancel exactly. Of course, we are not in the $Q^2 \to \infty$ limit, but q is much larger than k_F, and it may well be a good approximation. For the sake of argument they are calculated, and the final expressions used are

$$S_f(q,\omega) = -\frac{2}{\pi^3\rho}\mathrm{Im}\int d\boldsymbol{P} d\boldsymbol{k}_0$$
$$\sum_{LJST}(2J+1)(2T+1)\mathcal{G}_{LL}^{JST}(|\boldsymbol{P}+\boldsymbol{q}/2|; |\boldsymbol{k}_0+\boldsymbol{q}/2|, |\boldsymbol{k}_0+\boldsymbol{q}/2|)$$
$$\times \frac{1}{(\omega + e(\boldsymbol{P}+\boldsymbol{k}_0) - e(\boldsymbol{P}+\boldsymbol{k}_0+\boldsymbol{q}) + i\eta)^2} \qquad \text{(II.29)}$$
$$\times \Theta(k_F - |\boldsymbol{P}-\boldsymbol{k}_0|)\Theta(k_F - |\boldsymbol{P}+\boldsymbol{k}_0|)$$
$$\times \Theta(|\boldsymbol{P}+\boldsymbol{k}_0+\boldsymbol{q}| - k_F) \qquad \text{(II.30)}$$

$$S_g(q,\omega) = \frac{4}{\pi^3\rho}\mathrm{Im}\int d\boldsymbol{P}d\boldsymbol{k}_0 \sum_{\substack{JST\\LL'}}(2T+1)$$

$$\mathcal{G}^{JST}_{LL'}(|\boldsymbol{P}+\boldsymbol{q}/2|;|\boldsymbol{k}_0-\boldsymbol{q}/2|,|\boldsymbol{k}_0+\boldsymbol{q}/2|)$$

$$\sum_{Mm_L}\langle Lm_LSM-m_l|JM\rangle\langle L'm_LSM-m_L|JM\rangle$$

$$\bar{P}^{m_L}_L(\theta_{\boldsymbol{k}_0+\boldsymbol{q}/2})\bar{P}^{m_L}_{l'}(\theta_{\boldsymbol{k}_0-\boldsymbol{q}/2})$$

$$\times\frac{1}{(\omega+e(\boldsymbol{P}+\boldsymbol{k}_0)-e(\boldsymbol{P}+\boldsymbol{k}_0+\boldsymbol{q})+i\eta)} \qquad \text{(II.31)}$$

$$\times\frac{1}{(\omega+e(\boldsymbol{P}-\boldsymbol{k}_0)-e(\boldsymbol{P}-\boldsymbol{k}_0+\boldsymbol{q})+i\eta)}$$

$$\times\Theta(k_F-|\boldsymbol{P}+\boldsymbol{k}_0|)\Theta(k_F-|\boldsymbol{P}-\boldsymbol{k}_0|)$$

$$\times\Theta(|\boldsymbol{P}+\boldsymbol{k}_0+\boldsymbol{q}|-k_F)\Theta(|\boldsymbol{P}-\boldsymbol{k}_0+\boldsymbol{q}|-k_F)\,. \qquad \text{(II.32)}$$

References

[1] M.A. MacGregor, R.A. Arndt and R.M. Wright, Phys. Rev. **182**, 1714 (1969).

[2] S.O. Bäckman, G.E. Brown and J.A. Niskamin, Phys. Rep. **124**, 1 (1985).

[3] R. deTourreil, B. Rouben and D.W.L. Sprung, Nucl. Phys. **A242**, 445 (1975).

[4] For recent work on ^{3}He$(e, e'p)$, see E. Jans *et al.*, Phys. Rev. Lett. **49**, 974 (1982).

[5] For a review of NIKHEF work, see P.K.A. de Witt Huberts, In *New Vistas in Electronuclear Physics,* page 331 NATO Advanced Study Institute, Plenum 1986.

[6] J.D. Bjorken, Phys. Rev. **179**, 1547 (1969).

[7] For a complete review of the early days of scaling in deep inelastic scatterin, see J.L. Friedman and H.W. Kendall, Ann. Rev. Nucl. Sci. **22**, 203 (1972).

[8] G. West, Phys. Rep. **18**, 263 (1975).

[9] Y. Kawazoe, G. Takeda and H. Matsuzaki, Prog. Theor. Phys. **54**, 1394 (1975).

[10] For a complete review of the applications of QCD to deep inelastic electron scattering, see E. Reya, Phys. Rep. **69**, 195 (1981).

[11] I. Sick, Phys. Lett. **157B**, 13 (1985).

[12] R.D. McKeown, Phys. Rev. Lett. **56**, 1452 (1986).

[13] D. Day *et al.*, Phys. Rev. Lett. **43**, 1143 (1979).

[14] E. J. Moniz, Phys. Rev. **184**, 1154 (1969).

[15] H.A. Mook, Phys. Rev. Lett. **55**, 2452 (1985).

[16] V.F. Sears, E.C Stevenson, P. Martel and A.D.B. Woods, Phys. Rev. Lett. **49**, 279 (1982).

[17] I. Sick, D. Day and J.S. McCarthy, Phys. Rev. Lett. **45**, 871 (1980).

[18] P. Bosted, R.G. Arnold, S. Rock and Z. Szalata, Phys. Rev. Lett. **49**, 1380 (1982).

[19] W. Schütz *et al.*, Phys. Rev. Lett. **38**, 259 (1977).

[20] J. D. Bjorken and S. D. Drell, *Relativistic Quantum Mechanics*, McGraw-Hill Book Company 1964.

[21] T.W. Donnelly, In *New Vistas in Electronuclear Physics*, pages 151, NATO Advanced Study Institute, Plenum 1986.

[22] C. Cioffi degli Atti, E. Pace and G. Salmè, Phys. Lett. **127B**, 303 (1983).

[23] R. Schiavilla, A. Fabrocini and V.R. Pandharipande, University of Illinois Preprint No. ILL-(NU)-87-#18, (1987).

[24] P. Barreau *et al.*, Nucl. Phys. **A402**, 515 (1983).

[25] Z.E. Meziani *et al.*, Phys. Rev. Lett. **52**, 2130 (1984).

[26] P.D. Zimmerman, C.F. Williamson and Y. Kawazoe, Phys. Rev. **C19**, 279 (1979).

[27] S. Rock *et al.*, Phys. Rev. **C26**, 1592 (1982).

[28] R.V. Reid, Ann. of Phys. **50**, 411 (1968).

[29] H. Meier-Hajduk, Ch. Hajduk, P.U. Sauer and W. Thies, Nucl. Phys. **A395**, 332 (1983).

[30] P.U. Sauer, *Electron and Photon Interactions at Intermediate Energies,* page 256, Volume 234 of *Lecture Notes in Physics,* Springer-Verlag 1984.

[31] C. Cioffi degli Atti, Il Nuovo Cimento **76A**, 330 (1983).

[32] D.B. Day *et al.*, Submitted to Phys. Rev. Lett. (1987).

[33] D. Potterveld, Private Communication.

[34] J. Laget, In *New Vistas in Electronuclear Physics,* page 361 NATO Advanced Study Institute, Plenum 1986.

[35] L.L. Frankfurt and M.I. Strickman, Phys. Rep. **76**, 215 (1981).

[36] S.A. Gurvitz, TRIUMF Preprint No. TRI-PP-84-85, (1984).

[37] For a complete review of early effective interactions, see D.M. Brink, *Nuclear Forces*, Pergamon Press New York 1965.

[38] T.H.R. Skyrme, Phil. Mag. **1**, 1043 (1956).

[39] T.H.R. Skyrme, Nucl. Phys. **9**, 615 (1959).

[40] D. Vautherin and D.M. Brink, Phys. Rev. **C5**, 626 (1972).

[41] M. Beiner, H. Flocard, N. Van Giai and P. Quentin, Nucl. Phys. **A238**, 29 (1975).

[42] P. Quentin and H. Flocard, Ann. Rev. Nucl. Sci. **28**, 523 (1978).

[43] J. Negele and D. Vautherin, Phys. Rev. **C5**, 1472 (1972).

[44] J. Negele and D. Vautherin, Phys. Rev. **C11**, 1030 (1975).

[45] H.A. Bethe, Ann. Rev. Nucl. Sci. **21**, 93 (1971).

[46] D.W.L. Sprung, page 225, Volume 5 of *Advances in Nuclear Physics,* Plenum (N.Y.), 1972.

[47] B.D. Day, Rev. Mod. Phys. **50**, 495 (1978).

[48] H.A. Bethe, B.H. Brandow and A.G. Petschek, Phys. Rev. **129**, 225 (1963).

[49] J.P. Jeukenne, A. Lejeune and C. Mahaux, Phys. Rep. **25**, 83 (1976).

[50] K.A. Brueckner and D.T. Goldman, Phys. Rev. **116**, 424 (1959).

[51] W. Czyz and K. Gottfried, Ann. Phys. NY **21**, 47 (1963).

[52] R. Jastrow, Phys. Rev. **98**, 1479 (1955).

[53] J.W. Van Orden, W. Truex and M.K. Banerjee, Phys. Rev. **C21**, 2628 (1980).

[54] J.G. Zabolitsky and W. Ey, Phys. Lett. **76B**, 527 (1978).

[55] M. Lacombe *et al.*, Phys. Rev. **C21**, 861 (1980), and references therein.

[56] S. Fantoni and V.R. Pandharipande, Nucl. Phys. **A427**, 473 (1984).

[57] H. Kümmel, K.H. Lührman and J.G. Zabolitzky, Phys. Rep. **36**, 1 (1978).

[58] J.J. Weinstein and J.W. Negele, Phys. Rev. Lett. **49**, 1016 (1982).

[59] J.J. Weinstein, Ph.D. thesis MIT (1982).

[60] M.J. Haftel and F. Tabakin, Nucl. Phys. **A158**, 1 (1970).

[61] T. Hamada and I.P. Johnston, Nucl. Phys. **34**, 382 (1962).

[62] J. Humberston and J.B.G. Wallace, Nucl. Phys. **A141**, 362 (1970).

[63] B. Filippone, Private Communication.

[64] S. A. Gurvitz and A. Rinat, Phys. Rev. **C35**, 696 (1987).

[65] H.J. Pirner and J.P. Vary, Phys. Rev. Lett. **46**, 1376 (1981).

[66] R. Brockmann and R. Machleidt, Phys. Lett. **149B**, 283 (1984).

[67] For a review, see R. Machleidt, K. Holinde and Ch. Elster, Phys. Rep. **149**, 1 (1987).

[68] I.S. Gradshteyn and I.M. Ryzhik, *Table of Integrals, Series and Products*, Academic Press 1980.

[69] P.K. Banerjee and D.W.L. Sprung, Can. J. Phys. **49**, 1899 (1971).

[70] A. Kallio and B.D. Day, Nucl. Phys. **A124**, 177 (1969).

[71] P.J. Siemens, Nucl. Phys. **A141**, 225 (1970).